IMPERIAL COLLEGE LONDON

Corrosion Scale Dynamics

by

Markus Peter Tautschnig

A thesis submitted for the degree of Doctor of Philosophy

in the

Faculty of Natural Sciences

Department of Physics

October 2017

Declaration of Originality

I certify that, except where appropriately referenced, the work is that of the author alone and has not been previously submitted to qualify for any other academic award.

– M. P. Tautschnig, October 2017

Abstract

This work presents a methodology for simulating ionic and electronic grain boundary transport through thin films, scales or membranes with columnar grain structure. In the model developed the grain structure is idealized as a lattice of identical hexagonal cells – a honeycomb pattern. Reactions with the environment constitute the boundary conditions and drive the transport between the surfaces. Time-dependent simulations solving the Poisson equation self-consistently with the Nernst-Planck flux equations for the mobile species are performed. In the resulting Poisson-Nernst-Planck system of equations, the electrostatic potential is obtained from the Poisson equation in its integral form by summation. An object oriented C++ code has been implemented to solve the system of equations numerically.

First, the model is used to interpret alumina membrane oxygen permeation experiments, in which different oxygen gas pressures are applied at opposite membrane surfaces and the resulting flux of oxygen molecules through the membrane is measured. Simulation results involving four mobile species, charged aluminum and oxygen vacancies, electrons, and holes, provide a complete description of the measurements.

Second, the model is extended to simulate internal oxidation and stress generation within a thin film of alumina at conditions of high-temperature metal oxidation. The steady-state stresses predicted are compatible with experimental measurements of lateral growth stresses in alumina scale growth experiments. The hypothesized $p - n$ ionic transition within the alumina grain boundaries is observed.

In limiting cases the more general simulations are closely related to the Wagner theory of metal oxidation. The Wagner theory assumes local ionic equilibrium while the simulation results demonstrate the possibility of a significant deviation from local Schottky equilibrium within an oxide scale at conditions of steady-state growth. The deviation is related to stress generation, and limits the applicability of the Wagner theory.

The three-dimensional model and computational approach developed in this work are readily adaptable to problems such as transport in a solid state electrode, corrosion scale growth, and oxide membrane permeation.

Acknowledgements

I would like to thank my supervisors Professor Nicholas Harrison and Professor Michael Finnis for their guidance and support throughout three busy years. The many shared meetings and discussions with Nic and Mike were a continuous inspiration and source of motivation.

I thank the Centre for Doctoral Training on Theory and Simulation of Materials (CDT-TSM) and the BP International Centre for Advanced Materials for funding. The many people I have met through the engaging activities of the CDT-TSM have made the past years a rewarding experience.

My parents have supported me generously from the start of my education and offered encouragement whenever needed. I am very grateful for that.

Contents

Notation

c_s	concentration (number density) of species 's'	m^{-3}
J_s	flux of species 's', positive flux in positive coordinate direction	$\mathrm{m}^{-2} \cdot \mathrm{s}^{-1}$
I_s	current density of species 's'	$\mathrm{A} \cdot \mathrm{m}^{-2}$
z_s	integer charge number of species 's'	
η_s	electrochemical potential of species 's'	$\mathrm{kg} \cdot \mathrm{m}^2 \cdot \mathrm{s}^{-2}$
ℓ_D	reference Debye length	m
λ_D	Debye length	m
μ_s	chemical potential of species 's'	$\mathrm{kg} \cdot \mathrm{m}^2 \cdot \mathrm{s}^{-2}$
ϕ	electrostatic potential	$\mathrm{kg} \cdot \mathrm{m}^2 \cdot \mathrm{s}^{-3} \cdot \mathrm{A}^{-1}$
ν	dominant vacancy species, $\nu/\overline{\nu}$**-notation**	
$\overline{\nu}$	charge compensating dominant electronic species, $\nu/\overline{\nu}$**-notation**	

Chapter 1

Introduction

All things pass and nothing stays

— Heraclitus as quoted by Plato in *Cratylus*

Corrosion is an ubiquitous phenomenon. Sometimes used synonymously with 'metal rusting' corrosion really denotes the generic process by which a refined metal is transformed into a more chemically-stable compound, such as an oxide or sulfide. The pervasiveness of the phenomenon is owed to the extensive use of metals and alloys in engineering and technological products, and to the unfortunate fact that at atmospheric conditions of temperature and pressure the laws of nature favour oxides and sulfides over the chemically pure metals.

To prevent their rapid decay the surfaces of most metals and alloys are chemically modified or coated before service. However, such a treatment is not always feasible or sufficient and the sublime usefulness of many alloys, despite their inevitable decay in most environments, is due to a peculiarity of the corrosion process: The formation of dense 'scales' as the oxidation reaction product that adhere to the alloy surface and subsequently act as a protective layer against further oxidation. While the presence of a dense adherent scale does not prevent the oxidation reaction, the impediment is often significant and changes the timescale of the decay. It is indeed the chemical stability of the chromium oxide and aluminum oxide forming naturally on chromium and aluminum containing alloys that adds significantly to the usefulness of these alloys in application.

Similar to the use and importance of silicon oxide as an engineerable protective film in much of semiconductor technology, chromium oxide and aluminum oxide scales are often formed deliberately on the alloy surface by high-temperature oxidation. In this work micrometer thin oxide layers on a metal or alloy surface are referred to as 'scales' or 'films' interchangeably.

A detailed understanding of the rate of formation and stability of such alumina and chromia scales is indispensable for the engineering of the scale on the alloy surface as a protective layer, particularly for alloys deployed at high temperatures and under chemically severe conditions. Growth of micrometer-thin films can often be described as a quasi-steady-state phenomenon, with constant ionic fluxes across the film that determine the growth rate. Given such conditions apply, there is a close resemblance between film growth and solid oxide membrane permeation. In a series of α-Al_2O_3 membrane oxygen permeation experiments Kitaoka *et al.* [83, 84] have demonstrated the occurrence of a '$p - n$' transition in the ionic transport depending on the oxygen partial pressures applied on the membrane surfaces. This has since sparked a renewed effort to gain a mechanistic understanding of alumina scale growth and the transport processes involved [70, 71], and motivated part of the work presented in this thesis.

In chapter 2, some experimental work and theoretical models from the literature on metal oxidation and corrosion scale growth are reviewed. Much progress has been made in understanding the formation and physical properties of oxide scales, especially α-Al_2O_3 has been studied intensively due to its technological importance. The importance of the grain structure during the formation of oxide films is emphasized. It is evident from the experimental literature that the grain structure plays a pivotal role in the formation of corrosion scales such as alumina and chromia. During the scale growth the grain boundary transport determines the overall kinetic behaviour and internal oxidation occurs at grain boundaries affecting the stability and adherence of the scale. The theoretical background for the simulation method described in chapter 3 is introduced, see in particular section 2.6. The experimental results of the series of α-Al_2O_3 membrane oxygen permeation experiments, mentioned above, are summarized in section 2.7.

In chapter 3, a novel continuum model is described that idealizes the grain structure of a growing film or scale as a slab consisting of a 2D periodic pattern of hexagonal cells. Both, the grain boundary transport and the internal oxidation including stress generation are taken into account in this hexagonal cell continuum model. First, the simulation methodology and computational approach are described. Second, the hexagonal cell model is applied to the above mentioned alumina membrane oxygen permeation experiments [83], see chapter 3 section 3.4. Third, the model is extended to include internal oxidation and stress generation in a corrosion scale, see chapter 3 section 3.5. Thereby, the stability of the scale depending on the oxidation conditions and physical properties of the scale, under the assumption of steady-state growth, can be studied.

The developed model is applied to α-Al_2O_3 scales but considered transferable to

other oxide and sulfide scales. The simulation methodology is closely related to 'drift-diffusion' semiconductor device simulations, and the vast literature available on this subject was relied upon in the mathematical formulation and numeric implementation of the computational approach. *Ab initio* simulations are related to the developed continuum model in that the physical input parameters can be obtained from techniques such as density functional theory, enabling – in principle – a straight forward 'multiscale' simulation approach, the connection is outlined in chapter 2. The simulation results of chapter 3 depend on the physical input parameters such as reaction equilibrium constants, and diffusion coefficients and although alumina has been deliberately chosen as a well studied and characterized material, only few of the desired parameters can be determined decisively from the experimental data available. Therefore, the choice of parameters constitutes a difficult step in the simulation methodology. The simulation results are benchmarked against analytical models which are applicable in certain limiting cases.

In chapter 4, some theoretical aspects of metal oxidation limited by 'drift-diffusion' transport through the scale are analyzed. The focus is on the 'classical' theory of metal oxidation by Carl Wagner. Classical in that it was developed in the nineteen-thirties but is still a standard tool today in the field of high-temperature metal oxidation due to its elegant thermodynamic formulation. The Wagner theory and related literature is introduced in chapter 2. Much of the work presented in chapter 3 is related to Wagner's theory and chapter 4 gives a discussion of it in light of the findings stemming from the calculations with the hexagonal cell model developed in chapter 3.

Chapter 2

Scale growth

2.1 Introduction

Metals and alloys react with oxidizing environments to reach a lower energy state. Unless kinetically limited this 'corrosion' or 'metal oxidation' process would proceed until either the metal or oxidant are exhausted. As the metal and environment composite system approaches the lower energy state 'corrosion scales' form as reaction product composed of metal and oxidant, where the latter is typically either oxygen of sulfur.

The dynamic behaviour can be described by entropic forces, driving the reaction and transport processes involved. If dense adherent scales form on the metal (alloy) surface, see figure 2.1, they separate it from the oxidizing environment, and ionic and electronic transport through the scale becomes an important aspect of the growth process. Scale growth can continue to occur at the metal-scale interface, the scale-environment interface, or at extended defects within the scale, examples of which are grain boundaries and voids. For growth at the metal-scale interface oxidant atoms or ions need to be transported through the scale, and similarly, metal atoms or ions need to be transported through the scale to sustain an oxidation reaction at the scale-environment interface. Assuming, as is typically the case, the absence of metal in the oxidizing environment. Either or both ionic transport processes have to occur during growth of dense adherent scales.

FIGURE 2.1: Schematic of uniform scale growth on metal (alloy) substrate.

It was first shown by Wagner [189] that ionic transport also requires electron transport to avoid the build-up of large electric fields within the scale that would suppress ionic diffusion, this theory is further described in section 2.3 and examined in detail in chapter 4. After the initial treatment, Wagner, a co-creator of the charged vacancy concept in solids [156], went on to interpret the ionic transport during oxidation in terms of cation and anion vacancies [190, 196]. His work remains influential in the literature on scale growth models, some of which are further discussed here in section 2.3.

Otherwise the chapter is organized as follows. Sections 2.1 to 2.4 give an overview of scale growth models from the literature. The importance of the grain structure for the oxidation behaviour of alumina and chromia scales is well known; however, growth models generally do not take into account a realistic description of the grain structure and grain boundary transport. The results from the literature on the electronic structure properties of alumina are summarized in section 2.5, since they are relevant for the application of the model developed in this work. In section 2.6, the theoretical background is introduced for the transport equations used in the model developed here, which is further described in chapter 3.

A process closely related to uniform steady-state metal oxidation is oxide membrane permeation. In permeation experiments the two surfaces of an oxide membrane can be subjected to atmospheres with different oxygen partial pressure, and resulting ionic fluxes provide insight into the transport processes occurring during metal oxidation. A series of such permeation experiments on α-Al_2O_3 membranes was conducted recently by Kitaoka *et al*. [83, 84], and part of the work in this thesis is concerned with simulating the membrane permeation computationally, see chapter 3. The experimental results of Kitaoka *et al.* are therefore summarized in section 2.7.

2.2 The characteristic time dependence

The oxidation of metal consists of multiple steps, involving the dissociation of molecular oxygen (sulfur), transport through the growing oxide layer, and the reaction between oxygen (sulfur) and metal atoms, it is therefore a heterogeneous non-equilibrium process. For parallel processes the fastest process is rate determining and for processes in series the slowest process is rate determining. The simultaneous diffusion of one species through the grains and grain boundaries of the scales would be a parallel process. The interface reactions and transport through the scale constitute an example of processes in series.

In this work and as is usual in most scale growth models only the idealized situation of growth with planar interfaces is considered, that is the metal–scale and metal–environment interfaces are idealized as planes parallel to each other and growth occurs normal to the interface planes. This is also referred to as 'uniform' scale growth. The surface structure involving steps, kinks, *etc.* is not taken into account explicitly, the interface reactions considered typically describe an averaged behaviour. Most importantly, therefore, in growth of dense adherent 'uniform' scales are the relative rates of the oxidation reactions at the interfaces and the transport through the scales to sustain the reactions; the slower process determines the overall rate dependence. The rate limiting step determines the characteristic functional time dependence of the growth rate for scales with planar interfaces

$$\frac{dL}{dt} = F\left(L,\, t, ...\right) \tag{2.1}$$

where L denotes the thickness of the film or scale at time t, and $F(\cdot)$ is a function to be determined from experimental data or based on a physical model.

Despite the complexity of the oxidation and scale growth processes, and the variety of materials and environments found in application and experimental studies, a small number of characteristic time dependences encompass most experimentally observed behaviours. Growth of thick films in high-temperature oxidation of metals (alloys) typically adheres to a 'parabolic' growth rate law

$$L(t) = \sqrt{2k_{\mathrm{p}}\, t}. \tag{2.2}$$

Other rate dependences frequently observed in oxidation experiments are the 'linear' law,

$$L(t) = k_{\mathrm{l}}\, t \tag{2.3}$$

the 'logarithmic' law,

$$L(t) = a_1 + a_2\, \ln\left(t\right) \tag{2.4}$$

$$\tag{2.5}$$

and 'inverse logarithmic' law

$$L(t) = 1/(b_1 + b_2\, \ln\left(t\right)). \tag{2.6}$$

While the experimental growth kinetic data can often be fitted satisfactorily to one of these characteristic time dependences various growth models have been developed in the literature to justify the functional forms and to explain the rate constants in these laws in terms of physical system parameters. Growing scales are found to switch between different characteristic time dependences, depending on the transport and interface reaction rates, and in particular their thicknesses; an effect which only few growth models are able to predict.

Growth models in the literature for predicting or interpreting scale growth can be classified as empirical, semi-empirical, and mechanistic [133]. Empirical and semi-empirical models are fitted to experimental data, consist of arbitrary functions, and have limited validity outside their calibration range. Mechanistic models aim to translate information about the key physical processes into a suitable mathematical formalism.

This work focuses on systems in which ionic and electronic grain boundary diffusion, and the resulting internal electrostatic field are significant for understanding the overall growth process. What follows is a brief review focusing on influential theories in the literature that have advanced the mechanistic understanding of the growth process.

2.3 Review of some scale growth models from the literature

The observation of the square root time dependence in the scale thickness, $L(t)$,

$$L \sim \sqrt{t} \tag{2.7}$$

led to the first theories of scale growth with diffusion of the atomic species (neutral) through the growing scale as the rate limiting step [47]. Assuming for example the metal to be soluble in the scale, a metal concentration gradient, ∇c_{M}, arises between the metal–scale, I, and the scale–environment, II, interface. Suppose the metal diffuses by an interstitial mechanism to the oxidant containing environment, and assuming a quasi steady-state in which the metal at the interface II is consumed instantly by the oxidation reaction to generate new scale, the Fickian diffusion flux reads as

$$J_{\mathrm{M}} = -D_{\mathrm{M}} \nabla c_{\mathrm{M}} = -D_{\mathrm{M}} (c_{\mathrm{M}}^{II} - c_{\mathrm{M}}^{I}) \,/\, L(t) \tag{2.8}$$

where D_{M} is the diffusion coefficient (constant), and c_{M}^{j} is the concentration at the j-th interface. The flux is constant as a function of the position in the scale, but through

the thickness, L, the flux depends on time and decays as $\sim 1/L$ provided the interfacial concentrations are fixed. This means the oxidation reaction at the interface II consumes exactly that amount of metal in a given small period of time, between t and $t+dt$, which arrives at the interface II by diffusion; J_{M} per unit of surface area and time. Therefore, the scale thickness changes as

$$\frac{dL}{dt} = \Omega \, |J_{\mathrm{M}}| \tag{2.9}$$

where Ω is the amount of volume added to the scale per metal atom arriving at the interface II. Integration yields the square root growth law including a rate constant that depends on the material properties.

Building on this earlier work, Wagner, in his 'Contribution to the theory of the tarnishing process' [189–191, 196], derived an expression for the parabolic rate constant assuming drift-diffusion of ions and electrons as the rate limiting step

$$k_{\mathrm{p}} = \frac{\Omega_{\mathrm{u}}}{e_0 |z_{\mathrm{X}} z_{\mathrm{M}}|} \int_I^{II} \frac{(\sigma_{\mathrm{X}} + \sigma_{\mathrm{M}}) \, \sigma_{\mathrm{e}}}{\sigma_{\mathrm{X}} + \sigma_{\mathrm{M}} + \sigma_{\mathrm{e}}} \, d\mu_{\mathrm{X}} \tag{2.10}$$

where Ω_{u} is the volume per formula unit of scale material; e_0 is the positive elementary charge; the subscripts 'X' and 'M' denote the oxidant and metal, respectively; z_{X} and z_{M} are the integer charge numbers; σ_{X} and σ_{M} are the conductivities; σ_{e} is the electron conductivity; μ_{X} is the oxidant chemical potential; and the integration domain is bounded by the alloy (metal) – scale interface 'I' and the scale – environment interface 'II'. To arrive at this expression the drift-diffusion of ions and electrons during the growth process are considered, and a parabolic growth rate, $L = \sqrt{2k_{\mathrm{p}}t}$ of course only follows if k_{p} is indeed *constant* as the thickness increases.

The theory assumes thermodynamic equilibrium to hold at the metal–scale and scale–gas interfaces and a steady-state growth with no divergences of the mobile species fluxes. Transport through the scale with constant diffusion coefficients is the rate limiting step, and the scales are considered to be free of voids, grain boundaries, and any other extended defects.

The Wagner theory is a standard device to analyze high-temperature oxidation experiments with films thicker than 1μm [2, 21]. It is also often used to solve the inverse problem of calculating diffusion coefficients from the measured scale growth rates, e.g. [164]. While in principle all parameters in this theory are experimentally accessible, the variation of the conductivities throughout the film or their dependence on the oxidant chemical potential are typically not known and the formula 2.10 is approximated. The range of validity or error in these approximations is seldom discussed.

The question of growth rate behaviour different from parabolic and predicted from the same level of theory was also investigated by Wagner [192], in particular also the question of simple rate laws between the limiting cases of thin and thick films [193]. An early discussion and confirmation of the Wagner theory was given by Bardeen [8] investigating the oxidation of copper with copper vacancy mediated diffusion as the limiting step in the growth rate.

Reviews of the Wagner theory are available in the literature, see for example Atkinson's review article [2] or reference [62], a thorough discussion of Wagner's theory is given here in chapter 4 section 4.2. The self-consistency of the Wagner theory and the notion that this theory necessarily predicts a parabolic growth rate have both been challenged in the literature [47]; these criticisms are analyzed in chapter 4 sections 4.2.2 and 4.3.3, respectively.

In a series of papers Mott [125–127] aimed to extend Wagner's work to thin oxide films, and to find an explanation for the drop in growth rate at a certain self-limiting thickness on the order of nanometers for some oxides. These thin layers are referred to as 'passive films', and the Mott-Cabrera theory [14] is most influential for interpreting their growth behaviour. Mott noted that for nanometer thin films electrons could tunnel from the metal–film to the film–environment interface, setting up a strong electric field in which the metal ions are transported through the film to the oxidant containing environment; thereby rendering the interface reaction of metal leaving the alloy or metal substrate the rate limiting step. The model predicts an inverse logarithmic growth rate for thin films in the 'high-field limit', and a parabolic rate for thick films with a weak electric field.

The Fehlner-Mott model [39] for low, below $300\,\mathrm{K}$, temperatures predicts logarithmic growth. Three stages are described: oxygen incorporation into the metal substrate by diffusion (place exchange); continued slow logarithmic oxide growth with a voltage built up – the Cabrera-Mott potential; and subsequent 'reordering' of the film leading to a faster logarithmic rate due to grain boundary diffusion and resulting island formation. A review of the oxidation kinetics for transition metals at low- and intermediate temperatures can be found in [163]. Transport in transition metal oxides and sulfides can be expected to introduce additional complexity, an early discussion was given by Wagner [195].

The 'point-defect-model' [17] was developed as an extension of Wagner's theory to condensed phase environments and particularly aqueous environments where

its predictions have been found in good agreement with experiment in many applications [103]. The model was later improved to account for new experimental findings in particular steady-states in the film thicknesses. The growth rate in this model is given by

$$dL/dt = a_1 \exp(-a_2\, L) - a_3 \tag{2.11}$$

with constants, a_i, and details of the improved model can be found in [102]. It assumes a bi-layer structure with an inner defective oxide or hydride barrier layer and an outer layer formed by precipitation from an aqueous environment.

The current version of the point-defect-model focuses more on the outer layer in recognition of experimental indications that these outer layers could have a significant impact on the overall corrosion behaviour [104]. The development of the point-defect-model is reviewed in [103]. Many other models for thin passive films in solutions are known in the literature, following MacDonald they could be classified as high-field models [14, 39], place exchange models [153], and interfacial equilibrium models [81, 185, 186]; a more comprehensive list of references is given in [103].

The Mott-Cabrera, Mott-Fehlner, point-defect (MacDonald), and additional models that have been suggested in the literature are reviewed for example in [159].

The focus of this work, however, is on dry oxidation where another influential model for dry high-temperature oxidation is found in the Deal-Grove model [29]. It is used to interpret and predict thermal oxidation of silicon which is especially important for semiconductor device fabrication. The model takes into account the fluxes of the oxidant in the gaseous environment and through the growing silicon-oxide, and the reaction between the oxidant and silicon substrate at the substrate–oxide interface. This entails Henry's law, Fickian diffusion, and a first-order reaction at the substrate–oxide interface while electric field effects are neglected. In the presumed steady-state conditions the transport processes and interfacial reactions are simply proportional to the oxidant concentrations at the interfaces, and in the bulk gas. It predicts a linear or parabolic growth rate depending on the parameters, and it is known to fail for nanometer thin and for polycrystalline films.

Fromhold has pioneered the use of computer simulation and numeric analysis to model metal oxidation [47, 50]. His work on analytic and numeric analysis of oxide growth includes modelling ionic diffusion under the influence of electron tunneling [52], thermionic emission [53], and extensive analysis of space charge effects, see for example [51] and references therein. Similarly to Fromhold's work on solving the equations for ionic diffusion numerically [50] frameworks for modelling metal oxidation based on

ionic transport equations and the Poisson equation for determining the self-consistent electric field have been described in the literature [10, 134]. Typically these simulation approaches assume homogeneous scales which means the effects of dislocations and grain boundaries that are known to act as preferential pathways in some oxides are neglected.

The scale grain structure is particularly important for the transport properties in oxides such as alumina and chromia, and the next section gives an overview over related experimental findings, as well as modelling approaches.

2.4 The scale grain structure

The structures found in scale growth experiments range from amorphous or nanocrystalline to microcrystalline, and also porous and multilayer structures have been observed [2, 119]. Under some conditions the oxidation becomes a cyclic process of scale growth, cracking, and delamination. The granular structure of the scales depends on the oxidizing conditions, wet or dry, the temperature, and material properties such as the surface free energies of the growing grains for example.

The importance of the grain structure for nanometer thin 'passive' films and the influence of grain boundaries on their stability and growth is increasingly well recognized and studied due to advances in the relevant experimental characterization techniques available [65, 110, 111, 119].

In high-temperature oxidation and growth of micrometer thick films the importance of the grain structure has long been recognized, typical morphologies observed are microcrystalline columnar or columnar-equiaxed duplex structures [2]. Aluminum oxide (Al_2O_3) [129], nickel oxide (NiO) [2, 163], and iron sulfide (FeS) [120] can be named as exemplary materials forming these structures. Two of the most important and technologically relevant oxide scales are aluminum oxide, α-Al_2O_3 (alumina), and chromium oxide, Cr_2O_3 (chromia), that are frequently formed deliberately on alloy surfaces to serve as high-temperature oxidation barriers as part of thermal barrier coatings [26, 27, 35, 37, 142, 167], show transport behaviour dominated by the grain boundaries of the polycrystalline films or scales. Due to their technological importance the grain boundary transport in these materials has been studied heavily experimentally [3, 4, 59, 170], and more recently also by computer simulations [69]. For alumina it has been found that the oxygen and aluminum fluxes through the scales both contribute significantly [135, 178] to the overall growth rate, but the microscopic diffusion mechanisms in bulk and the grain boundaries are still under debate [68, 69, 71]. A

recent series of membrane oxygen permeation experiments [83] have contributed new insight into the diffusion properties of alumina they are further discussed in section 2.7.

Typically Harrison's [60, 172] scheme is employed to classify processes with significant grain boundary diffusion. In the intermediate 'B' regime the grain diffusion length with the grain (bulk) diffusion coefficient, D_{g}, satisfies

$$\delta \ll \sqrt{D_{\mathrm{g}} t} \ll d \tag{2.12}$$

where the grain boundary width, δ, and the average grain size, d, appear. The 'A' regime applies for smaller grain diffusion lengths, $\sqrt{D_{\mathrm{g}} t}$, and the 'C' regime for larger ones. In the B regime the grain boundary diffusion contribution to the flux through the material is significant, in the A regime it is dominant. A frequently applied modification of the Wagner theory [73, 162] to account for grain boundary diffusion is based on an effective diffusion coefficient introduced by Hart [61]

$$D^{\mathrm{H}} = D_{\mathrm{g}} \left(1 - f\right) + D_{\mathrm{gb}} \, f \tag{2.13}$$

where D_{gb} is the grain boundary diffusion coefficient; and $f = q\delta/d$ is the grain boundary volume fraction with the grain boundary width, δ, the average grain size, d, and a numerical constant q characterizing the grain shape [64, 121].
The Fisher-Whipple-LeClaire model [43, 91, 199], which is discussed for example in references [64, 121, 172], is a standard tool in analysing grain boundary diffusion experiments. Tracer concentration profiles extracted from secondary ion mass spectroscopy of the diffusion samples are analyzed with analytic solutions and functional forms obtained from the Fisher-Whipple-LeClaire model. Originally developed for metals this model is also applied to tracer diffusion experiments on oxides [40].

None out of the Harrison classification, the Hart effective diffusion coefficient, and the Fisher-Whipple-LeClaire model include effects of an internal electric field which is clearly present during diffusion of ions mediated by charged vacancies or interstitials. This means any space charge or Debye double layer effects that could be particularly relevant for preferential diffusion along dislocations and grain boundaries are not explicitly discussed in the relevant studies. No generally accepted generalizations of these models to include electric field effects are currently available in the literature.

In the field of solid state ionics and its subfield nanoionics space charge effects have been studied intensively [105, 106, 109] and are often actively sought for use in electrochemical devices that exploit interfacial and size effects for ionic transport and

charge storage [108]. Electrochemical devices exploit materials with mixed electronic and ionic conduction to transform chemical energy into electrical energy or information as in the case of oxygen sensors. Reviews of 'fast ionic conduction' and ionic conduction in nanocrystalline materials in this context are available in [181] and [58], respectively. The space charge near grain boundaries in equilibrium is a consequence of charge carrier segregation due to the different structure of the interfacial core. As the proportion of interface to bulk increases for a material with ionic and electronic disorder the bulk electroneutrality condition has to be replaced by the Poisson equation, the related changes in the species concentrations can be large and affect the ionic transport significantly [107]. Analytic models for taking into account space charge effects on ionic transport have been developed [80, 180]. Detailed modelling of space charge effects due to accumulation and depletion of charge carriers at interfaces depending on the material properties and parameters characterizing the environment generally requires numeric solutions of the relevant system of equations. In these simulations the grain structure is typically idealized as in the 'brick layer' model of cubic grains [44, 57], but also conduction in two-dimensional Voronoi grain structures has been investigated [45].

These models do, however, typically not consider simultaneous transport of vacancies, electrons, and holes in a chemical potential gradient, which is required for studying oxidation. Furthermore, during counter diffusion of anion and cation vacancies formation and dissolution of scale at grain boundaries can occur and generates stress. These aspects are addressed with the hexagonal cell model presented in chapter 3. Growth stresses are observed in oxidation experiments and further discussed in section 3.5.

2.5 Electronic structure: point defects and interfaces

In what follows a brief review of the defect and electronic structure properties of alumina is given that have been elucidated by recent density functional theory (DFT) and molecular dynamics calculations.

The effective charges of the point defects are defined with respect to the ions of the pristine lattice, and the Kröger-Vink notation for point defects is used, although for generality, integers are used to denote the charge states rather than the original superscript $^{\bullet}$ or $'$ symbols, while the $^{\times}$ notation for neutral species is retained.

To understand and predict the oxidation properties of alumina scales the point defect concentrations and hopping barriers in the bulk material and at the grain boundaries are required. While the point defect formation energies can be used to determine the defect populations and help elucidate solid state diffusion in oxides, localized states in the band gap induced by the defects can give rise to charge trap states relevant for the electron transport.

As a widely used ceramic the electronic structure of alumina is also of interest in a range of technological applications, such as high-temperature structural ceramics and gate dielectrics in metal-oxide-semiconductor devices. This means many theoretical studies of its electronic structure are available.

DFT calculations have become a standard tool for first principles calculations of defects in solids [46]. The Kohn-Sham density functional theory is a formally exact method of calculating the ground state energy of a fixed number of interacting electrons in a multiplicative external potential. This ground-state is determined by mapping the interacting system onto a fictitious system of non-interacting electrons with the same electron density as the real interacting system. The electrons move in a multiplicative effective (Kohn-Sham potential) potential that consists of the ionic potential due to the ion cores, electron-electron interaction (Hartree) potential, and the many-body effects are lumped into the exchange-correlation (xc) potential. Different methods have been developed to solve the resulting self-consistent one-electron Schrödinger equations. A pivotal element is a suitable approximation of the xc functional that yields reliable results at reasonable computational cost. Most of the results from the literature mentioned in this section have been determined from DFT calculations.

Statistical thermodynamics provides a convenient framework for the description of point defects in solids. In the equilibrium state of a solid with an environment at fixed temperature, T, and pressure, P, its Gibbs free energy has a minimum

$$\delta(U - TS + PV) = 0. \tag{2.14}$$

The thermodynamic system permits no exchange of matter with the environment, only heat and volume can be exchanged. In any solid at equilibrium there exists an ensemble average number of point defects such that the increased vibrational and configurational entropy balances the energy cost of forming them by breaking the bonds and adding the atom to the crystal surface or a chemical reservoir. A discussion of point defect thermodynamics in crystals summarizing the most salient concepts has been given by Finnis in reference [151].

There is an analogy in the statistics of vacancies in lattices and electrons in discrete quantum states. Randomly distributing a fixed number of vacancies over lattice sites is mathematically equivalent to distributing a fixed number of electrons over discrete quantum states, and for a fixed total energy the Fermi-Dirac distribution

$$\langle n_i^s \rangle = \frac{1}{e^{(\epsilon_i - \eta_s)/k_\mathrm{B}T} + 1} \tag{2.15}$$

maximizes the entropy. It expresses the probability of the i-th state with energy ϵ_i to be occupied, while 'η_s' denotes the electrochemical potential of species 's'. In the dilute limit $\langle n_i^s \rangle \ll 1$ the occupation function reduces to the Boltzmann form

$$\langle n_i^s \rangle \simeq \exp\left(\frac{\eta_s - \epsilon_i}{k_\mathrm{B}T}\right). \tag{2.16}$$

Given the conditions for the dilute limit apply, the electrochemical potential of species 's' including electrons, holes, and point defects can be written as

$$\eta_s(r) = k_\mathrm{B}T \, \ln\left(c_s(r)/c_s^0\right) + z_s e_0 \, \phi(r) \tag{2.17}$$

where c_s is the concentration (number density); z_s is the integer charge state, and e_0 the elementary charge; and which separates a chemical term from the mean field electrostatic potential, ϕ. The expression is expected to hold also for small deviations away from equilibrium, hence the spatial dependence with the position vector r, and the number density c_s^0 characterizes the chosen reference state. The theory underpinning the extension to a spatial dependence of η_s is further described in the next section.

The electron electrochemical potential, η_e, in equilibrium is also referred to as the Fermi level. The Fermi energy, ϵ_F, denotes the Fermi level in the limit of the temperature $T \to 0\,\mathrm{K}$. For non-degenerate semiconducting materials and large band gap insulators, which are relevant for this work, the dilute limit applies. For temperatures $T > 0\,\mathrm{K}$ the excitation of electrons raises the Fermi level discontinuously to somewhere in the band gap. For electron-hole equilibrium furthermore, $\langle n_i^\mathrm{h} \rangle = 1 - \langle n_i^\mathrm{e} \rangle$ and $\eta_\mathrm{h} = -\eta_\mathrm{e}$. Away from equilibrium, where the electron and hole electrochemical potentials are not constant as a function of position, they are also referred to as quasi Fermi levels in the literature [173].

Al_2O_3 has a number of different phases. The stable aluminium oxide phase α-Al_2O_3 at most conditions of interest adopts the R$\bar{3}c$ space group (corundum), with fourfold coordinated O sites and sixfold coordinated Al, see figure 2.2. The tetrahedron

of Al ions surrounding the O ion is distorted, with two (about 5%) shorter bonds out of the four in total. Correspondingly, any Al ion is surrounded by a distorted octahedron of O ions. The primitive rhombohedral unit cell has $1/3$ the volume of the conventional hexagonal cell. Simulations to obtain defect formation energies are typically performed in supercells consisting of multiple primitive or conventional cells and the defect of interest. This allows the calculations to be performed with the highly efficient computational methods developed for periodic solids. The supercell size is generally limited by the computational cost and the remaining artificial effects have to be corrected for *a posteriori* [46].

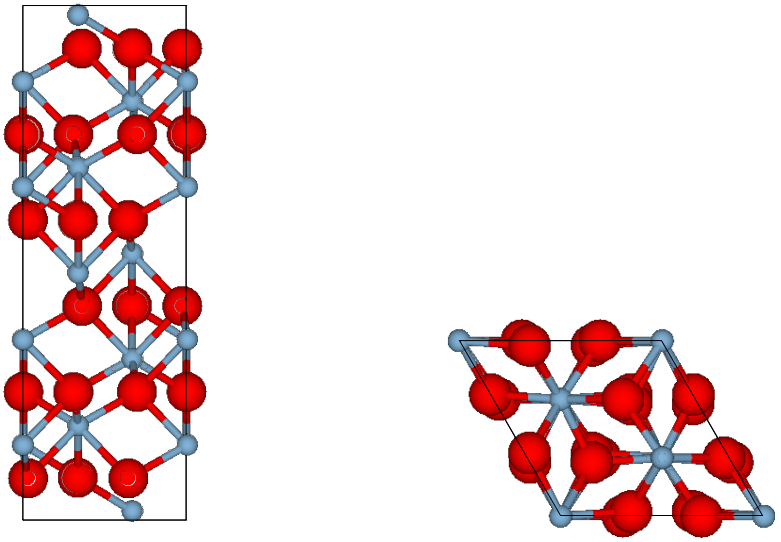

FIGURE 2.2: Corundum conventional unit cell. View along the a-axis (left) and c-axis (right).

Alumina is classified as a material with mostly ionic character and typically the point defects with the nominal ionic charges, $\mathrm{V}_{\mathrm{O}}^{2+}$ and $\mathrm{V}_{\mathrm{Al}}^{3-}$, are expected to be the most energetically favourable in the bulk material.

Within the Zhang-Northrup formalism the dependence of the formation energy on the Fermi level and the component reservoir chemical potentials can be investigated in density functional theory (DFT) calculations [46, 200]. Calculations for bulk alumina are available for example in [22, 74, 99, 118]. However, different choices for the exchange correlation functional and band gap correction can lead to discrepancies in the predicted properties. For example, the donor transition levels $5\,\mathrm{eV}$ above the valence band maximum introduced by $\mathrm{V}_{\mathrm{O}}^{\times}$ reported in [118], have been found at $3.5\,\mathrm{eV}$ above the valence band maximum by Hine *et al*. [74]. The disagreement has been attributed to the difference in the band gap correction procedure adopted [22], which typically assume that only the conduction band states are affected by the band gap error. The

band gap in semiconductors and insulators is defined as the difference between the first ionization energy and the first electron affinity of the neutral solid. Reported values for the experimental band gap of monocrystalline alumina are between $8.8\,\mathrm{eV}$ and $9.4\,\mathrm{eV}$.

Also defect formation and migration energy studies for alumina twin grain boundaries are available [93, 138, 174, 176]. The band structure properties of alumina and their influence on the transport during oxidation have been reviewed by Heuer *et al.* [69, 71]. The defect formation energies, charge state, and the hopping barriers are all crucial for the non-equilibrium drift-diffusion process. The Fermi level is expected to be pinned by gap states at the metal–oxide interface. Band bending and gap states are discussed extensively in the semiconductor and device literature see for example the monographs [122, 124] or the review [201].

During the oxide growth the Fermi level varies between the metal–oxide and oxide–gas interface. The gradient of the electron electrochemical potential, $\nabla\eta_\mathrm{e}$, cannot vanish since it drives the electron current which has to balance the vacancy current at any point in the oxide in the steady-state. Taking the valence band maximum at the metal–oxide interface 'I' as the starting point the sign of the slope in the Fermi level depends on

$$\mathrm{sgn}\{\sigma_\mathrm{ion} - \sigma_\mathrm{el}\} \tag{2.18}$$

the difference of the ionic and the electronic conductivity, see also figure 2.3 and figure (4) in reference [71].

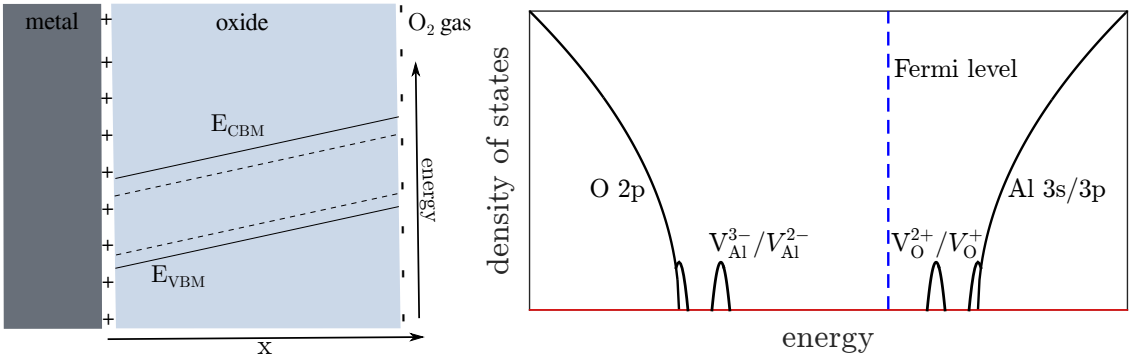

FIGURE 2.3: (a) Schematic of the Fermi level variation in the oxide for $\sigma_\mathrm{ion} > \sigma_\mathrm{e}$. The conduction band minimum (CBM) and valence band maximum (VBM) are indicated. The dashed lines represent the localized states. An electric field is present in the non-equilibrium steady-state and its direction also depends on $\mathrm{sgn}\{\sigma_\mathrm{ion} - \sigma_\mathrm{e}\}$. (b) Schematic of the density of states for polycrystalline α-alumina [71]. Grain boundary states due to the aluminum and oxygen ions, and deep levels due to the vacancies are indicated. The vacancies could act as donor and acceptor states by trapping electrons or holes.

While the experimental evidence seems unequivocal on grain boundaries as the dominant pathways for ionic transport in alumina, e.g. [68, 147], the electron and hole transport mechanisms and pathways are largely unknown. The microscopic transport mechanism for the atoms or ions in alumina grain boundaries is also still under debate. The Arrhenius form diffusion coefficients deduced from experiments show unusually large prefactors and activation energies for the alumina grain boundaries [68, 71]. To account for the large prefactors that could indicate a cooperative diffusion mechanism Heuer *et al.* have proposed a 'disconnection' mechanism for atomic transport through alumina grain boundaries [71, 72]. Disconnections are defects that exhibit combined dislocation and step character. They can mediate mass transfer along interfaces by virtue of their step character and produce deformations through their dislocation character [75, 77]. The disconnections are thought to glide through the grain boundary plane driven by the Peach-Koehler force which is a thermodynamic force describing the tendency of a dislocation to move in the presence of a stress field [172].

The electronic states in infinitely large perfect crystals are described by Bloch waves and commonly aligned in bands of permitted states, structured in the valence and conduction bands in semiconductors. The density of states (DOS) denoted by, $g(E)$, is a measure for the number of available quantum states between the energies E and $E + dE$ in a material and important for many of its properties. In general at a fixed electron concentration the Fermi level, η_{e}, is implicitly defined by

$$N_{\mathrm{e}} = \int_{E_{\mathrm{c}}}^{\infty} g(\epsilon)\, f^{\mathrm{e}}(\epsilon; \eta_{\mathrm{e}})\, d\epsilon \tag{2.19}$$

where N_{e} is the number of conduction band electrons, and f^{e} denotes the distribution function $\langle n^{\mathrm{e}}(\epsilon)\rangle$. The square root behaviour of the density of states, $g(\epsilon) \sim \sqrt{|\epsilon - E_i|}$, near the conduction, $E_i = E_{\mathrm{c}}$, and valence band edges $E_i = E_{\mathrm{v}}$, is a good approximation for many semiconductors.

However, the density of states in imperfect materials containing defects is a more complex quantity. Point defects such as vacancies and interstitials are a source of scattering in electron transport and of localized energy states in the band gap of the material. The localized states denote occupied orbitals that may exist in the vicinity of the defect site. The lower conduction band of bulk α-Al_2O_3 consists of Al $3s$ states and the upper valence band of O $2p$ states. DFT calculations for bulk alumina have shown that vacancies can introduce localized states and corresponding transition levels in the band gap region [22, 74]. The projection of the density of states (DOS) on pristine grain

boundary regions of DFT calculations for two $\Sigma 7$ tilt grain boundaries shows localized states at the boundary [56]. It has been suggested that the electrons and holes in alumina grain boundaries are localized on the states introduced in the gap by the vacancies [71]. This would imply doubly charged aluminum vacancies, V_{Al}^{2-}, and singly charged oxygen vacancies, V_{O}^{+}, see figure 2.3 (b).

The localized states could act as trap states capturing electrons from the conduction band or holes from the valence band. Electron conduction in bulk α-Al_2O_3 is considered consistent with Poole-Frenkel hopping involving a localized state $\sim 1.8\,\text{eV}$ below the conduction band edge [99]. Trapping or release of electrons by the localized states requires less energy than the excitation from the valence to the conduction band. The trapped particles could then recombine as is described for example in the Shockley-Read electron-hole recombination process [173]. The electron-hole recombination could lead to an enhanced vacancy diffusion as was suggested for some semiconductor materials [197, 198]. Recombination enhanced migration could occur by a local heating mechanism due to the recombination excess energy or due to a defect charge state dependent diffusion coefficient.

Several elements, if present in low-concentrations in aluminum-containing or chromium-containing elements, are known to segregate to the alloy–oxide interface and the grain boundaries of the growing oxide during high-temperature oxidation. The segregated elements are expected to modify the transport properties of the grain boundaries and the interfacial bonding at the alloy-oxide interface. The elements Y and Hf are known to dramatically reduce the growth rate of alumina scales. This 'reactive element effect' is used to engineer the growth of thin, dense and adherent alumina or chromia scales on alloy surfaces. Different explanations have been proposed, typically involving the differences in the ionic size resulting in a steric 'blocking' effect, for a recent review see [130]. However, the ionic size effect cannot account for all observations [71]. Based on DFT calculations it has been hypothesized that the segregation of reactive elements, e.g. Y, modifies the population of near band edge grain boundary states [70, 71], thereby affecting the grain boundary transport.

2.6 Drift-diffusion equations

The drift-diffusion or Nernst-Planck flux [131, 145] occurs in the description of various physical processes. Particular examples are transport in ionic channels of organic tissue [33, 34], the electron-hole transport in semiconductor devices [112, 158], and electrochemical systems in general [12]. The Nernst-Planck flux is frequently introduced

as a phenomenological equation and can be thought of as a superposition of Fickian diffusion in the chemical potential gradient and Ohmic conduction in the electrostatic potential gradient. In this section the flux equation is introduced including some theoretical background and comments on the range of validity of this transport model. For a time-dependent transport model including a self-consistent electric field, the flux equations have to supplemented by the continuity equation and the Poisson equation, as is described below.

The drift-diffusion equations for electron-hole transport in semiconductors have been analyzed theoretically and numerically for decades [173]. Thorough discussions of their mathematical properties are available in the literature [112, 158], and the connection to higher levels of theory including quantum effects on electron-hole transport has been established [79, 155].

Transport of ions in oxides has been studied less intensively. Approaches for going beyond the mesoscopic Poisson-Nernst-Planck equations by coupling them to classical density function theory have been introduced in the literature on ion channels [54]. A methodology for coupling quantum density functional theory to the Poisson-Nernst-Planck equations to model grain boundary oxidation is described in [171].

In this work the transport of electrons and ions is treated on the same level of theory, the transport of all mobile species is described by the Nernst-Planck flux expression. The thermodynamic basis of the transport equations is emphasized and it indicates the generic applicability of the equations adopted here. This level of theory in the transport equations is, furthermore, ideally suited for describing the reaction boundary conditions to the transport equations by the law of mass action, which is further discussed in chapter 3. In linear irreversible thermodynamics [28, 92] transport of ions and electrons is formulated in terms of material specific kinetic coefficients and thermodynamic driving forces. In this theory the concepts and quantities of equilibrium thermodynamics are applied to small subsystems or 'cells' of the non-equilibrium system under consideration. In these cells 'local' thermodynamic equilibrium is assumed to hold, and the thermodynamic state variables are thereby extended to functions of position and time. Irreversible thermodynamics is commonly adopted to describe kinetic transformations in materials involving atomic transport [5], a concise treatment of the theory is given in the monograph by Lebon and Jou [92].

In section 2.6.1, the system of equations is defined, the unit system adopted is described, and the physical assumptions necessary for the validity of the equations are summarized.

In section 2.6.2, the effect of Coulomb screening as predicted from the classical Nernst-Planck theory is discussed briefly, this effect is essential for understanding the charge dynamics and electric field effect during oxide scale growth.

2.6.1 Poisson-Nernst-Planck theory

Based on the local equilibrium hypothesis the electrochemical potential, $\eta_s(r,t)$, of species 's' such as point defects, electrons or holes at position r and time t is written as

$$\eta_s(r,t) = \mu_s(r,t) + z_s e_0\, \phi(r,t) \tag{2.20}$$

where, μ_s is the chemical potential, ϕ is the electrical potential, z_s is the integer charge number, e_0 is the positive elementary charge, and $r = (x_1, x_2, x_3)$ is the position vector. Within linear irreversible thermodynamics [92, 139, 140] the particle flux, J_{N_s}, of species s, under isothermal conditions ($\nabla T = 0$), is given by

$$J_{N_s} = L_{N_sN_s} \nabla \left(\frac{-\eta_s}{T} \right) = -L'_{N_sN_s} \nabla \eta_s \tag{2.21}$$

with the kinetic coefficient, $L_{N_sN_s}$, the temperature T, and $L'_{N_sN_s} = L_{N_sN_s}/T$. The cross terms $L_{N_sN_{s'}}$ between species s and s' have been neglected and since the material is modelled as an isotropic medium, the kinetic coefficients are scalars. In a system with uniform concentrations ($\nabla \mu_s = 0$), but a non vanishing electric field, $E = -\nabla\phi$, the current density, I_s, is given by

$$I_s = z_s J_{N_s} = -z_s^2 e_0^2 L'_{N_sN_s} \nabla \phi \tag{2.22}$$

where equations 2.20 and 2.21 have been used. In mechanical equilibrium and within the ideal dilute solution approximation [15], in which the gradient of the chemical potential of species s, only depends on the concentration (number per unit volume), c_s, of species s, and with a uniform electrical potential ($\nabla\phi = 0$), the particle flux reduces to

$$J_{N_s} = -L'_{N_sN_s} \frac{k_\mathrm{B} T}{c_s} \nabla c_s \tag{2.23}$$

where equations 2.17 and 2.21 have been used. Through Ohm's law of conduction and Fick's law of diffusion

$$I_s = -\sigma_s \nabla \phi \qquad \text{and} \qquad J_{N_s} = -D_s \nabla c_s \tag{2.24}$$

where D_s is the diffusion coefficient of species s, the kinetic coefficient, $L'_{N_sN_s}$, is linked to the conductivity, σ_s, and the diffusion coefficient, D_s; the Nernst-Einstein relation,

$$\sigma_s = \frac{D_s c_s z_s^2 e_0^2}{k_\mathrm{B} T} \tag{2.25}$$

is implied. Using the above definitions and approximations, the particle flux in the presence of concentration and electrical potential gradients is written as

$$J_s = -D_s \nabla c_s - \frac{D_s c_s z_s e_0}{k_\mathrm{B} T} \nabla \phi \tag{2.26}$$

where J_{N_s} has been replaced by J_s for brevity. Equation 2.26 is referred to as the Nernst-Planck flux [131, 132, 145] and is used as the constitutive equation for the description of the point defect transport; magnetic field effects are not considered.
For the superposition of Fickian diffusion and drift of charged particles in the gradient of the electrostatic potential the label 'drift-diffusion' equations is also common in the literature.

The continuity equation with the Nernst-Planck flux solved self-consistently with the Poisson equation

$$\partial_t c_s = -\nabla \cdot J_s \tag{2.27}$$

$$\varepsilon_r \varepsilon_0 \nabla^2 \phi = -\rho \tag{2.28}$$

is referred to as the Poisson-Nernst-Planck (PNP) system of equations. For electron and hole transport in semiconductor device simulations a system of equations, mathematically equivalent to equations 2.26, 2.28, and 2.27 was first introduced by van Roosbroeck [182]. In the context of semiconductor device simulations these equations are typically referred to as drift-diffusion equations, and can be derived from the Boltzmann transport equation by either the Hilbert expansion or the moment method [112, 158]. The linear constitutive equations, like Fick's first law, have a phenomenological basis; however, they can also be thought of as laws of inference based on probability theory [55].

The nondimensionalization and mathematical scaling of the PNP system is described in what follows because it is essential for the numerical solution of the equations, which is further described in chapter 3. Table 2.1 contains the dimensional quantities occurring in the PNP system expressed in base units [9].

TABLE 2.1: Summary of the dimensional quantities occurring in the Poisson-Nernst-Planck system of equations. The chosen base unit system consists of length, ℓ, time, τ, amount of substance, N, charge, Q, and mass, M.

base units	ℓ_{ref}	t_{ref}	c_{ref}	ϕ_{ref}	D_{ref}	$k_{\text{B}}T$	e_0	$\varepsilon_r\varepsilon_0$
ℓ	1		-3	2	2	2		-3
τ		1		-2	-1	-2		2
N			1					1
Q				-1			1	1
M				1		1		-1

Reading table 2.1 as a matrix its nullspace yields three dimensionless groups in this problem

$$\Pi_1 = \frac{\ell_{\text{ref}}^2}{D_{\text{ref}} t_{\text{ref}}}, \quad \Pi_2 = \frac{k_{\text{B}}T}{e_0 \phi_{\text{ref}}}, \quad \Pi_3 = \frac{\varepsilon_r \varepsilon_0 \phi_{\text{ref}}}{e_0 \ell_{\text{ref}}^2} \tag{2.29}$$

which are not unique since any linear combination of the vectors spanning the nullspace yields a dimensionless group [9]. The reference length, time, and electrostatic potential are chosen based on physical and mathematical arguments, a discussion in the literature for the PNP system is given for example in reference [158] and references therein.

In this work D_{ref} is chosen as the maximum out of the diffusion coefficients of the mobile species

$$D_{\text{ref}} = \max_s \{D_s\}, \tag{2.30}$$

and c_{ref} as the maximum concentration of any species 's' within the domain. Furthermore, by choosing the film thickness as the reference length $\ell_{\text{ref}} = L$, the diffusion length as the reference timescale $t_{\text{ref}} = L^2/D_{\text{ref}}$, and the thermal voltage [158] as the reference electrostatic potential $\phi_{\text{ref}} = k_{\text{B}}T/e_0$, the dimensionless parameter, κ, is obtained

$$\kappa = \sqrt{\Pi_3} = \left(\frac{\varepsilon_r \varepsilon_0 k_{\text{B}} T}{e_0^2 c_{\text{ref}} L^2} \right)^{1/2} \tag{2.31}$$

that is not necessarily of magnitude 1; the groups $\Pi_1 = \Pi_2 = 1$, while $\Pi_3 \ll 1$ for thick films and or large defect concentrations. The parameter κ plays an important role in the behaviour of the PNP system. It is understood as the ratio between the reference screening length and the film thickness ℓ_{D}/L. The film thickness L and the reference screening length ℓ_{D} typically describe two vastly different length scales, both relevant

for the problem. The reference screening length, ℓ_{D}, is on the same order of magnitude as the Debye length which is discussed in the next section.

The drift velocity of particles with a charge e_0 migrating in the electric field is given by

$$v_{\text{drift}} = -\frac{D_{\text{ref}} e_0}{k_{\mathrm{B}} T} \nabla \phi. \tag{2.32}$$

During the time it takes the particles to diffuse a length L,

$$\tau_{\mathrm{d}} = L^2 / D_{\text{ref}}, \tag{2.33}$$

and in an electric field due to the thermal voltage, $k_{\mathrm{B}} T / e_0 L$, they drift the distance

$$\tau_{\mathrm{d}} v_{\text{drift}} = L, \tag{2.34}$$

which means that in a field due to the thermal voltage the particles drift and diffuse over equal lengths. Suggesting $k_{\mathrm{B}} T / e_0$ as a suitable reference magnitude for the electrostatic potential.

The validity of the Nernst-Planck flux expression is bound to the validity of the Boltzmann equilibrium distribution. Electrons adhere to the Fermi-Dirac distribution and in approximating it with the Boltzmann distribution one makes a transition from indistinguishable particles to classical distinguishable particles. The symmetry of the wavefunction taken into account by the Fermi-Dirac distribution introduces a statistical repulsion or exchange interaction in an ensemble of electrons. The spread of the wavepackets describing the electrons is on the order of the thermal wavelength

$$\lambda_T = \frac{h}{(2\pi m_{\mathrm{e}} k_{\mathrm{B}} T)^{1/2}} \tag{2.35}$$

The classical Boltzmann distribution neglecting the exchange interaction is therefore only applicable for interparticle distances much larger than the thermal wavelength and hence

$$\lambda_T c_{\text{ref}}^{1/3} \ll 1. \tag{2.36}$$

The Nernst-Planck flux expression is a ‘mean field approximation’, which describes the evolution of a large number of particles in terms of mean concentrations and a mean electrostatic potential potential obtaining a statistically averaged behaviour. It is of the

lowest order in the Bogoliubov-Born-Green-Kirkwood-Yvon hierarchy of kinetic equations [146]. The mean field approximation requires the potential energy of Coulomb interaction to be small compared to the kinetic energy of the particles. The Bjerrum length is defined as the distance at which the thermal kinetic energy equals the bare Coulomb interaction energy of two elementary charges

$$\lambda_{\mathrm{B}} = \frac{e_0^2}{4\pi\varepsilon_r\varepsilon_0 k_B T} \tag{2.37}$$

Only if the average interparticle distance, $c_{\mathrm{ref}}^{-1/3}$, is much greater than the Bjerrum length can the electron-electron correlation be neglected, and hence if

$$\lambda_{\mathrm{B}} c_{\mathrm{ref}}^{1/3} \ll 1 \tag{2.38}$$

is the mean field approximation applicable in this problem; the pair interactions between discrete ions are replaced by a continuum mean field theory.

The Nernst-Planck flux relies on a linearization of the Maxwell-Boltzmann distribution that holds if

$$\left| \frac{e_0\,\delta\phi}{k_{\mathrm{B}} T} \right| \ll 1 \tag{2.39}$$

where $\delta\phi$ is the potential difference between two defect hopping sites. The thermodynamic driving force for the transport problems considered in this work, $k_{\mathrm{B}} T \ln\left(P^{II}/P^{I}\right)$, is determined by the ratio of the oxidant pressures at the metal–scale, P^{I}, and scale–environment, P^{II}, interface. The developing electrostatic potential difference across the film is typically on the order of the thermal voltage, $\Delta\phi \sim k_{\mathrm{B}} T/e_0$, and the above criterion will certainly hold unless the thickness of the film approaches the hopping distance of the mobile ionic or electronic species. For local thermodynamic equilibrium to be maintained in a thermodynamic subsystem or 'cell' subject to a thermodynamic force, the relative magnitude of the thermodynamic force across the cell must be small compared to the statistical fluctuations [146].

The above assumptions and limits are expected to be unproblematic in most oxides but have to be examined carefully when calculating transport rates in strongly correlated oxides and sulfides. A phenomenological approach to transport in sulfides and transition metal oxides was given by Wagner [193], where linear irreversible thermodynamic fluxes including cross-terms are discussed; oxidation of transition metals is reviewed in [163].

2.6.2 Debye-Hückel screening

Considering the surface of a homogeneous material a gradient in the chemical potential of a species mobile within the material can be generated by varying the chemical properties of the environment which impose the boundary conditions for the species transport within the material. After a transient period a self-consistent electric field is present opposing the chemical potential gradient, such that the distance particles diffuse in the chemical potential gradient during a particular time equals the distance they drift in the gradient of the electrical potential during the same time, requiring,

$$\nabla \mu_s = -z_s e_0 \nabla \phi, \tag{2.40}$$

which characterizes this dynamic equilibrium state, and consequently, the flux vanishes locally

$$J_s(r) = 0. \tag{2.41}$$

For an ideal dilute solution where

$$\nabla \mu_s = \frac{k_\mathrm{B} T}{c_s} \nabla c_s \tag{2.42}$$

the equilibrium relation 2.40 can be integrated and yields the Boltzmann form distribution for the concentrations

$$c_s(r) = c_s^0 \, \exp\left(-\frac{z_s e_0 \, \phi(r)}{k_\mathrm{B} T} \right) \tag{2.43}$$

where c_s^0 denotes the reference concentrations in the bulk material unperturbed by the chemical environment that satisfy,

$$\sum_s z_s c_s^0 = 0, \tag{2.44}$$

and the electrostatic potential reference in bulk is set to zero for convenience. The self-consistent electrostatic potential, ϕ, can be calculated from the Poisson equation with the charge density generated by the concentrations 2.43,

$$\varepsilon_r \varepsilon_0 \nabla^2 \phi = -\sum_s z_s e_0 c_s^0 \, \exp\left(-\frac{z_s e_0 \, \phi}{k_\mathrm{B} T} \right) \tag{2.45}$$

which is referred to as the Poisson-Boltzmann equation in the literature. In the limit of

$$\left| \frac{e_0 \, \delta\phi}{k_{\mathrm{B}} T} \right| \ll 1 \tag{2.46}$$

that has already been introduced as a necessary condition for the validity of the Nernst-Planck flux, see section 2.6.1, the Poisson-Boltzmann equation is linearized and reduces to the Helmholtz equation

$$\left(\nabla^2 - \lambda_{\mathrm{D}}^{-2} \right) \phi = 0 \tag{2.47}$$

where the Debye length

$$\lambda_{\mathrm{D}} = \left(\frac{\varepsilon_r \varepsilon_0 \, k_{\mathrm{B}} T}{e_0^2 \sum_s z_s^2 c_s^0} \right)^{1/2} \tag{2.48}$$

is defined. It is the length scale for spatial variations of $\phi(r)$ and $\rho(r)$ near the interfaces. The Debye length was identified in the famous treatment of ionic liquids by Debye and Hückel [30], and describes the characteristic length scale for classical Coulomb screening. The free energy change due to screening is negative and the screened state is the equilibrium state corresponding to the free energy minimum with respect to the possible induced charge distributions.

The equation 2.47 has been applied to different physical phenomena distinguished by the corresponding boundary conditions imposed on equation 2.47. A simple case is given by a uniformly charged surface, the electrostatic potential decays as

$$\phi(x) \sim \exp(-|x|/\lambda_{\mathrm{D}}) \tag{2.49}$$

near the surface, as a function of the distance $|x|$ to the surface. The charge density behaves similarly.

As noted by Onsager [141] the linearization of the Boltzmann form distribution in the Debye-Hückel treatment of screening is indeed necessary to obtain a self-consistent theory [95]. An extensive discussion of Coulomb screening effects in material science applications can be found in [18].

2.7 Membrane permeation

Membrane permeation is a more general problem than metal oxidation in the sense that two environments of the membrane can be chosen freely, but it is substantially less

complicated because unlike in the scale growth problem the position of the interfaces is typically fixed. However, in this work scale growth is typically considered under conditions of steady-state growth and under such conditions membrane permeation and scale growth are similar phenomena from a modelling point of view.

A recent series of oxygen permeation experiments on polycrystalline α-Al_2O_3 membranes [83, 84] has provided new insight into grain boundary diffusion in alumina, a material whose diffusion properties have been investigated since decades [68, 70, 71]. The experimental results will be summarized briefly in the following section.

2.7.1 Alumina membrane oxygen permeation experiments

The permeation rates of oxygen through a polycrystalline membrane of alumina have been reported in the literature [83, 84], and cover a range of oxygen partial pressures. Scanning Electron Microscope (SEM) imaging of the films prepared under different applied pressures strongly suggests that mass transfer occurs along grain boundaries. The thermodynamic driving force in these experiments is the difference in the oxygen chemical potential between the two membrane surfaces $\Delta\mu_{O_2} = k_B T \ln\left(P^{II}_{O_2}/P^{I}_{O_2}\right)$. Figure 4.4 shows a schematic of membrane permeation experiments.

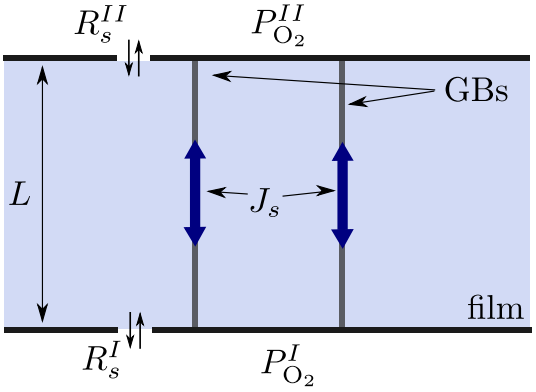

FIGURE 2.4: Schematic of the membrane permeation experiments where mass transfer occurs by grain boundary transport. Different oxygen gas partial pressures, $P^{I}_{O_2}$ and $P^{II}_{O_2}$, are applied on the surfaces. R^{I}_{s} and R^{II}_{s} denote the interfacial reactions.

The experiments included nominally pure α-alumina polycrystals [84, 188], doped α-alumina polycrystals [85, 115–117], and nominally pure α-alumina bicrystals [114], with temperatures of $\sim 1700 - 2000$ K. A simple analysis of the permeation rate data in reference [84], assumed a model of one-dimensional, steady-state diffusion, in which either Al or O is transported by vacancy migration, depending on the absolute magnitude of the applied oxygen pressure.

In the non-doped polycrystalline alumina experiments [84], when applying high oxygen pressures at surface (II), $P_{O_2}^{\text{hi}} = 10^3 - 10^5$ Pa, while keeping surface (I) at $P_{O_2}^{I} = 1$ Pa, grain boundary ridges formed on the $P_{O_2}^{\text{hi}}$ surface and grain boundary trenches were observed on surface (I). Applying a low oxygen pressure at surface (II), $P_{O_2}^{\text{lo}} = 10^{-5} - 10^{-8}$ Pa, while keeping surface (I) at $P_{O_2}^{I} = 1$ Pa, no grain boundary ridges are formed and only grain boundary trenches are observed. Since the oxygen permeation rates of a single-crystal alumina wafer were below the measurable limit and as the visible surface growth and 'dissolution' proceeds at grain boundaries it is reasonable to assume that grain boundaries dominate the transport [84]. The oxygen permeation rates, P, for fixed $P_{O_2}^{I} = 1$ Pa were found to follow distinct power laws [84]; in the limit of $P_{O_2} = P_{O_2}^{\text{hi}}$ at (II),

$$P \sim P_{O_2}^{3/16}, \tag{2.50}$$

and in the limit of $P_{O_2} = P_{O_2}^{\text{lo}}$ at (II),

$$P \sim P_{O_2}^{-1/6}. \tag{2.51}$$

The power laws and the pressure dependent formation of the grain boundary ridges have led to the interpretation of the experiments in terms of, aluminum vacancy transport being dominant in oxygen chemical potential gradients with high oxygen pressure magnitude, $P_{O_2}^{II} = P_{O_2}^{\text{hi}}$, and oxygen vacancy transport being dominant in the case of $P_{O_2}^{II} = P_{O_2}^{\text{lo}}$.

Indeed, the rational power laws appear in the theory as a direct consequence of the +3 and -2 ionic charges of the ions, assuming that the negative of these charges is carried by each vacancy, with a counter-current of electrons or holes, and no time-dependence of the fluxes (the steady-state assumption) or net local charge densities within the grain boundaries. These assumptions are discussed further in section 3.4.1. Furthermore, only aluminum vacancy transport can lead to ridge formation, which is observed by SEM imaging in the case of $P_{O_2}^{II} = P_{O_2}^{\text{hi}}$, supporting the above interpretation. The switch-over in dominant point defect species in the grain boundary has been termed '$p - n$ transition' in the literature [70, 71].

The diffusion coefficients determined from alumina bicrystal experiments with $P_{O_2}^{II}/P_{O_2}^{I} = 10^5$ Pa$/1$ Pa for several distinct grain boundary types have been found compatible with those measured in polycrystalline samples [114]. The bicrystal diffusion coefficients were calculated from the grain boundary ridge volume and a caveat regarding this approach is that the formation of the ridges on the $P_{O_2}^{\text{hi}}$ side does not necessarily

imply an exactly equivalent mass transport from the opposite side of the membrane, since oxide can be displaced by formation of internal pores in the subsurface region of the crystals, as has indeed been observed in some polycrystal permeation experiments [116].

The above level of analysis leaves several open questions, e.g. does the grain boundary diffusion mechanism, with the associated inhomogeneity of fluxes and electric fields, map accurately onto a 1D diffusion problem? And what are the magnitude and roles of the surface and interface charges, the electric fields, currents, space charges, and transients that are all believed to be present in a three-dimensional film, traversed by grain boundaries?

These questions are addressed in chapter 3, where the transport of oxygen through a planar film with an idealized grain structure is studied. In the novel model presented the grains are supposed to be columnar, with identical and perfectly hexagonal cross sections, see figure 3.1. A set of coupled reaction-diffusion equations is used to model the oxygen permeability across the membrane, the model is described in section 3.2, and the results obtained for the model alumina membrane are found in section 3.4.

Chapter 3

The hexagonal cell model

3.1 Introduction

Thin films of insulating material at metal – gas and metal – liquid interfaces accomplish a range of service functions in materials technology. Common examples are functional ceramics in electronics, energy related applications and sensors. Thin films formed by surface oxidation of a metal can have either beneficial or corrosive effects. Alumina and chromia formed by thermal oxidation are examples of protective oxide films, which find application in thermal barrier coatings, and can be engineered for durability by additions of rare earth elements [37, 130, 142, 168]. They can also grow in an uncontrolled manner, adhering weakly to the metal and allowing corrosion to proceed. While the slowest process is rate-determining for consecutive processes, like dissociation of oxygen molecules and their transport through the oxide, the fastest process is rate-determining for parallel processes, like bulk and grain boundary diffusion through the oxide.

The measured oxygen and aluminum diffusion coefficients in α-alumina are found to be several orders of magnitude greater at the grain boundaries than in the bulk material [68, 69, 71]. The fact that grain boundaries provide the dominant transport mechanism underlines the importance of including their geometric and transport properties in a realistic model of the process. Oxides grow in various polycrystalline or even amorphous structures during metal oxidation. In dry high-temperature oxidation columnar grain structures are frequently found. In the model presented here the granular structure of a film, scale or membrane is idealized as a 2D periodic pattern of hexagonal cells. Since vacancies in strongly ionic oxides such as alumina or chromia are charged species relative to the perfect crystal, the fluxes of these species carry an electric current, which in the usual scenario of steady-state growth is not sustainable, unless compensated by

an equal and opposite current of electrons or holes, as described by the classic model of Wagner [2, 189]. The prediction of the growth behaviour of thin films, and its influence on the material or device performance, requires us to describe the mixed ionic, electronic transport through the films, while taking their grain boundary structure into account.

Because of the widespread importance of alumina films [31], and since it is a relatively well characterized material, the focus here is on alumina films for the validation of our modelling approach. Moreover, a recent series of permeation experiments for α-alumina polycrystalline membranes, e.g. [84], conducted for different combinations of applied oxygen gas pressures at high temperatures, provides an ideal test case for our transport model. The chapter is organized as follows.

In section 3.2, the model is defined; its geometry, and the mathematical formulation of the transport and the reaction boundary conditions are described. In section 3.3, the numerical solution technique and the computational implementation are summarized.

In section 3.4, the hexagonal cell model is applied to membrane oxygen permeation experiments and the simulation results are compared to the experimental results that have been summarized in chapter 2 section 2.7.1.

In section 3.5, the model is extended to include internal oxidation and the consequential generation of stress at the grain boundaries. Related experimental findings, modelling approaches, and the essential theoretical background for a thermodynamic description of stressed solids are provided in sections 3.5.2, 3.5.4, and 3.5.3, respectively.

The model and the results presented in section 3.4 have been the subject of a publication by the present author [175].

3.2 The model

The model is expected to be applicable to different granular materials and is particularly suitable to investigate transport in films with columnar grain structure. The model is applied here to investigate membrane permeation and metal oxidation but should also be readily adaptable to problems such as transport in solid state electrodes. Within the hexagonal cell geometry, which is discussed below, grain boundary transport through the film of charged point defects, electrons, and holes is simulated, while reactions with the environment constitute the boundary conditions.

3.2.1 2D-periodic hexagonal prism grain structure

The columnar grains are idealized as hexagonal prisms, with the rectangular faces denoting the grain boundaries, see figure 3.1. The hexagonal prisms are periodically repeated to construct a slab of infinite extent in two dimensions.

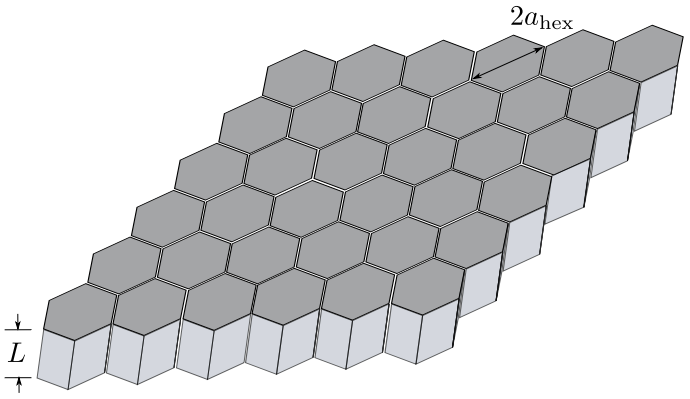

FIGURE 3.1: Section of the slab with thickness, L, composed of hexagonal cells of side length, a_{hex}.

Transport through the slab is presumed to be dominated by that through the rectangular grain boundaries, located at the interfaces between the cells. The grain boundaries are assumed to be composed of a very thin homogeneous and isotropic medium of finite width δ. The width of the boundary is not a physical width, but rather a theoretical construct, which allows concentrations to be expressed per unit of volume or per atomic site rather than per unit of area.

From the symmetry of the system only the 'irreducible zone' of the hexagonal cell, shown in figure 3.2, needs to be considered as a domain for calculation. It includes a triangular piece of the surface hexagon and half of a grain boundary rectangle. The 2D-periodic tiling enables an explicit calculation of the long-range Coulomb interaction between the charged point defects.

3.2.2 Grain-boundary transport

The point defect concentrations within the boundary are assumed to be continuous functions of space and time. Based on the local equilibrium hypothesis the electrochemical potential, η_s, of point defects, and electrons or holes of species 's', is given by

$$\eta_s(r,t) = \mu_s(r,t) + z_s e_0\, \phi(r,t) \tag{3.1}$$

where, μ_s is the chemical potential of species s, ϕ is the electrostatic potential, z_s is the charge (integer number), e_0 is the positive elementary charge, and r is the position vector. As discussed in section 2.6, the particle flux due to a gradient in the electrochemical potential may be written as,

$$J_s = -\frac{D_s c_s}{k_\mathrm{B} T} \nabla \eta_s \tag{3.2}$$

which in the ideal solution approximation [15] is equivalent to

$$J_s = -D_s \nabla c_s - \frac{D_s c_s z_s e_0}{k_\mathrm{B} T} \nabla \phi \tag{3.3}$$

where D_s is the diffusion coefficient, and $c_s(r,t)$ is the concentration (number per unit volume) of species s. Equation 3.3 is referred to as the Nernst-Planck flux, and combines Ohm's law of conduction and Fick's law of diffusion. It is used here as the constitutive equation for the description of the point defect transport; magnetic field effects are not considered.

The local charge density is given by

$$\rho(r,t) = \sum_s z_s e_0 \, c_s(r,t) \tag{3.4}$$

where the sum is performed over all charged species present. The instantaneous electrostatic potential can be calculated from the charge density by solving Poisson's equation, which is given here in integral form for a linear dielectric material,

$$\phi(r,t) = \frac{1}{4\pi\varepsilon_0\varepsilon_r} \int_{\mathbb{V}} \frac{\rho(r',t)}{|r-r'|} d^3 r' \tag{3.5}$$

where ε_0 and ε_r are the vacuum and relative permittivity respectively, and the domain of integration $\mathbb{V}$ of the 'Coulomb integral' includes the entire system, in which charge densities are non-zero within a slab of infinite extent in two dimensions, composed of identical hexagonal cells and their surfaces. Overall charge neutrality holds for the domain $\mathbb{V}$, at any instant of time

$$\int_{\mathbb{V}} \rho(r,t) d^3 r = 0. \tag{3.6}$$

The continuity equations for the individual species are given by

$$\frac{\partial}{\partial t} c_s = -\nabla \cdot J_s + R_s \tag{3.7}$$

where a reaction term, R_s, has been added to enable processes such as electron and hole recombination within the grain boundary to be described. The continuity equations for the different mobile species are used in the simulations to evolve the defect concentrations in time; they are solved self-consistently with the equation for the electrostatic potential 3.5, which depends on the charge density $\rho(r,t)$.

To model coupling effects in the species transport the dynamics could be formulated in terms of linear irreversible thermodynamics [139, 146], but this theory does not provide explicit expressions for the constitutive equations including the transport coefficients. The linear constitutive equations, like Fick's first law, have a phenomenological basis; however, they can also be thought of as laws of inference based on probability theory [55].

The equations describing time-dependent diffusion of ions, electrons and holes through a polycrystalline film, driven by electric fields and defect concentration gradients, cannot be solved analytically in general, and numerical methods must be applied. Models including numerical computations to describe transport through films have been developed for homogeneous films [10, 13, 50], for which a one dimensional model may be a suitable approximation. The symmetry of the present model of idealized columnar hexagonal grains is used to reduce the problem to 2D boundary diffusion along the rectangular boundaries of the hexagonal grains, while explicitly taking account of the long-ranged electrostatic interactions between the charged species within the 3D structure. In order to be able to describe transient behaviour and time-dependent environments, time-dependent boundary conditions are taken into account, but the movement of the boundaries is neglected. This means surface charges can build up or be depleted as a function of time, due to the reactions with oxygen in the environment, in our case a prescribed oxygen partial pressure, and the delivery of charged species to the surfaces from the grain boundaries.

The system of equations used in our model to describe the fluxes of point defects, electrons and holes and their Coulomb interaction, see also section 2.6, is mathematically equivalent to the drift-diffusion (DD) equations applied in semiconductor device simulations for electron and hole transport [112, 158], and to the Poisson-Nernst-Planck (PNP) system, which is used for ion channel simulations [33, 34] and other electrochemical applications [12]. Unlike most computational methods of solution for the DD and PNP equations, which solve the Poisson equation in differential form and often only consider the steady-state solution, the solution method developed here allows for time-dependent calculations and the Poisson equation is solved in its integral form, taking into account the long-range Coulomb interaction within the 3D structure.

3.2.3 Time dependent boundary conditions

The boundary conditions are formulated to describe oxide creation and dissolution at the slab surfaces by reaction with the environment. We refer to our system, which includes its upper and lower surfaces, as 'the slab'. The thin surface layers of the slab are treated as a homogeneous and isotropic medium of thickness δ. The flux of defects between the surfaces and the grain boundary, and the reactions between the slab and the environment, change the concentrations of species s in the surface layers, $\mathcal{C}_s$, as expressed by

$$\int_{\mathbb{V}_{\text{TRI}}} \frac{\partial \mathcal{C}_s}{\partial t}\, d^3r = \int_{\mathbb{A}_{\text{GB}}} J_s \cdot \hat{n}\, d^2r + \int_{\mathbb{V}_{\text{TRI}}} \mathcal{R}_s\, d^3r. \tag{3.8}$$

Reactions between the slab surface and the environment produce species s in the surface layer at a rate $\mathcal{R}_s$. The unit normal, $\hat{n}$, and the integration domains are defined in figure 3.3. Equation 3.8 holds for all species 's' and separately for the surfaces (I) at $x_3 = 0$ and (II) at $x_3 = L$.

Assuming transport to be much faster across the surface than between surface and grain boundary, uniform defect concentrations are used on the surfaces. This leads to the following simplification of equation 3.8

$$\frac{\partial}{\partial t}\mathcal{C}_s = \frac{1}{\mathbb{V}_{\text{TRI}}} \int_{\mathbb{A}_{GB}} J_s \cdot \hat{n}\, d^2r + \mathcal{R}_s \tag{3.9}$$

which is used as the boundary condition in the simulations reported below. If the surface transport mechanism and parameters are known it is straightforward to relax the above assumption.

No separate boundary condition is needed for the electrostatic potential since it is calculated by a summation technique, only requiring the instantaneous charge distribution as a function of position. The reaction rates in the grain boundary, R_s, and on the surface, $\mathcal{R}_s$, depend on the application of the model. For the present purpose of describing the alumina permeation experiments the rate equations are derived with the law of mass action, and discussed in more detail in section 3.4.2.1. The application to oxide scale growth will require a separate boundary condition at the interface between oxide and metal.

The initial conditions also depend on the application. For the oxygen permeation experiments they are discussed in section 3.4.3.1.

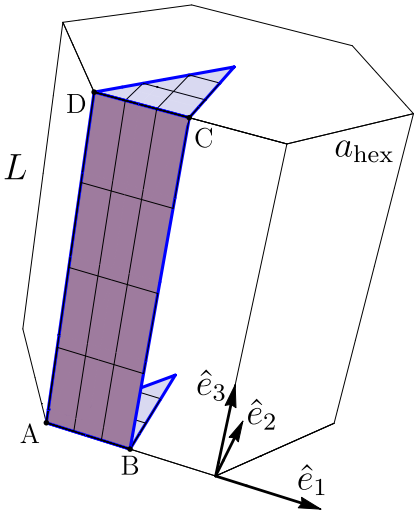

FIGURE 3.2: Irreducible zone of the hexagonal cell. The grain boundary rectangle, enclosed by $\overline{ABCD}$, is indicated. The coordinate system is defined.

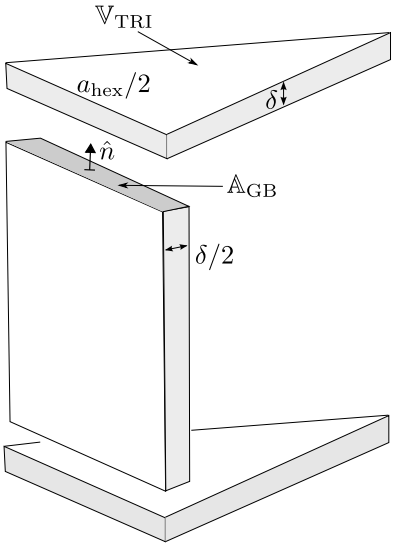

FIGURE 3.3: Exploded-view of the irreducible zone of the hexagonal lattice defining the surface and grain boundary domains. The grain boundary thickness, δ, which is equal to the surface layer thickness, δ, the grain boundary cross-section, $\mathbb{A}_{\text{GB}}$, the outward pointing unit normal, $\hat{n}$, and the volume of the surface triangle, $\mathbb{V}_{\text{TRI}}$, are indicated. Drawn out of proportion, since in general $\delta \ll a_{\text{hex}}$.

3.3 Method of solution

An object oriented C++ code has been developed to solve the system of coupled partial differential equations 3.3, 3.7, and 3.9, self-consistently with the Coulomb integral, equations 3.4, and 3.5, which is approximated by the summation technique described in section 3.4.4. Since the system of equations is nonlinear, involves vastly different rates in the diffusion processes and the reactions, and involves different length scales characterized by the Debye length, defined below, and the system size, this is a challenging computational problem.

3.3.1 Dimensionless equations

To obtain dimensionless equations for the numerical calculations the variables, parameters, and fields are scaled as follows [158]:

$$\begin{aligned} r &= \frac{1}{L}\,\widetilde{r}, \quad D_s = \frac{1}{D_{\text{ref}}}\,\widetilde{D}_s, \quad c_s(r,t) = \frac{1}{c_{\text{ref}}}\,\widetilde{c}_s, \\ t &= \frac{D_{\text{ref}}}{L^2}\,\widetilde{t}, \quad \phi(r,t) = \frac{e_0}{k_{\text{B}}T}\,\widetilde{\phi}, \end{aligned} \tag{3.10}$$

where L is the thickness of the scale; $D_{\text{ref}} = \max\{D_s\}$ is the largest diffusion coefficient for all species; c_{ref} is a suitable reference concentration; and e_0 is the elementary positive charge. To avoid unnecessarily heavy notation, the original quantities were denoted with the 'tilde' mark over the symbol in the definition of the scaling, and the dimensionless quantities without the tilde are used in the following.

With the scaling defined by equations 3.10, the system of transport equations and the Coulomb integral can be brought into dimensionless form

$$\frac{\partial}{\partial t}c_s = -\nabla\cdot(-D_s\nabla c_s - D_s z_s c_s \nabla\phi) \tag{3.11a}$$

$$\kappa^2\phi(r,t) = \frac{1}{4\pi}\int_{\mathbb{V}} \frac{\sum_s z_s c_s(r',t)}{|r-r'|} d^3r' \tag{3.11b}$$

where the dimensionless parameter, κ,

$$\kappa = \frac{\ell_{\text{D}}}{L}, \qquad \ell_{\text{D}} = \left(\frac{\varepsilon_0\varepsilon_r k_{\text{B}}T}{e_0^2\, c_{\text{ref}}}\right)^{1/2} \tag{3.12}$$

and the reference screening length, ℓ_{D}, are introduced. L denotes the thickness of the slab, see figure 3.1. The Debye screening length is defined by

$$\lambda_{\text{D}} = \left(\frac{\varepsilon_0\varepsilon_r k_{\text{B}}T}{e_0^2\sum_s z_s^2 c_s^0}\right)^{1/2} \tag{3.13}$$

where c_s^0 are the spatially uniform concentrations obtained in the limit of $T\to\infty$, while holding the total number of each species, N_s, constant. In the application considered in this work the oxygen gas chemical potentials are fixed at the surfaces, the concentrations, $c_s(r,t)$, are independent variables, and the total number of each species depends on time, $N_s(t)$; however, c_{ref} is chosen such that ℓ_{D} has similar magnitude to λ_{D}, and ℓ_{D} is therefore referred to as the reference screening length.

Overall charge conservation and zero total charge within the system are maintained during the evolution of the concentrations, while charge is redistributed within

the grain boundary and moved in or out of the surfaces by the fluxes.

3.3.2 Discretization of the transport equation

The finite difference method is used to discretize the continuum equations in space and time [94, 158]. For the spatial discretization a rectangular mesh is used, and it covers the irreducible zone of the hexagonal cell, indicated in figure 3.2. The concentrations and electrostatic potential at mesh node (i, j) at position $r(x_1^i, x_3^j)$ in the grain boundary ($x_2 = 0$) and discrete time t_n are denoted by, $c_s(x_1^i, x_3^j, t_n) = c_s^{i,j,n}$, and $\phi(x_1^i, x_3^j, t_n) = \phi^{i,j,n}$, respectively, where $i = 1, 2, ..., N_1$ and $j = 1, 2, ..., N_3$.

The mesh spacings near the surfaces need to be significantly smaller than the reference screening length to resolve the behaviour near the surfaces correctly. However, the whole grain boundary cannot be meshed with such a fine spacing in the $\hat{e}_3$ direction, because the summation technique used for calculating the Coulomb interaction would become too computationally expensive. Therefore, a layer-adapted mesh is used in the $\hat{e}_3$ direction.

The Nernst-Planck flux in equation 3.3 is approximated with the Scharfetter-Gummel discretization scheme [154]; in one dimension for fixed j it is given by

$$J_s^{i+1/2,j,n} = - D_s \frac{c_s^{i+1,j,n}\, \mathrm{B}\left(-z_s \Delta\phi^{i,j,n}\right) - c_s^{i,j,n}\, \mathrm{B}\left(z_s \Delta\phi^{i,j,n}\right)}{\Delta x_1^i} \tag{3.14}$$

where $J_s^{i+1/2,j,n}$ is the flux of species s between node i and $i+1$ at time t_n, $\Delta x_1^i = x_1^{i+1} - x_1^i$ is the length of the interval, $\Delta\phi^{i,j,n} = \phi^{i+1,j,n} - \phi^{i,j,n}$ is the potential difference between the mesh nodes at time t_n, and $\mathrm{B}(x) = x/(\exp(x) - 1)$ is the Bernoulli function [158]. For the time stepping the continuity equation 3.7 is discretized in implicit form,

$$\begin{aligned} & c_s^{i,j,n} - c_s^{i,j,n-1} + \frac{\Delta t_n}{\Delta \overline{x}_1^i} \left(J_s^{i+1/2,j,n} - J_s^{i-1/2,j,n} \right) + \\ & \frac{\Delta t_n}{\Delta \overline{x}_3^j} \left(J_s^{i,j+1/2,n} - J_s^{i,j-1/2,n} \right) - \Delta t_n R_s^{i,j,n} = 0 \end{aligned} \tag{3.15}$$

where $\Delta \overline{x}_1^i = (\Delta x_1^i + \Delta x_1^{i-1})/2$, $\Delta \overline{x}_3^j = (\Delta x_3^j + \Delta x_3^{j-1})/2$, and $\Delta t_n = t_n - t_{n-1}$. The initial time step, Δt_1, is chosen such that the discretizations in space and time have a similar order of accuracy, hence $\Delta t_1 \approx (\Delta x_{\min})^2$ where $\Delta x_{\min}$ denotes the smallest mesh element. $\Delta x_{\min}$ is chosen to have the same size as the surface layer thickness, $\delta = 1\,\mathrm{nm}$, and for a film thickness of $L = 1\,\mu\mathrm{m}$ the smallest mesh element is given

by $\Delta x_{\min} = 10^{-3}$ in units of the film thickness, L. Therefore, typically $\Delta t_1 = 10^{-6}$ and the time step is subsequently increased adaptively, to improve efficiency of the procedure while ensuring convergence at each time step. The maximum time step is typically $\Delta t_{\max} \sim 0.1$ which allows calculations to be performed long enough to reach steady-state conditions without the need for exceptional computational resources.

3.3.3 Calculation of the long-range Coulomb interaction

Since the functions $c_s(r,t)$ are discretized in space and time the Coulomb integral in equation 3.11b can be approximated with a summation technique. In this section the concentration at the mesh nodes is abbreviated as $c_s(r_j,t_n) = c_s(x_1^{j_1}, x_2^{j_2}, x_3^{j_3}, t_n) = c_s^{j,n}$, with the composite index $j = (j_1, j_2, j_3)$, and in the same way $c_s(r_i,t_n) = c_s^{i,n}$. The volume element corresponding to mesh node j is denoted by, ν_j. The charge density in the volume, ν_j, around mesh node j is turned into a point charge, $q^{j,n} = \sum_s z_s\, c_s^{j,n}\, \nu_j$, placed at position r_j. With this definition the Coulomb integral is converted into the Coulomb sum

$$\phi(r,t_n) = \kappa^{-2} \sum_j^{\mathbb{V}\prime} \frac{\sum_s z_s\, c_s^{j,n}\, \nu_j}{|r - r_j|} \tag{3.16}$$

where $\phi(r,t_n)$ is still a continuous function of space, and it can only be evaluated at the discrete times, t_n, since the $c_s^{j,n}$ are only known at discrete times t_n. The prime indicates that the possible term $r = r_j$ is excluded from the summation. The summation index j runs over all volume elements of the infinite slab, and since the potential decays with r^{-1}, the sum is only slowly and conditionally convergent; it cannot be trivially truncated. Therefore, the Parry summation technique [143, 144], which is an Ewald summation technique for 2D periodic systems, is used. In this technique the sum is split into a real and a Fourier (reciprocal) space part, the short-range interactions are evaluated in real space and the long-range interactions are evaluated in Fourier space. The advantage is rapid convergence compared to the direct summation.

The rhombus shown in figure 3.4 is defined as the repeat unit of the 2D periodic tiling, and the rhombohedral prism shown in figure 3.5 is a repeat unit of the infinite slab, used to carry out the Parry summation. The symmetry of the hexagonal prism, with distinct hexagonal surfaces on the top and bottom surface, is used to increase the computational efficiency of the evaluation of the Coulomb sum.

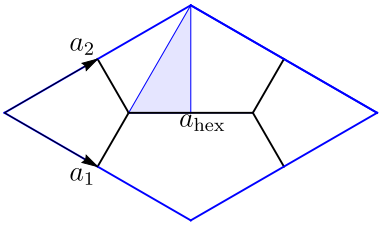

FIGURE 3.4: A 2D repeat unit of the hexagonal tiling used in the simulations. The shaded area is the irreducible zone of the surface, referred to as the surface triangle.

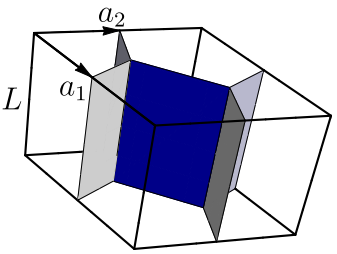

FIGURE 3.5: A 3D repeat unit of the infinite slab, seen in plan view in figure 3.4. The shaded planes indicate the grain boundaries within the repeat unit.

During a calculation the charge density changes with time and the potential needs to be updated with the changing charge density; however, the geometry of the hexagonal structure and the mesh do not change. Therefore, the Parry summation is performed only once, at the beginning of the calculations, to determine the Green's function for the given mesh and periodic cell structure. The Green's function is calculated for unit charges on the individual mesh nodes, and is stored as a matrix, g_{ij}, for the nodes of the irreducible zone, where g_{ij} denotes the potential at node i due to a unit charge and all its images, generated by symmetry and periodicity, at node j. During the time-dependent calculations, the potential is calculated by summing the discretized charge density, multiplied by the Green's function, over the nodes of the irreducible zone,

$$\phi(r_i, t_n) = \sum_j q^{j,n} g_{ij} \,. \tag{3.17}$$

This strategy greatly reduces the computational cost of evaluating the Coulomb integral.

A stretched mesh with variable mesh spacings, which are different in the $\hat{e}_1$ and $\hat{e}_3$ direction, is found to lead to divergence problems when performing the summation over the point charges, $q^{j,n}$. Therefore, 'Gaussian smearing' is used for the charge densities at the individual mesh nodes. The local charge density at mesh node j and discrete time t_n, $\rho(r_j, t_n)$, is replaced by a normalized Gaussian distribution

$$\rho_g(r, r_j, t_n) = \rho(r_j, t_n) \left(\frac{\beta}{\pi}\right)^{\frac{3}{2}} \exp(-\beta |r - r_j|^2) \tag{3.18}$$

where $\beta = (2\sigma^2)^{-1}$ and σ is the width of the Gaussian centered around r_j. With the

Gaussian distribution the electrostatic potential contributed by the charge density corresponding to mesh node j takes the form

$$\phi_g(r, r_j, t_n) = \kappa^{-2} \frac{q^{j,n}}{|r - r_j|} \text{erf}(\sqrt{\beta}|r - r_j|). \tag{3.19}$$

In the limit of $|r - r_j| \to 0$ the electrostatic potential contributed by the charge density centred on mesh node j itself becomes

$$\phi_g(|r - r_j| \to 0, t_n) = 2\,\kappa^{-2} \left(\frac{\beta}{\pi}\right)^{\frac{1}{2}} q^{j,n}, \tag{3.20}$$

which has to be added to the potential at this node generated by all the other charges in the system. The width σ of the Gaussians is chosen to be that of the smallest mesh spacing in the slab.

3.3.4 Iterative solver for the self-consistent calculations

A multidimensional Newton method is used to solve the nonlinear system of discretized equations, including the continuity equations for all species on all mesh points, their boundary conditions, and the Coulomb summation to obtain the self-consistent electrostatic potential value at each mesh point. Depending on the number of mesh points and the number of species the system, which needs to be solved in every time step, can contain several thousand variables. Therefore, the Jacobian-Free-Newton-Krylov (JFNK) method from the NOX package of the Trilinos Project [66] is used. JFNK methods are nested iteration methods and can achieve Newton-like convergence without the cost of forming and storing the true Jacobian required for ordinary Newton methods [86].

3.4 Diffusion of oxygen through an alumina membrane

Oxygen membrane permeation or diffusion through an oxide film is a non-equilibrium process, involving oxygen exchange and electron transfer reactions at the oxide surfaces and the transport of defects between the surfaces.

3.4.1 1D analytic model for the permeation rate

The 1D analytic model and its derivation is discussed in more detail in chapter 4 section 4.3.2. The given derivation the oxygen permeation rate emphasizes the role of the electric field for the establishment of approximately stoichiometric proportions for the

dominant vacancy and electronic species of the surface concentrations, $\mathcal{C}_s$, which determine the permeation rate, and the appearance of an effective (ambipolar) diffusion coefficient, see also section 4.3.2.2, in the presence of the self-consistent electric field.

The concentrations of the defect species on the surfaces exposed to the oxygen gas environment, characterized by the oxygen partial pressure and the temperature, evolve over time and depend on the reactions taking place and the transport to and from the surfaces. At the oxide – gas interface the absorption (desorption) of oxygen and creation (annihilation) of aluminum vacancies can be described by

$$\frac{1}{2}\mathrm{O}_2(g) + 2\mathrm{e} \underset{k_{\mathrm{Al},b}}{\overset{k_{\mathrm{Al},f}}{\rightleftharpoons}} \mathrm{O}_{\mathrm{O}}^{\times} + \frac{2}{3}\,\mathrm{V}_{\mathrm{Al}}^{3\text{-}}\,. \tag{3.21}$$

For the purpose of a simple analytical treatment it is assumed that a steady-state is reached at the surfaces, in which Schottky and electron-hole equilibrium, see reactions 3.35 and 3.36, characterized by the equilibrium constants K_{S} and K_{eh}, respectively, are attained. The reaction 3.21 could be formulated with holes instead of electrons, however, assuming instantaneous equilibration between electrons and holes both formulations yield identical results. At high applied oxygen gas partial pressures, aluminum vacancies are formed predominantly at the surface and oxygen vacancies are annihilated, with the reverse scenario applying for low oxygen partial pressures. Since instantaneous Schottky equilibration is assumed at the surfaces no additional reaction is required involving oxygen incorporation by oxygen vacancy annihilation. In reaction 3.21 for $P_{\mathrm{O}_2}^{\mathrm{hi}}$ applied electrons are consumed by the oxygen atoms creating oxygen sublattice sites and aluminum vacancies, and due to the electron hole equilibration the concentration of holes increases simultaneously; therefore, in the limit of $P_{\mathrm{O}_2}^{\mathrm{hi}}$ applied, aluminum vacancies and holes are the dominant species on the $P_{\mathrm{O}_2}^{\mathrm{hi}}$ surface. Similarly, oxygen vacancies and electrons are expected to dominate on a $P_{\mathrm{O}_2}^{\mathrm{lo}}$ surface. The electric field due to the charged defect species modifies the transport to and from a particular surface in such way that local charge neutrality holds approximately between the dominant vacancy species, ν, and the charge compensating electronic species, $\overline{\nu}$, on the surface

$$|z_\nu|\mathcal{C}_\nu \simeq \mathcal{C}_{\overline{\nu}} \tag{3.22}$$

where the $\{\nu, \overline{\nu}\}$ pair denotes $\{\mathrm{V}_{\mathrm{Al}}^{3\text{-}}, \mathrm{h}\}$ at high oxygen partial pressure, and $\{\mathrm{V}_{\mathrm{O}}^{2+}, \mathrm{e}\}$ at low oxygen partial pressure. This approximation does not hold in general for intermediate pressures, or if the vacancies are much more numerous than the electronic defects in

equilibrium. Applying the law of mass action to the reaction given in 3.21 with equilibrium constant K_{Al}, together with Schottky and electron hole equilibrium at the surfaces, the concentration of the dominant vacancy species, ν, is found to adhere to the simple power law given by

$$\mathcal{C}_\nu = f_\nu \, P_{\mathrm{O}_2}^{n_\nu} \tag{3.23}$$

$$n_\nu = \frac{-z_\nu}{2|z_{\mathrm{O}}| \, (|z_\nu| + 1)} \tag{3.24}$$

$$f_\nu = \left(|z_\nu|^{-|z_\nu|} \, K_{\mathrm{S}}^{3-|z_\nu|} K_{\mathrm{eh}}^{|z_\nu|(|z_\nu|-2)} K_{\mathrm{Al}}^{-z_\nu/2} \right)^{\frac{1}{|z_\nu|+1}} \tag{3.25}$$

where z_{O} is the integer charge number of the oxygen ion, z_ν is the charge of the dominant vacancy species, and the power law exponent, n_ν, which in our case takes the values, $n_{\mathrm{V}_{\mathrm{O}}^{2+}} = -1/6$ and $n_{\mathrm{V}_{\mathrm{Al}}^{3-}} = 3/16$, and the prefactor, f_ν, are introduced. It is noteworthy that the realisation of these power laws in the experiments supports the model of vacancies carrying nominal ionic charges, not the fractional charges that are usually estimated in electronic structure calculations, which typically vary from 1.0 to 1.6 in DFT calculations for oxides [11, 32]. It is also far from obvious that simple point defect diffusion, well understood in bulk crystals, is the mechanism of diffusion in grain boundaries, in which the prefactors of diffusion coefficients are anomalously large [59, 68].

In general, the flux of aluminum ions, J_{Al} implies the take up or release of $|3J_{\mathrm{Al}}/4|$ molecules of O_2 per unit time and unit area of surface, and the opposite flux of oxygen ions leads to $|J_{\mathrm{O}}/2|$ molecules O_2 taken up or released. The ionic charges have the opposite sign and the fluxes have the opposite sign due to their different gradients, therefore the permeation rate in molecules of oxygen per unit area per second is given by

$$P = \left| \frac{3}{4} J_{\mathrm{Al}} \right| + \left| \frac{1}{2} J_{\mathrm{O}} \right| = \frac{1}{4e_0} |I_{\mathrm{ion}}|,$$

and hence by using $I_{\mathrm{ion}} = I_{\mathrm{vac}}$

$$P = \frac{1}{4e_0} |I_{\mathrm{vac}}| \tag{3.26}$$

where the current density carried by the ions, I_{ion}, and vacancies, I_{vac}, represent the same physical current density, which has to be balanced by the electron and hole currents.

To interpret and compare with the results of our fully time-dependent approach, a simple one-dimensional steady-state model is introduced, the derivation of which is

given in chapter 4 section 4.3.2. By considering only the flux of the dominant vacancy species, denoted by suffix ν, and its charge-compensating electronic species, $\overline{\nu}$:

$$I_{\text{vac}} \simeq I_{\nu}, \tag{3.27}$$

the permeation rate is approximated by

$$P = \frac{|z_{\nu}|}{4} D_{\nu}^{\text{eff}} \frac{|\mathcal{C}_{\nu}^{II} - \mathcal{C}_{\nu}^{I}|}{L}, \tag{3.28a}$$

$$D_{\nu}^{\text{eff}} = \frac{D_{\nu} D_{\overline{\nu}}}{D_{\nu}|z_{\nu}| + D_{\overline{\nu}}}(|z_{\nu}| + 1). \tag{3.28b}$$

Using equation 3.23 the permeation rate can be written as

$$P = \frac{|z_{\nu}|}{4} D_{\nu}^{\text{eff}} f_{\nu} \frac{|\left(P_{\text{O}_2}^{II}\right)^{n_{\nu}} - \left(P_{\text{O}_2}^{I}\right)^{n_{\nu}}|}{L} \tag{3.29}$$

where again $n_{\text{V}_{\text{O}}^{2+}} = 3/16$, and $n_{\text{V}_{\text{Al}}^{3-}} = -1/6$. Equation 3.29 shows that the permeation rate becomes a power law only for $\left(P_{\text{O}_2}^{II}\right)^{n_{\nu}} \gg \left(P_{\text{O}_2}^{I}\right)^{n_{\nu}}$. It is also worth noting that the permeation rate is not proportional to the oxygen pressure difference across the membrane, but rather to the difference in the vacancy concentration between the two surfaces.

The oxidation rate 'J' of aluminum in atoms per second per unit area in terms of the permeation rate of oxygen in molecules per second per unit area is given by

$$J = \frac{2}{3} P \,. \tag{3.30}$$

We can compare the above results with the Wagner theory [2, 62, 189], in which the oxidation rate is given by

$$J = \frac{1}{|z_{\text{Al}}| z_{\text{O}}^2 e_0^2} \int_I^{II} \frac{(\sigma_{\text{V}_{\text{O}}^{2+}} + \sigma_{\text{V}_{\text{Al}}^{3-}})(\sigma_h + \sigma_e)}{\sigma_{\text{V}_{\text{O}}^{2+}} + \sigma_{\text{V}_{\text{Al}}^{3-}} + \sigma_h + \sigma_e} d\mu_{\text{O}} \tag{3.31}$$

where z_{Al} is the aluminum ion charge and μ_{O} is the internal oxygen chemical potential. By assuming that the conductivity of the dominant vacancy species, $\sigma_{\nu} = D_{\nu} c_{\nu} z_{\nu}^2 e_0^2 / k_{\text{B}} T$, is much larger than that of the other vacancy species, and similarly for the dominant electronic species, $\overline{\nu}$, the oxidation rate simplifies to

$$J = \frac{1}{|z_{\text{Al}}| z_{\text{O}}^2 e_0^2} \int_I^{II} \frac{\sigma_{\nu} \sigma_{\overline{\nu}}}{\sigma_{\nu} + \sigma_{\overline{\nu}}} d\mu_{\text{O}} \,. \tag{3.32}$$

Applying the charge neutrality approximation to this equation and considering relation 3.30 the permeation rate given in equations 3.28 follows, which makes our 1D model consistent with the Wagner theory. The derivation of this form of the Wagner theory, however, requires Schottky and electron-hole equilibrium at any position in the film or scale,

$$3\mu_{\mathrm{V}_\mathrm{O}^{2+}} + 2\mu_{\mathrm{V}_\mathrm{Al}^{3-}} = 0 \quad \text{and} \quad \mu_\mathrm{e} + \mu_\mathrm{h} = 0 \tag{3.33}$$

neither of which is enforced in our treatment. Strictly speaking, the above conditions only need to be met by the spatial variations of the chemical potentials, but if equations 3.33 hold at the surfaces both formulations are equivalent and there is no arbitrary additive constant.

Equations 3.28 are equivalent to the formulas given by [84] for the permeation rate in the limit of $D_\nu \ll D_{\overline{\nu}}$. However, the details of the derivation are different such as the assumption of purely conductive transport of electrons and holes, $I_s = -\sigma_s \nabla\phi$, which is made in [84].

3.4.2 Time-dependent 3D calculations

In the calculations within the hexagonal slab model transport of vacancies is simulated for the 3D grain structure and grain boundaries with finite width δ. The time-dependent calculations prove to have a similar steady-state limit to the 1D model described above, in which the fluxes and current densities are constant as a function of the position in the grain boundary. The vacancy flux is calculated directly from the concentration and electrostatic potential gradients, and the permeation rate follows from equation 3.26. Before the steady-state is achieved, an average permeation rate can be calculated by numerical integration of the vacancy flux through the grain boundary, which converges faster to the steady-state permeation rate than the permeation rate calculated from the vacancy fluxes on individual mesh nodes.

3.4.2.1 Reaction equations

Exchange of oxygen between the gas phase and the oxide surface includes multiple steps, namely adsorption, dissociation, surface diffusion, charge transfer, and incorporation into the oxide surface, each of which might be the rate limiting step. In the simulations the assumptions of instantaneous equilibration between the vacancy species inducing the Schottky equilibrium, and the instantaneous equilibration between electrons and holes are relaxed, and the respective processes are formulated with rate dependent

reaction equations. In addition to the oxygen incorporation mechanism given in 3.21, oxygen absorption (desorption) by annihilation (creation) of an oxygen vacancy is considered

$$\frac{1}{2}\mathrm{O}_2(g) + \mathrm{V}_{\mathrm{O}}^{2+} \underset{k_{\mathrm{O},b}}{\overset{k_{\mathrm{O},f}}{\rightleftharpoons}} \mathrm{O}_{\mathrm{O}}^{\times} + 2\mathrm{h}. \tag{3.34}$$

The Schottky reaction is included at the alumina – oxygen gas surfaces

$$\mathrm{Nil} \underset{k_{\mathrm{S},b}}{\overset{k_{\mathrm{S},f}}{\rightleftharpoons}} \frac{2}{3}\,\mathrm{V}_{\mathrm{Al}}^{3\text{-}} + \mathrm{V}_{\mathrm{O}}^{2+}\,. \tag{3.35}$$

Electron and hole recombination and generation,

$$\mathrm{Nil} \underset{k_{\mathrm{eh},b}}{\overset{k_{\mathrm{eh},f}}{\rightleftharpoons}} \mathrm{e} + \mathrm{h}, \tag{3.36}$$

is considered at the grain boundary and on the surfaces.

In this application the surface reactions, $\mathcal{R}_s$, depend on the time-dependent surface concentrations, $\mathcal{C}_s^{I/II}(t)$, and the oxygen partial pressures, $P_{\mathrm{O}_2}^{I}$ or $P_{\mathrm{O}_2}^{II}$, on the respective surfaces, (I) or (II), and the reaction rate constants, $k_{i,f}$ and $k_{i,b}$

$$\begin{aligned}
&\mathcal{R}_s^{\mathrm{j}}\left(\{\mathcal{C}_s^{\mathrm{j}}(t)\}; P_{\mathrm{O}_2}^{\mathrm{j}}, \{k_{i,f}\}, \{k_{i,b}\}\right) \qquad (3.37)\\
&s \in \{\mathrm{V}_{\mathrm{O}}^{2+}, \mathrm{V}_{\mathrm{Al}}^{3\text{-}}, \mathrm{e}, \mathrm{h}\} \text{ species}\\
&i \in \{\mathrm{O}, \mathrm{Al}, \mathrm{S}, \mathrm{eh}\} \quad \text{see reactions 3.34, 3.21, 3.35, and 3.36}\\
&\mathrm{j} \in \{I, II\} \text{ surface index}
\end{aligned}$$

The law of mass action is used to derive expressions for the reactions $\mathcal{R}_s$, and R_s. The coupled system of reactions, $\mathcal{R}_s$, at the alumina - oxygen gas surfaces, is used for the boundary conditions of the transport equations. The equations are provided in what follows and they describe reactions that may proceed in either direction, depending on the species concentrations and the oxygen gas pressure applied.

Applying the law of mass action to the reactions, 3.34, 3.21, 3.35, and 3.36 yields

$$\mathcal{R}_{\mathrm{O}} = k_{\mathrm{O},b}\left(K_{\mathrm{O}}\, P_{\mathrm{O}_2}^{1/2}\, \mathcal{C}_{\mathrm{V}_{\mathrm{O}}^{2+}} - \mathcal{C}_{\mathrm{h}}^{2}\right) \tag{3.38}$$

$$\mathcal{R}_{\mathrm{Al}} = k_{\mathrm{Al},b}\left(K_{\mathrm{Al}}\, P_{\mathrm{O}_2}^{1/2}\, \mathcal{C}_{\mathrm{e}}^{2} - \mathcal{C}_{\mathrm{V}_{\mathrm{Al}}^{3\text{-}}}^{2/3}\right) \tag{3.39}$$

$$\mathcal{R}_{\mathrm{S}} = -k_{\mathrm{S},b}\left(\mathcal{C}_{\mathrm{V}_{\mathrm{Al}}^{3\text{-}}}^{2/3}\, \mathcal{C}_{\mathrm{V}_{\mathrm{O}}^{2+}} - K_{\mathrm{S}}\right) \tag{3.40}$$

$$\mathcal{R}_{\mathrm{eh}} = -k_{\mathrm{eh},b}(\mathcal{C}_{\mathrm{e}}\, \mathcal{C}_{\mathrm{h}} - K_{\mathrm{eh}}) \tag{3.41}$$

and the coupled system of reactions at the alumina – oxygen gas surfaces can be written as

$$\mathcal{R}_{\mathrm{V}_{\mathrm{O}}^{2+}} = -\mathcal{R}_{\mathrm{O}} + \mathcal{R}_{\mathrm{S}} \qquad \mathcal{R}_{\mathrm{V}_{\mathrm{Al}}^{3-}} = \mathcal{R}_{\mathrm{Al}} + \frac{2}{3}\mathcal{R}_{\mathrm{S}} \tag{3.42a}$$

$$\mathcal{R}_{\mathrm{h}} = 2\,\mathcal{R}_{\mathrm{O}} + \mathcal{R}_{\mathrm{eh}} \qquad \mathcal{R}_{\mathrm{e}} = -3\,\mathcal{R}_{\mathrm{Al}} + \mathcal{R}_{\mathrm{eh}} \tag{3.42b}$$

3.4.3 Simulation results

Results are presented here to address some of the questions posed in section 2.7.1 of the introduction, regarding the membrane experiments [84] and their interpretation with 1D diffusion models based on the Wagner theory. Time dependent calculations are performed and characteristic aspects of the dynamics are highlighted and explained. A permeation calculation reproduces the power laws found in [84].

3.4.3.1 Initial conditions and choice of parameters

The system at $t = t_0$ is assumed to be of strictly stoichiometric composition, $2c_{\mathrm{V}_{\mathrm{O}}^{2+}}(t_0) = 3c_{\mathrm{V}_{\mathrm{Al}}^{3-}}(t_0)$, and the set of initial values of the concentrations, $\{c_s(t_0)\}$, and $\{\mathcal{C}_s(t_0)\}$, is assumed to be in equilibrium with oxygen partial pressure $P_{\mathrm{O}_2}^{\mathrm{eq}}$, which is defined as the reference pressure so that only ratios $P_{\mathrm{O}_2}/P_{\mathrm{O}_2}^{\mathrm{eq}}$ enter the equations. The initial concentrations in the surface layer and in the grain boundary are chosen to be equal, $c_s = \mathcal{C}_s$, and independent of the position in the grain boundary and on the surface. This choice also constrains the electron and hole concentrations, $c_{\mathrm{e}}(t_0) = c_{\mathrm{h}}(t_0)$, in order for overall charge neutrality to be maintained. The initial values for the concentrations, $c_s(t_0)$, are used to specify the equilibrium constants, K_i, of the reactions, which are also related to the reactions rates

$$K_i = \exp\left(\frac{\sum_s w_{i,s}\mu_s^0}{k_{\mathrm{B}}T}\right) = \prod_s c_s^{w_{i,s}}(t_0) = \frac{k_{i,f}}{k_{i,b}} \tag{3.43}$$

where $\mu_s^0 = -k_{\mathrm{B}}T\ln(c_s(t_0))$ is the reference chemical potential with $c_s(t_0)$ in units of c_{ref}, and $w_{i,s}$ is the stoichiometric coefficient of species s in the i-th reaction.

This choice of initial parameters only leaves undetermined the ratio of point defect to electronic defect initial concentrations, which is a function of the difference

between the vacancy formation (segregation) energy and the Fermi level. For bulk α-alumina the ionic and electronic disorder has been analyzed from experimental thermodynamic data [123] and more recently from first principles calculations [138]. At temperature $1900\,\mathrm{K}$ electronic disorder is found dominant for the bulk material. However, in the absence of data for the surface and interface equilibrium defect concentrations the aim is to justify the choice by comparison to the experimental permeation data, see section 3.4.3.6. We expect the point defects which are favourably formed at the surfaces and interfaces to introduce states in the band gap, and therefore assume much higher vacancy, electron, and hole concentrations at the surfaces, and interfaces than in the bulk material. The reference concentration for the simulations is chosen as $c_{\mathrm{ref}} = 10^{18}\,\mathrm{cm}^{-3}$, which would correspond to about 4×10^{-5} defects per formula unit of bulk Al_2O_3, and will only be reached in the high or low pressure limits. The concentrations are initialized at $t = t_0$ with $c_{\mathrm{h}} = 0.1\,c_{\mathrm{ref}}$, and $c_{\mathrm{V}_{\mathrm{O}}^{2+}} = 5 \times 10^{-3}\,c_{\mathrm{ref}}$.

For $T = 1900\,\mathrm{K}$ and with $\varepsilon_r^{\mathrm{Al_2O_3}} = 9.8$, the reference screening length, see equation 3.12, becomes, $\ell_{\mathrm{D}} = 9.4\,\mathrm{nm}$. The thickness of the slab is set to, $L = 1\,\mu\mathrm{m}$, the side length of the hexagon to $a_{\mathrm{hex}} = 1\,\mu\mathrm{m}$, the grain boundary and surface layer thickness to $\delta = 1\,\mathrm{nm}$. The diffusion coefficients of the species are chosen as: $D_{\mathrm{h}} = D_{\mathrm{e}} = 1\,D_{\mathrm{ref}}$, and $D_{\mathrm{V}_{\mathrm{O}}^{2+}} = D_{\mathrm{V}_{\mathrm{Al}}^{3-}} = 0.01\,D_{\mathrm{ref}}$ where D_{ref} is unknown and used to define the time scale of the simulations. One reaction rate constant in each reaction has to be estimated and they are set to: $k_{\mathrm{O},b} = 10^3$, $k_{\mathrm{Al},b} = 10^2$, and $k_{\mathrm{eh},b} = k_{\mathrm{S},b} = 10^3$.

In sections 3.4.3.2, 3.4.3.3 and 3.4.3.5 calculations are discussed for which the oxygen partial pressure is raised at surface (II), the pressure at surface (I) is kept constant at $P_{\mathrm{O}_2}^{I} = P_{\mathrm{O}_2}^{\mathrm{eq}}$, and the pressure ratio is given by $P_{\mathrm{O}_2}^{II}/P_{\mathrm{O}_2}^{I} = 10^5$. Snapshots of the evolution at two times, t_n, and t_N, with $t_n \ll t_N$, are shown. The time t_n is chosen to capture characteristic behaviour in the initial transient, and t_N is the time at which steady-state conditions are achieved.

3.4.3.2 Evolution of the concentrations

Figure 3.6 shows snapshots of the concentrations; the coordinate system is defined in figure 3.2. The pressure $P_{\mathrm{O}_2}^{II} = P_{\mathrm{O}_2}^{\mathrm{hi}}$ and the $\mathrm{V}_{\mathrm{Al}}^{3-}$ and the h concentrations are the dominant species. Local charge neutrality holds approximately for the dominant species, $3c_{\mathrm{V}_{\mathrm{Al}}^{3-}} \approx c_{\mathrm{h}}$, throughout most of the grain boundary and at surface (II) in the steady-state t_N limit but is clearly violated at surface (I).

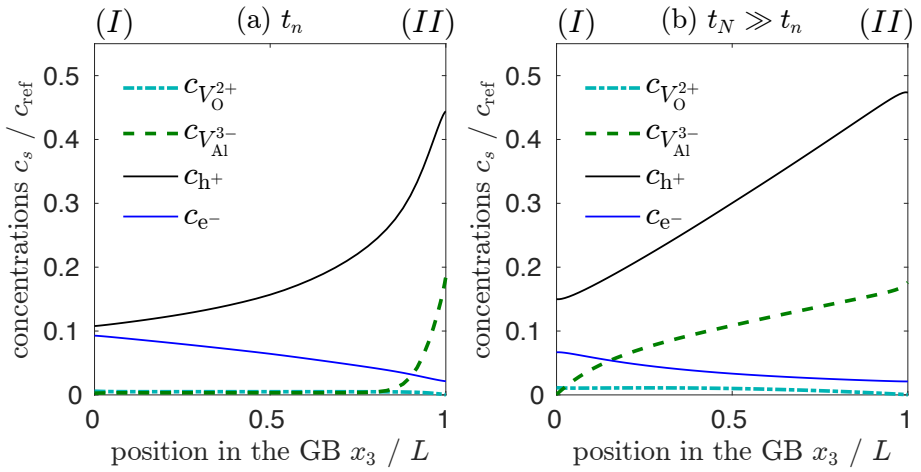

FIGURE 3.6: Snapshots of the concentrations of vacancies, electrons, and holes as a function of x_3 in the grain boundary plane, with fixed $x_1 = a_{\text{hex}}/4$, for two different times and with $P^{II}_{O_2}/P^{I}_{O_2} = 10^5$. Scaled units with $c_{\text{ref}} = 10^{18}\,\text{cm}^{-3}$ and $L = 1\,\mu\text{m}$.

3.4.3.3 Evolution of the charge density and the electrostatic potential

Figure 3.7 shows the charge density, ρ, and the electrostatic potential, ϕ, corresponding to the concentrations shown in figure 3.6. Charge is accumulated near the high pressure surface (II) initially until time t_n, see figures 3.7 (a) and 3.8; this change in the local charge density is due to the different magnitudes of the diffusion coefficients of the mobile species and the requirement of charge conservation within the irreducible zone of the structure. If all species had the same diffusion coefficient the charge density would be identically zero, $\rho(t) \equiv 0$, for all times in calculations with the present model. The negatively charged surface (II) generates a monotonically decreasing potential with increasing x_3; however, at t_n it is screened to an almost constant value by the charge density that has accumulated near surface (II). At time t_N, see figure 3.7 (b), some of the charge in the grain boundary has propagated to the surface (I) and the grain boundary has become weakly negatively charged, see also figure 3.8. However, the electrostatic potential has become almost linear as a function of x_3, and is dominated by the surface charges; the remaining departure from linearity is due to the charge density within the grain boundary.

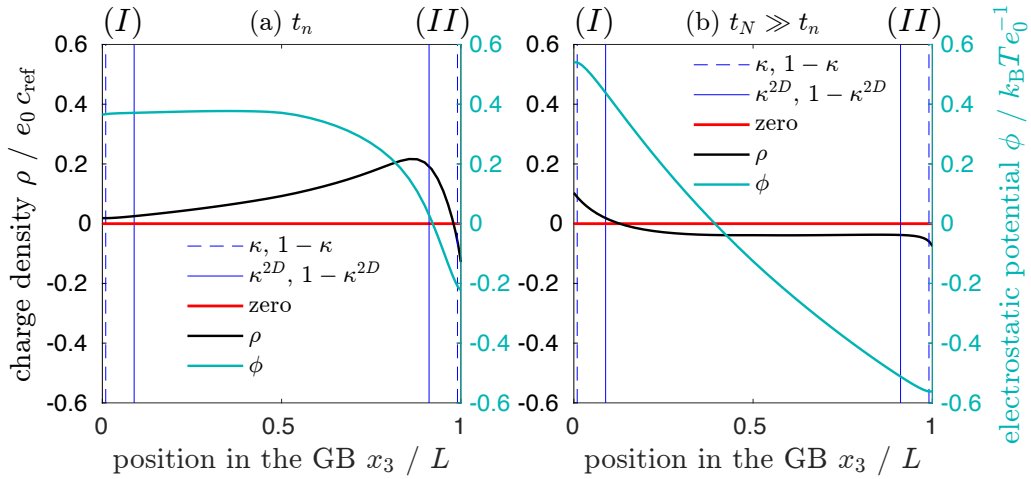

FIGURE 3.7: Snapshots of the charge density and the electrostatic potential as a function of x_3 at fixed $x_1 = a_{\text{hex}}/4$ for two different times. Two screening lengths κ, and κ^{2D} are indicated and described in the text. Scaled units with $e_0\, c_{\text{ref}} = 0.16\,\text{C}\,\text{cm}^{-3}$, $k_{\text{B}}T/e_0 = 0.16\,\text{V}$, and $L = 1\,\mu\text{m}$. The stages (a), and (b) of the overall dynamics are discussed in the text.

3.4.3.4 Screening effects

The quantity κ denotes the scaled reference screening length ℓ_{D}/L, defined in equation 3.12, and characterizes the decay in the local charge density from the surface into the grain boundary. κ^{2D} is the equivalent of the scaled reference screening length for two dimensional systems and is defined here as

$$\kappa^{2D} = \ell_{\text{D}}^{2D}/L, \quad \text{where} \quad \ell_{\text{D}}^{2D} = \frac{\varepsilon_0 \varepsilon_r k_{\text{B}} T}{e_0^2 c_{\text{ref}} \delta}. \tag{3.44}$$

The simulations, see figure 3.7, show that ℓ_{D}^{2D} is a better estimate for the spatial extent of the variations in the charge density within the grain boundary than ℓ_{D}. It should be pointed out here that simulations in which the grain boundaries and surfaces are idealized as planes without finite thickness δ would yield the same results, and $c_{\text{ref}}\delta$ in equation 3.44 would be replaced by a reference concentration per unit area. The only requirement for this to hold is that the total numbers of each species present in the irreducible zone initially, are chosen equal for the simulations with and without finite thickness δ.

3.4.3.5 Surface and grain boundary charges

The simulations are initialized with zero total charge and charge conservation requires the total charge in the irreducible zone of the structure, q_{tot}, to remain equal to zero.

This is satisfied for the calculations performed, see figure 3.8, which provides a useful check on the numerical accuracy and stability of the solution.

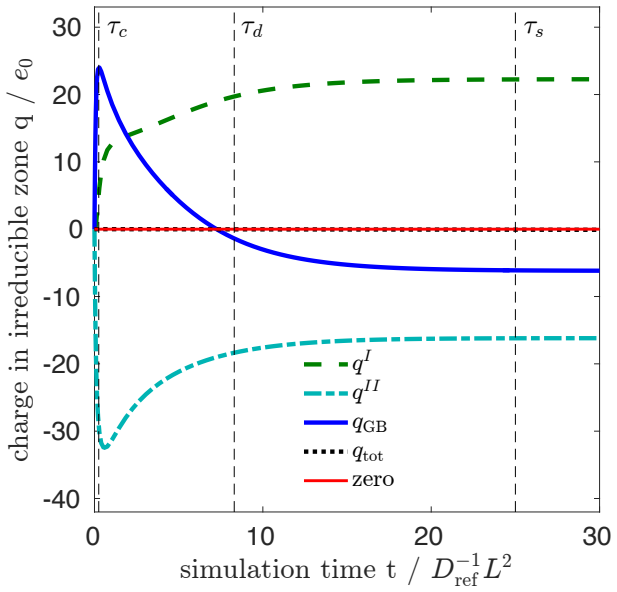

FIGURE 3.8: The charge (integrated charge density) in the irreducible zone as a function of time. q^I and q^{II} are the charges in the surface triangles of surfaces (I) and (II), respectively, q_{GB} is the charge in the grain boundary, $q_{\mathrm{tot}} = q^I + q^{II} + q_{\mathrm{GB}}$ is the total charge in the irreducible zone. The characteristic time scales τ_{c}, τ_{d}, and τ_{s} are indicated, and further discussed in the text. Scaled units are used with the thickness of the slab, $L = 1\ \mu$m, and e_0 the positive elementary charge.

The charge integrated over the grain boundary volume changes with time, $q_{\mathrm{GB}}(t)$, and the boundary carries an excess of electrons in the steady-state limit. This demonstrates that local charge neutrality, which is an assumption of the simple 1D models, is not consistent with this 3D model. Two characteristic time scales for the charging and discharging of the grain boundary are found. The time constants can be estimated by analogy to 'RC'-circuits, with time constant $\tau = RC$, where R is the resistance, and C is the capacitance. The initial charge build-up within the grain boundary is due to the diffusion of the faster of the dominant species, for $P_{\mathrm{O}_2}^{II} = P_{\mathrm{O}_2}^{\mathrm{hi}}$ the positively charged holes, $\overline{\nu} = \mathrm{h}$, and the time constant is estimated as follows from appropriate values of R and C:

$$R_{\overline{\nu}} = \frac{1}{\langle \sigma_{\overline{\nu}} \rangle} \frac{4L}{a_{\mathrm{hex}}\delta}, \tag{3.45}$$

$$C_{\mathrm{hex}} = \varepsilon_0 \varepsilon_r \frac{a_{\mathrm{hex}}^2 \sqrt{3}}{8L}, \tag{3.46}$$

$$\tau_{\mathrm{c}} \sim \frac{\varepsilon_0 \varepsilon_r}{\langle \sigma_{\overline{\nu}} \rangle} \frac{a_{\mathrm{hex}}\sqrt{3}}{2\delta}. \tag{3.47}$$

The time constant characterizing the discharging of the grain boundary is estimated from the diffusion of the slower of the dominant species, for $P^{II}_{\mathrm{O}_2} = P^{\mathrm{hi}}_{\mathrm{O}_2}$ the aluminum vacancies, $\nu = \mathrm{V}^{3\text{-}}_{\mathrm{Al}}$:

$$R_\nu = \frac{1}{\langle \sigma_\nu \rangle} \frac{4L}{a_{\mathrm{hex}}\delta}, \tag{3.48}$$

$$\tau_{\mathrm{d}} \sim \frac{\varepsilon_0 \varepsilon_r}{\langle \sigma_\nu \rangle} \frac{a_{\mathrm{hex}}\sqrt{3}}{2\delta}. \tag{3.49}$$

Where the angle brackets denote the spatial average and the physically meaningful conductivity is the product $\sigma\delta$. A third time scale characterizes the time elapsed until reaching the steady-state, and is estimated here from the diffusion length using the effective diffusion coefficient defined in equation 3.28b.

For the parameters used here, $D_\nu = D_{\overline{\nu}}/100$ and in the limit of $D_\nu \ll D_{\overline{\nu}}$,

$$\tau_{\mathrm{s}} \sim \frac{L^2}{D^{\mathrm{eff}}_\nu} \simeq \frac{L^2}{(|z_\nu|+1)D_\nu}. \tag{3.50}$$

The three time scales are indicated in figure 3.8.

3.4.3.6 Membrane permeation calculations

The permeation rate normalized by the thickness of the slab, PL, can be calculated from the current densities of the mobile defect species. Figure 3.9 shows the permeation rate in the steady-state limit as a function of the oxygen pressure ratio $P^{II}_{\mathrm{O}_2}/P^{I}_{\mathrm{O}_2}$ for a range of $P^{II}_{\mathrm{O}_2}$ values, while $P^{I}_{\mathrm{O}_2}$ is held fixed. The individual contributions of the $\mathrm{V}^{3\text{-}}_{\mathrm{Al}}$ and $\mathrm{V}^{2+}_{\mathrm{O}}$ are indicated by $PL_{\mathrm{V}^{3\text{-}}_{\mathrm{Al}}}$ and $PL_{\mathrm{V}^{2+}_{\mathrm{O}}}$, respectively. The parameters are the same as those in the previous section.

The permeation rate is also normalized by the grain boundary density, S_{GB}, to compare with the experimental permeation rate e.g. [83]. For the periodic hexagonal cell structure S_{GB} is calculated from the ratio between half the grain boundary side length of the irreducible zone, $a_{\mathrm{hex}}/4$, and the area of the irreducible zone surface triangle, $a^2_{\mathrm{hex}}\sqrt{3}/8$, hence $S_{\mathrm{GB}} = 2/\sqrt{3}a_{\mathrm{hex}}$.

Comparing the simulated permeation rate with the experimental values [84, 188] for $T = 1900\,\mathrm{K}$ and $P^{II}_{\mathrm{O}_2}/P^{I}_{\mathrm{O}_2} = 10^5\,\mathrm{Pa}/1\,\mathrm{Pa}$ the reference diffusion coefficient is calculated, $\delta D_{\mathrm{ref}} = 3.4 \times 10^{-13}\,\mathrm{m^3\,s^{-1}}$.

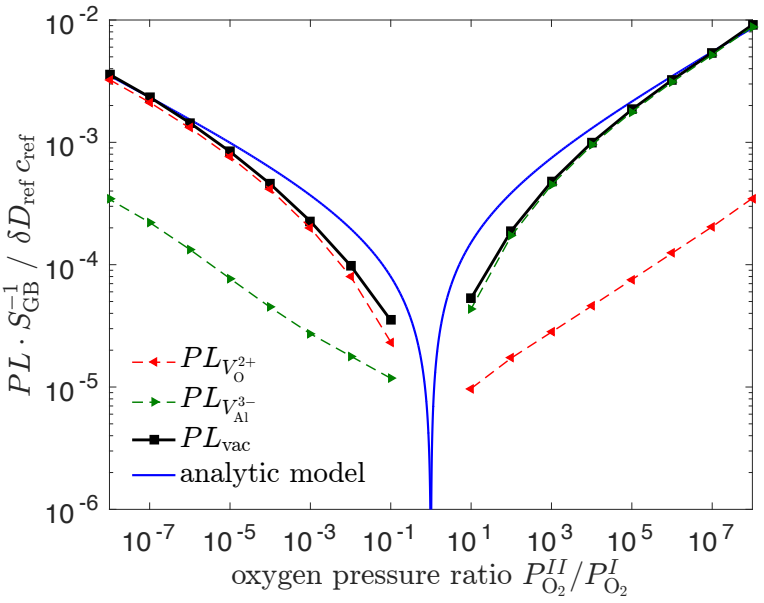

FIGURE 3.9: Oxygen permeation rate in the steady-state limit as a function of the ratio of applied oxygen gas pressures. The simulated permeation rate tends to the same power law exponents as those determined in the 1D analytic model (blue line), $n_{V_{Al}^{3-}} = 3/16$ and $n_{V_O^{2+}} = -1/6$, see section 3.4.1, and the experimentally found ones [84]. δ is the grain boundary width, $D_{ref}\,[m^2\,s^{-1}]$, $c_{ref} = 1.66\,mol\,m^{-3}$, and S_{GB} is the grain boundary density of the hexagonal cell structure.

At $P_{O_2}^{II}/P_{O_2}^{I} = 10^5$ the average aluminum vacancy concentration in the grain boundary is found to be $\langle c_{V_{Al}^{3-}} \rangle = 10^{17}\,cm^{-3}$, and with the concentration of alumina formula units, $c_{Al_2O_3} = 2.26 \times 10^{22}\,cm^{-3}$, the aluminum diffusion coefficient is estimated to be $\delta D_{Al} = \delta D_{V_{Al}^{3-}} \langle c_{V_{Al}^{3-}} \rangle / 2c_{Al_2O_3} = 7.6 \times 10^{-21}\,m^3\,s^{-1}$, which is close to the value reported in [84], $\delta D_{Al} = 4.5 \times 10^{-21}\,m^3\,s^{-1}$.

The agreement indicates that the reference concentration is a reasonable choice provided the assumptions of $c_\nu(P_{O_2}^{eq}) \ll c_{\bar{\nu}}(P_{O_2}^{eq})$ and $D_\nu \ll D_{\bar{\nu}}$ are applicable. Indeed, if electrons and holes would diffuse slower than the vacancies, $D_\nu \gg D_{\bar{\nu}}$, the permeation rate would be limited by the electronic defects and the diffusion coefficients determined from the permeation experiments [84] would reflect the electronic diffusion coefficient rather than the ionic one.

The simulated permeation rate, shown in figure 3.9 as a function of the oxygen partial pressure ratio $P_{O_2}^{II}/P_{O_2}^{I}$, demonstrates a transition between p-type and n-type ionic conductivity as the dominant transport mechanism. In growing alumina scales a $p-n$ transition has been hypothesized to occur within the grain boundaries of the scales [70], this transition is discussed further in section 3.5.6.4, where simulations with an extended model that includes an internal Schottky reaction and coupled stress generation mechanism are discussed.

The variation of the logarithm of the permeation rate P, see equation 3.29, with the oxygen chemical potential at surface (II) in the limits of high and low applied oxygen partial pressure, $P^{II}_{O_2}$, yield the power law exponent corresponding to the dominant defect species, ν,

$$\frac{\partial \ln P}{\partial \ln P^{II}_{O_2}} = n_\nu \tag{3.51}$$

in the limit of high and low $P^{II}_{O_2}$.

An asymptotic electronic current density, I_{el}, and vacancy current density, I_{vac} can be calculated similarly to the permeation rate. The current density of vacancies, $I_{vac} = I_{V^{2+}_O} + I_{V^{3-}_{Al}}$, is equal and opposite to the electronic current, $I_{el} = I_e + I_h$, at all pressure ratios in the long time limit, see figure 3.10, this means the net current, $I_{net} = I_{vac} + I_{el}$ is zero.

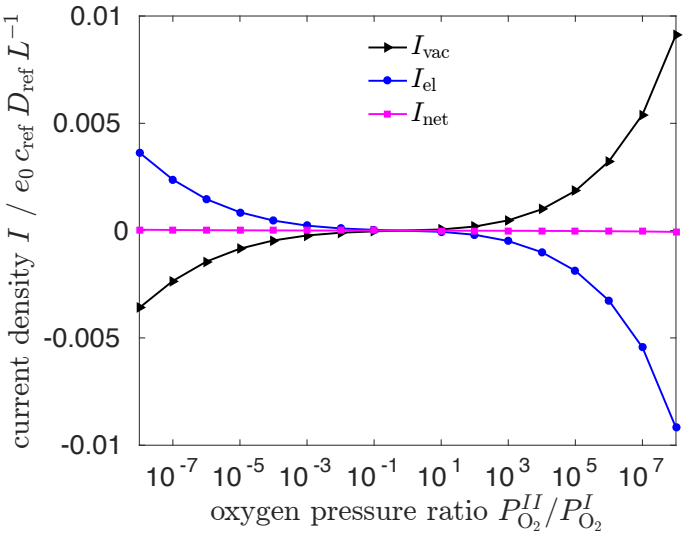

FIGURE 3.10: Current densities per grain boundary 'cross-section area' $\mathbb{A}_{GB}$, see figure 3.3, in the steady-state limit as a function of the ratio of applied oxygen gas pressures. Scaled units with $e_0\, c_{ref} = 0.16\,\mathrm{C\,cm^{-3}}$, and $L = 1\,\mu$m.

The plot for the average conductivities, see figure 3.11, is equivalent to a Kröger-Vink (Brouwer) diagram [165] for the mobile species present, except that the average concentrations are scaled by the corresponding diffusion coefficients. The averaged conductivities of the dominant point defect species, ν, adhere to

$$\frac{\partial \ln\langle\sigma_\nu\rangle}{\partial \ln P^{II}_{O_2}} = n_\nu. \tag{3.52}$$

The crossover in the dominant point defect species in the permeation rate and the average conductivity is observed at the same value of $P_{\mathrm{O}_2}^{II}$.

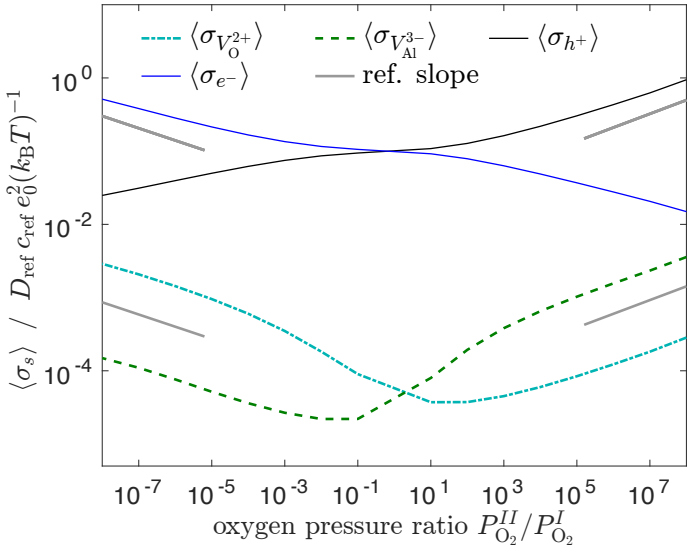

FIGURE 3.11: Conductivities averaged over the grain boundary layer, $\langle\sigma_s\rangle$. The reference lines are given by const. $\times\, P_{\mathrm{O}_2}^{n_\nu}$. Scaled units with $e_0^2\, c_{\mathrm{ref}}/k_{\mathrm{B}}T \approx 1\,\mathrm{C}^2\,\mathrm{cm}^{-3}\,\mathrm{J}^{-1}$.

3.4.3.7 The open circuit voltage

From the electrical potential difference across the film, $\Delta\phi$, and the chemical potential differences the voltage across the film, V_{e}, as measureable by a voltmeter, can be predicted. Analytically, the electrical potential difference within the zero net current approximation in steady-state can be calculated from

$$e_0\Delta\phi = -\int_0^L \sum_s t_s \frac{\nabla\mu_s}{z_s} dx \tag{3.53}$$

which follows from the zero net current approximation. In the limit of small ℓ_{D}/L the local charge neutrality approximation is applicable, as discussed further in chapter 4, and for the two species $(\nu, \overline{\nu})$,

$$|z_\nu| c_\nu + c_{\overline{\nu}} = 0 \tag{3.54}$$

$$d\mu_\nu = d\mu_{\overline{\nu}} \tag{3.55}$$

the variations in the chemical potentials are connected due to local charge neutrality. In the $\rho = 0$ limit the sum of the weighted transport numbers can be simplified

$$\frac{t_\nu}{z_\nu} + \frac{t_{\overline{\nu}}}{z_{\overline{\nu}}} = z_{\overline{\nu}} \frac{D_{\overline{\nu}} - D_\nu}{D_\nu |z_\nu| + D_{\overline{\nu}}} \equiv D' \tag{3.56}$$

where the dimensionless constant D' is introduced. The electrostatic potential difference for this special case hence reads as

$$e_0 \Delta\phi = -D' \, \Delta\mu_\nu = -D' \, \Delta\mu_{\overline{\nu}}. \tag{3.57}$$

If electrons and holes are in equilibrium at the film surfaces, and by using $\Delta\mu_{\overline{\nu}} = -z_{\overline{\nu}} \Delta\mu_\mathrm{e}$, the potential difference can be further written as

$$e_0 \Delta\phi = z_{\overline{\nu}} D' \, \Delta\mu_\mathrm{e} = \frac{D_{\overline{\nu}} - D_\nu}{D_\nu |z_\nu| + D_{\overline{\nu}}} \, \Delta\mu_\mathrm{e}. \tag{3.58}$$

Given the above formula for the electrostatic potential difference the electron electrochemical potential difference can be expressed as

$$\Delta\eta_\mathrm{e} = \Delta\mu_\mathrm{e} - e_0 \Delta\phi = (1 - z_{\overline{\nu}} D') \, \Delta\mu_\mathrm{e} \tag{3.59}$$

$$= \frac{D_\nu}{D_\nu |z_\nu| + D_{\overline{\nu}}} (|z_\nu| + 1) \Delta\mu_\mathrm{e}. \tag{3.60}$$

The open circuit voltage accross the membrane is given by

$$V_\mathrm{e} = -\frac{\Delta\eta_\mathrm{e}}{e_0} \quad \text{where} \quad \Delta\eta_\mathrm{e} = \eta_\mathrm{e}^{II} - \eta_\mathrm{e}^{I}. \tag{3.61}$$

If measured experimentally it could provide valuable additional information about the transport properties of the membrane. In the simulations the voltage is readily calculated in the ideal solution approximation by using the electron surface concentrations and the electrostatic potential difference, hence

$$V_\mathrm{e} = -\frac{k_\mathrm{B} T}{e_0} \ln\left(\frac{c_\mathrm{e}^{II}}{c_\mathrm{e}^{I}}\right) + \phi^{II} - \phi^{I}. \tag{3.62}$$

In figure 3.12 the electrostatic potential difference between the surfaces and the open circuit voltage, both calculated for the simulations with different applied $\Delta\mu_\mathrm{O}$ and in the steady-state limit are compared to a 1D analytic model. The model for the electrostatic

potential difference is given by

$$\Delta\phi = \phi^{II} - \phi^{I} = -z_{\overline{\nu}} \frac{D_{\overline{\nu}} - D_{\nu}}{D_{\nu}|z_{\nu}| + D_{\overline{\nu}}} \frac{k_{\mathrm{B}}T}{e_0} \ln\left(\frac{c_{\overline{\nu}}^{II}}{c_{\overline{\nu}}^{I}}\right) \tag{3.63}$$

and the model for the volatage is therefore given by

$$V_{\mathrm{e}} = \frac{D_{\nu}}{D_{\nu}|z_{\nu}| + D_{\overline{\nu}}} (|z_{\nu}| + 1) \ln\left(\frac{c_{\overline{\nu}}^{II}}{c_{\overline{\nu}}^{I}}\right). \tag{3.64}$$

The equations are derived in detail in chapter 4 sections 4.3.2.2 and 3.4.3.7.

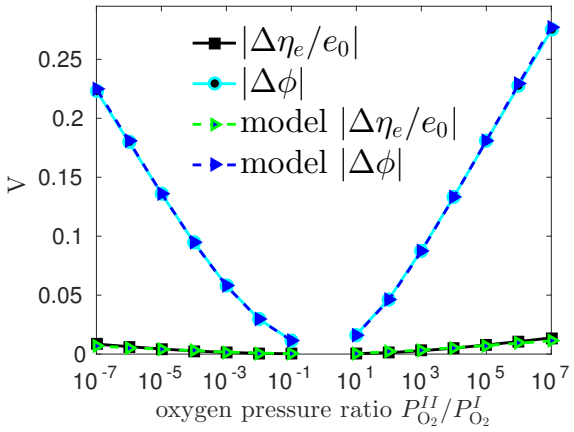

FIGURE 3.12: The electrostatic potential difference $\Delta\phi = \phi^{II} - \phi^{I}$ and the open circuit voltage $V_{\mathrm{e}} = -\Delta\eta_{\mathrm{e}}/e_0$ as a function of the applied oxygen partial pressure ratio at the membrane surfaces. The potential and voltage are in good agreement with an analytical model further described in the text.

For the graph of the models in figure 3.12 the concentrations of the dominant electronic defect, $c_{\overline{\nu}}$, as determined from the simulations have been used in equations 3.63 and 3.64. This way the validity of the factor containing the diffusion coefficients is assessed, which seems to be justified since the model matches the simulation results.
In the permeation experiments the concentration of electrons on the surfaces follows the simple power law behaviour

$$c_{\mathrm{e}} \sim P_{\mathrm{O_2}}^{-|n_{\nu}|} \quad \text{and} \quad n_{\nu} = -\frac{z_{\nu}}{4(|z_{\nu}| + 1)} \tag{3.65}$$

in the limit of very large, $P_{\mathrm{O_2}}^{\mathrm{hi}}$, or low, $P_{\mathrm{O_2}}^{\mathrm{lo}}$, partial pressure applied. In the limit the electron electrochemical potential difference, or difference in the Fermi level can therefore

be written as

$$\Delta\eta_{\mathrm{e}} = -\frac{D_\nu|z_\nu|}{D_\nu|z_\nu| + D_{\overline{\nu}}}\,\frac{k_{\mathrm{B}}T}{4}\ln\left(\frac{P_{\mathrm{O}_2}^{II}}{P_{\mathrm{O}_2}^{I}}\right). \tag{3.66}$$

the voltage is given by

$$V_{\mathrm{e}} = \frac{D_\nu|z_\nu|}{D_\nu|z_\nu| + D_{\overline{\nu}}}\,\frac{k_{\mathrm{B}}T}{4e_0}\ln\left(\frac{P_{\mathrm{O}_2}^{II}}{P_{\mathrm{O}_2}^{I}}\right) \tag{3.67}$$

and is always positive for $P_{\mathrm{O}_2}^{II} > P_{\mathrm{O}_2}^{I}$.

The scaled variation of the voltage with the applied pressure, V_{e}', could be used to determine the ratio of the vacancy and electron or hole diffusion coefficients

$$V_{\mathrm{e}}' = \frac{4e_0}{k_{\mathrm{B}}T}\,\frac{\partial\, V_{\mathrm{e}}}{\partial\, \log P_{\mathrm{O}_2}^{II}} = t_{\mathrm{e}} \simeq \frac{D_\nu|z_\nu|}{D_\nu|z_\nu| + D_{\overline{\nu}}} \tag{3.68}$$

where the constant $k_{\mathrm{B}}T/4e_0$ that gauges the required sensitivity in the measurement is $k_{\mathrm{B}}T/4e_0 = 40\,\mathrm{mV}$ at $1900\,\mathrm{K}$.

Importantly, if the variation determined from the permeation experiments with a voltage measurement $V_{\mathrm{e}}' \ll 1$ the electronic species diffuse much faster, and for $V_{\mathrm{e}}' \approx 1$ the vacancy species diffuse much faster. This measurement would therefore be of great use for determining the effect of the electric field on the vacancy diffusion, which depends on the difference of the vacancy and compensating electronic species diffusion coefficients.

For growing alumina scales voltages greater than $1\,\mathrm{V}$ have been measured [71, 160], indicating a significant ionic transport number.

3.4.3.8 The Schottky equilibrium

As discussed in section 3.4.1, Schottky equilibrium and electron-hole equilibrium are required conditions for the validity of the Wagner model and equation 3.31. In this section it is examined to what extent these equilibria are attained in our grain boundary calculations as the steady-state limit is approached.

Figure 3.13 shows an example of the voltages, $\eta_s/z_s e_0$, in the long time limit, the internal chemical potentials are shown in figure 3.14. The calculations are performed for $P_{\mathrm{O}_2}^{I} = P_{\mathrm{O}_2}^{\mathrm{lo}}$, and $P_{\mathrm{O}_2}^{II} = P_{\mathrm{O}_2}^{\mathrm{hi}}$. In these calculations Schottky equilibrium does not hold, see figures 3.13, and 3.14, except at the surfaces where the Schottky reaction is included in the equations. The reaction rates at the surfaces are higher than the transport between the surfaces and the grain boundaries, therefore Schottky equilibrium is

attained at the surfaces. The defect chemical potentials are calculated from the ideal dilute solution approximation, $\mu_s = k_\mathrm{B}T\ln(c_s/c_s(t_0))$, where $c_s(t_0)$ are the equilibrium concentrations. The spatial variation of the electrochemical, and chemical potentials would be significantly different if internal Schottky equilibrium was imposed.

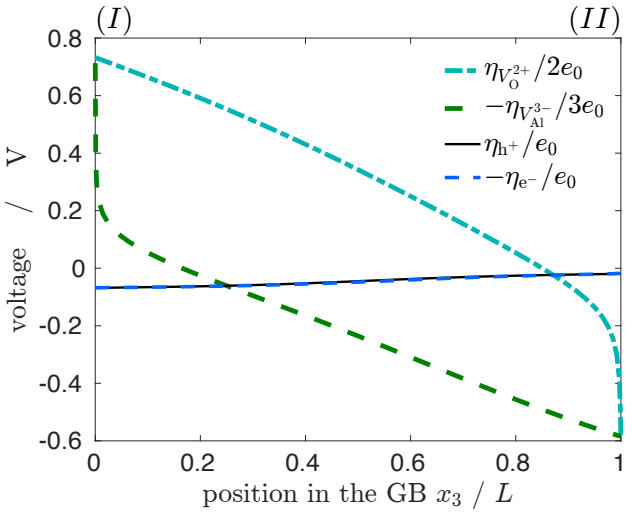

FIGURE 3.13: The voltages, $\eta_s/z_s e_0$, calculated from the ideal solution electrochemical potentials, of the mobile species for fixed $x_1 = a_\mathrm{hex}/4$ in the grain boundary plane. Schottky equilibrium is not satisfied in the grain boundary since $-\eta_{\mathrm{V}^{3-}_{\mathrm{Al}}}/3 \neq \eta_{\mathrm{V}^{2+}_{\mathrm{O}}}/2$, but electrons and holes are in equilibrium, $-\eta_\mathrm{e} = \eta_\mathrm{h}$. Calculation for $P^{II}_{\mathrm{O}_2}/P^{I}_{\mathrm{O}_2} = 10^6/10^{-9}$, $D_{\mathrm{V}^{2+}_{\mathrm{O}}} = 10^{-3}\,D_\mathrm{ref}$, $D_{\mathrm{V}^{3-}_{\mathrm{Al}}} = 0.01\,D_\mathrm{ref}$, and $D_\mathrm{e} = D_\mathrm{h} = 1\,D_\mathrm{ref}$, for other parameters see section 3.4.3.1. The thermal voltage is given by $k_\mathrm{B}T/e_0 = 0.16\,\mathrm{V}$, and $V_\mathrm{e} = -(\eta^{II}_\mathrm{e} - \eta^{I}_\mathrm{e})/e_0 = 50\,\mathrm{mV}$.

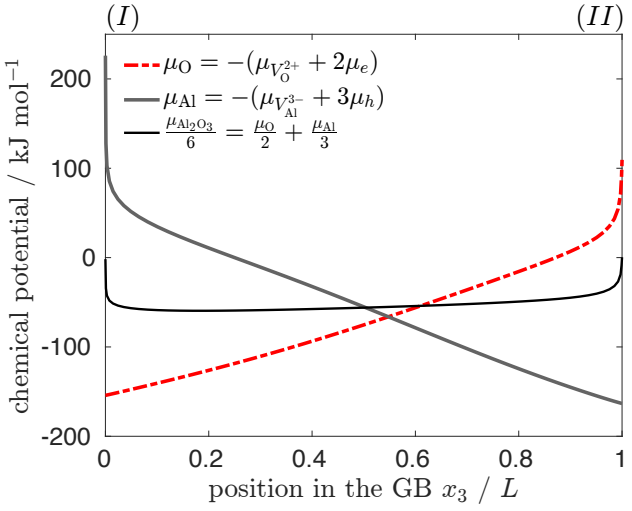

FIGURE 3.14: Component aluminum and oxygen chemical potential, μ_Al, and μ_O, for fixed $x_1 = a_\mathrm{hex}/4$ in the grain boundary plane. Schottky equilibrium holds at the surfaces where, $\mu_{\mathrm{Al_2O_3}} = 0$, but is not satisfied in the grain boundary. Same parameters are used as in figure 3.13.

The internal chemical potential distributions $\mu_{\mathrm{Al}}(x_3)$, and $\mu_{\mathrm{O}}(x_3)$ shown in figure 3.14 are different from those shown in figure 8 of reference [188] for polycrystalline alumina membrane permeation experiments. Schottky equilibrium together with electron-hole equilibrium implies $3\mu_{\mathrm{O}}+2\mu_{\mathrm{Al}} = 0$, which is not satisfied within the grain boundary, see figure 3.14, because $3\mu_{\mathrm{V}_{\mathrm{O}}^{2+}} + 2\mu_{\mathrm{V}_{\mathrm{Al}}^{3-}} \neq 0$. The qualitative discrepancy in the chemical potential distributions between reference [188] and this treatment is likely due to the assumption of Schottky equilibrium in [188].

A Schottky reaction term could be added to the transport equations 3.7, which would lead to Schottky equilibrium in the grain boundaries depending on the reaction and transport rates. However, the internal Schottky reaction with formation and dissolution of oxide at the grain boundaries would induce stress and cause a non-trivial modification in the permeation rate. The simulations discussed in this section are thought to correspond to the limit in which stress at the grain boundaries prohibits the formation and dissolution of oxide internally, similarly to its effect in the bulk material.

3.4.4 Discussion

The power laws for the oxygen permeation rate found experimentally in the limits of high and low applied oxygen pressures, are confirmed in the calculations with the slab model in the steady-state limit. The experiments are performed on 0.25 mm thick polycrystalline alumina membranes while the geometry of the slab in the calculations with $L = a_{\mathrm{hex}} = 1\,\mu$m is chosen to resemble more closely the situation of planar films growing with a columnar grain structure. The variation of the permeation rate, and the average conductivity with the oxygen chemical potential are related to the power law exponent n_ν, see figures 3.9 and 3.11, and equations 3.51 and 3.52. The power law exponent in turn depends on the stoichiometry of the quasi-chemical reactions at the surfaces, see equation 3.24. The applied pressure at which the transition between p-type and n-type ionic conductivity of the grain boundaries takes place depends on the ratio of the vacancy diffusion coefficients in the grain boundary, $D_{\mathrm{V}_{\mathrm{O}}^{2+}}/D_{\mathrm{V}_{\mathrm{Al}}^{3-}}$, given that $\mathrm{V}_{\mathrm{O}}^{2+}$, and $\mathrm{V}_{\mathrm{Al}}^{3-}$ are the mobile vacancy species.

The time-dependent calculations not only elucidate the initial transient behaviour but also help to clarify the steady-state. Varying the applied oxygen partial pressure from $P_{\mathrm{O}_2}^{\mathrm{eq}}$ to $P_{\mathrm{O}_2}^{\mathrm{hi}}$ or $P_{\mathrm{O}_2}^{\mathrm{lo}}$ on one of the surfaces changes the rate of creation and annihilation of vacancies, electrons and holes in stoichiometric proportions on the surface, the resulting chemical potential gradients between the surfaces along the grain boundaries drive the transport of species through the slab. The resulting fluxes of the mobile species depend on their diffusion coefficients and will therefore not necessarily preserve

the stoichiometric proportions of the surface populations of the species, except when all species have the same diffusion coefficient. The local charge density thereby becomes non-zero, and generates an electric field that retards the diffusion of the fastest dominant species, but enhances the diffusion of the slower dominant species which has an effective charge of opposite sign.

Three time scales involved in the dynamics of species concentration evolution are identified, τ_{c} (see equation 3.47) characterizes the rate of charge build-up on the surface and in the grain boundary, τ_{d} (see equation 3.49) characterizes the discharging of the grain boundary, and τ_{s} (see equation 3.50) characterizes the time to reach the steady-state at which $\nabla \cdot J_s \simeq 0$.

During the initial transient, $t \lesssim \tau_{\mathrm{c}}$, the different diffusion coefficients lead to the accumulation of charge in the grain boundary and on surface (II). If, for example in the $P_{\mathrm{O}_2}^{\mathrm{hi}}$ case, holes and aluminum vacancies are generated on surface (II), the holes, which are assumed to be the faster species, $D_{\mathrm{V}_{\mathrm{Al}}^{3-}} \ll D_{\mathrm{h}}$, diffuse away from the surface, generating positive charge density in the grain boundary, and surface (II) becomes negatively charged due to the aluminum vacancies. Once the holes reach surface (I) it becomes positively charged, and as the slower aluminum vacancies diffuse into the grain boundary it is discharged over a time $t \sim \tau_{\mathrm{d}}$. In this example the electric field effectively enhances the aluminum vacancy diffusion, and retards the diffusion of the oxygen vacancies and holes. In the steady-state limit the electrostatic potential difference between the surfaces, $\Delta\phi = \phi^{II} - \phi^{I}$, is on the order of the thermal voltage, $k_{\mathrm{B}}T/e_0$, in the high and low pressure limits considered. For the calculation shown in figure 3.13 with $P_{\mathrm{O}_2}^{II} = P_{\mathrm{O}_2}^{\mathrm{hi}}$ and $P_{\mathrm{O}_2}^{I} = P_{\mathrm{O}_2}^{\mathrm{lo}}$ the voltage between the surfaces observed in the simulations is $V_{\mathrm{e}} = -(\eta_{\mathrm{e}}^{II} - \eta_{\mathrm{e}}^{I})/e_0 = 50\,\mathrm{mV}$. V_{e} depends strongly on the species diffusion coefficients.

Physically, the mobile species distributions reconfigure to screen the electric field arising due to non-zero local charge density, and the Debye screening length (see equation 3.13) characterizes the spatial extent of the variations in the local charge density. Due to screening effects the local charge density and electrostatic potential are challenging to resolve numerically near the surfaces. For spatial variations in the charge density within the grain boundary the two-dimensional equivalent of the reference screening length, see equation 3.44, is found to be appropriate. Apart from the initial transient the electrostatic potential in the simulations is dominated by the contributions from the surface charges. In the parameter regimes investigated the non-zero charge density in the grain boundary does not affect the defect fluxes significantly, the 3D calculations can

therefore be mapped onto a 1D model. In the intermediate pressure regime the dominance of one vacancy species is less pronounced and in particular for $c_\nu(r,t) \sim c_\nu(t_0)$ in the steady-state the local charge neutrality approximation becomes invalid. For small species concentrations the Debye length gets larger, and the electric field gets weaker. Both of the later facts are considered responsible for the failure of the analytic model in the intermediate pressure regime, see figure 3.9.

The open circuit voltage has been determined and compared to a simplified 1D model, see figure 3.12. The measurement of the open circuit voltage in the permeation experiments could help to determine the relative magnitudes of the dominant species diffusion coefficients.

The simulations with the fixed oxygen chemical potential difference between the surfaces reach a stationary non-equilibrium state with a constant rate of entropy production. This means the populations of vacancies, electrons, and holes reach a dynamic equilibrium state, in which they are created and annihilated at the same rate and $\partial c_s/\partial t \simeq 0$, while the oxygen chemical potential difference sustains non vanishing fluxes between the surfaces.

3.5 Lateral growth stress

The stress state in growing scales is due to a superposition of multiple opposing generation and relaxation mechanisms acting simultaneously. Common examples of stress generation mechanisms are the lattice constant (Pilling-Bedworth ratio) and thermal expansion misfit between the alloy and scale [38, 169], and volume contractions due to phase transformations [183]. The focus here is on lateral growth stresses that occur due to the formation or dissolution of material within the scale during the growth process given that the scale is constrained by adhesion to the alloy substrate [24].

The growth stresses can be alleviated by plastic deformation in the alloy substrate, change in scale shape, plastic deformation in the scale, or diffusional creep in the scale. All these mechanisms have been observed in thermally grown alumina scales, wrinkling or rumpling shape changes of the scale are commonly observed phenomena. The resistance of alumina scales against cracking and spallation is critical to their application as oxidation barriers in coatings, where they are formed deliberately to protect the alloy substrate against oxidation [35, 37]. A detailed understanding of the evolution of lateral growth stresses is therefore indispensable for assessing the reliability of alumina scales.

Apart from the Frenkel interstitial and vacancy defect pair, vacancies in crystalline solids can only form at extended defects such as surfaces, interfaces, and dislocations. The vacancy formation is tied to steps, kinks and other microscopic properties of these extended defects. Given the availability of extended defects that can act as a sources and sinks for vacancies within the material, the attainment of equilibrium between anions and cations locally depends on the fluxes of the mobile species, and the reaction rates between the metal and oxidant vacancies.

In this section the hexagonal cell model described above is extended to describe metal oxidation with internal formation and dissolution of oxide inducing stress within the scale. The widely used industrial ceramic aluminum oxide, important as a protective layer in chemically severe conditions and at high-temperatures, again serves as an exemplary material for the application of the model. The model idealizes the columnar grain structure of growing oxide films as a lattice of hexagonal cells with identical cross-section. The transport of cations, anions, and electrons through the grain boundaries is modelled with the generic Nernst-Planck flux expression and the reactions between the point defect species are modelled with simple mass-action kinetics. Time-dependent simulations are performed taking into account the self-consistent electrostatic potential and space charge effects due to the charged mobile defects.

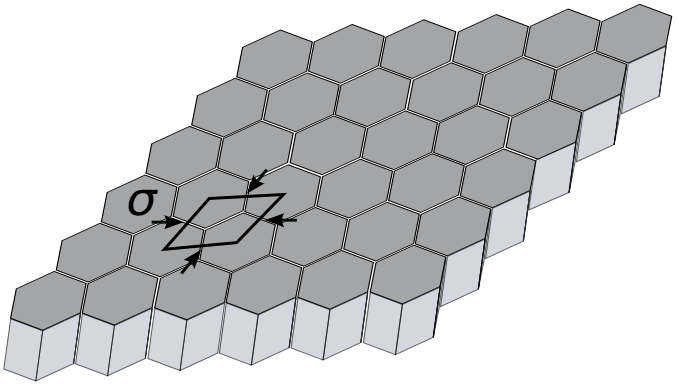

FIGURE 3.15: Hexagonal cell model including in plane stress σ.

The evolution of lateral growth stresses, induced by vacancy creation and annihilation at the grain boundaries, is simulated in this idealized three-dimensional grain structure, see figure 3.15. Some theoretical background in provided in section 3.5.3, related computational work is reviewed in section 3.5.4, and the novel approach developed here is described in section 3.5.5.

Compressive and tensile growth stresses have been observed in alumina scales growing during high-temperature oxidation of alloys. A brief summary of some experimental observations regarding lateral growth stresses is given in section 3.5.2. The Rhines-Wolf model [149] is frequently adopted to conceptualize growth stresses in alumina scales, it is further described in section 3.5.3. Based on 1D analytical considerations and some earlier work Atkinson [1, 166] has argued that anion and cation vacancy counter fluxes involving annihilation and creation of vacancies within growing scales can only induce tensile stresses.

These considerations are important for the interpretation of experimental work and with the computational approach detailed here it is possible to go beyond the simplifying assumptions made by Atkinson [1]. It can be investigated if vacancy mediated grain boundary diffusion including vacancy creation and annihilation can induce compressive stresses under specific conditions, and thereby determine if interstitial diffusion is indeed necessary to observe compressive stresses in the steady-state as was argued by Veal *et al.* [183]. The model proposed here should allow to determine if Atkinson's analytic analysis [1] holds in general and vacancy reaction-diffusion does indeed always induce tensile growth stress.

3.5.1 The alloy–oxide interface

Modelling an oxide adherent to a metal or alloy substrate requires to extend the membrane calculations, detailed in section 3.4, by including the metal–oxide or alloy–oxide interface. Such interfaces are of interest in a range of material systems including ceramics and semiconductor devices. A review with emphasis on thermodynamic aspects and empirical models pertaining to metal–ceramic interfaces has been given by Howe [76]. Minimization of the interfacial free energy typically results in ordered atomic structures at the interfaces [172]. Crucial thermodynamic variables for the interfacial properties relevant for oxidation are the oxidant partial pressure, temperature, time, and alloying additions to the metal. A review of essential theoretical concepts for modelling metal–ceramic interfaces was given by Finnis [42].

Three seminal theoretical concepts for understanding interfaces between metals and wide-band-gap oxides are band bending, metal-induced gap states, and the image interaction. Bending of the valence and conduction band is an ubiquitous phenomenon occurring at most interfaces except metal-metal junctions, it is of fundamental importance for many semiconductor devices and a comprehensive discussion can be found e.g. in the monograph by Sze [173] or in the more recent review [201]. At an interface with only electrons and holes as mobile charge carriers the Fermi-level (electron

electrochemical potential) is constant in their equilibrium configuration

$$\eta_{\mathrm{e}}(r) = \mu_{\mathrm{e}}(r) - e_0\phi(r) = \text{const.} \tag{3.69}$$

and the band bending is a consequence of the non-vanishing electrostatic potential, ϕ, variation near the interface. In cases where mobile point defects and gap states are present the distribution of valence and conduction band states near the interface is more complex.

Closely related to the band bending at the interface are the Fermi-level pinning and gap-states induced by joining a wide-band-gap oxide or semiconductor to a metal. Semiconductor surface states have been first discussed in detail by Heine [63] and comprehensive accounts can be found again in the semiconductor device literature e.g. [124]. The metal-induced gap states are not strictly localized, they are obtained from the requirement of continuity of the electron wave function at the metal–oxide interface which leads to states in the energy range of the oxide band gap decaying into the oxide from the position of the interface.

The classical image interaction has been shown by Finnis and co-workers to be the dominant term in the adhesion of ionic crystals to metals [41]. The image interaction refers to the force acting on a point charge that attracts it to a metal surface and that is thought to be mediated by the point charge's imaginary image.

For alumina scale growth the alloy substrate serves as an aluminum source and its properties have to be included in the boundary conditions for the model of the transport through the oxide. Here, effects due to an image interaction are not taken into account for the transport through the oxide film because the mobile charges in the hexagonal slab are not considered to generate a net electric field. Gap states and Fermi-level pinning at the interface are not considered explicitly, only the ficticious equilibrium interfacial oxygen partial pressure, $P^{\mathrm{int}}_{\mathrm{O}_2}$, is considered as a thermodynamic variable for the model. The partial pressure $P^{\mathrm{int}}_{\mathrm{O}_2}$ is expected to depend on the composition of the alloy substrate and temperature, and its value, ideally obtained from experimental thermodynamic data, is taken as an input for the calculations which are performed under isothermal conditions. Further details for modelling the alloy-oxide-gas system with the hexagonal cell model are found in section 3.5.5, where the calculation methodology for modelling lateral growth stresses due to internal oxidation is described.

3.5.2 Experimental evidence for lateral growth stress in α-Al_2O_3

Lateral growth stress generation due to internal formation or dissolution of scale requires a counter flux of metal and oxidant through the scale. Grain boundaries are the preferential transport pathways in alumina scales [68, 147] and the occurrence of an ionic counter flux has been convincingly demonstrated [3, 83, 136, 178].

The stress state in the oxide has been examined in numerous X-ray diffraction and piezo-spectroscopy studies at room temperature after cooling from the oxidation temperatures which are typically $\sim 1100 - 1200^\circ$ C [24]. Clarke *et al.* have determined growth stresses by piezo-spectroscopy of Cr^{3+} doped alumina measuring the frequency shift of the optical fluorescence transition lines due to stress [23, 98, 100, 101, 177]. The residual stress distributions are obtained after cooling the sample from oxidation temperatures $\sim 1100-1200^\circ$ C to room temperature which introduces compressive thermal expansion misfit stresses that are several times larger than the growth stresses [177], and vary with the alloy ~ -3 GPa [98]. Compressive growth stresses of -200 MPa to -300 MPa have been deduced from these studies [101, 177]. From spectral line broadening stress gradients are deduced of 2.6 GPa/μm for $\sim 1.2\,\mu$m thick films. Creep is considered to be the major relaxation process in thin films, while substrate deformation becomes significant at later stages of oxidation at high temperatures [177].

Uncertainties in the thermal expansion coefficients and stress relaxation during cooling limit the reliability and accuracy of growth stresses determined from these experiments [24, 25].

X-ray scattering has been applied to study stresses in alumina [152, 157]; however, the X-ray scattering cross-section of alumina is narrow producing weak diffraction patterns. Compressive growth stresses on the order of -1 GPa which partly relax to ~ -0.5 GPa, have been measured on FeCrAl(Y) alloys, while the growth stresses on NiAl were zero within the experimental uncertainty of ± 170 MPa [152]. Yttrium additions were found to decrease lateral scale growth but not to decrease growth stresses which were relaxed by plastic scale and alloy deformation. Veal *et al.* [183, 184] have performed *in situ* X-ray synchrotron experiments for oxidation of different alloys at high temperature 1100° C. They observed tensile stresses in steady-state for alloys containing reactive elements and compressive stresses for alloys without reactive elements, the stresses being on the order of ± 200 MPa in steady-state. Creep relaxation is considered to balance the stress generation by relaxation in steady-state. They argue that the θ to α-Al_2O_3 phase transformation during early oxidation stages introduces tensile stresses due to volume contraction. Using the same technique tensile growth stresses of 130 MPa and 200 MPa at 1000° C and 1100° C respectively, have been observed during

oxidation of a Y containing bond-coat alloy [35, 148]. Residual compressive stresses of -2.1 GPa and -4.8 GPa are found upon cooling to room temperature from oxidation temperatures of 1000° C and 1100° C respectively, and attributed to thermal expansion misfit.

3.5.3 Theoretical background

In the field theory of mechanical stresses in solids the interatomic forces are abstracted and taken into account through a coarse grained description. The macroscopic deformations are described in terms of displacements of volume elements whose size is large compared to the interatomic distances, and small compared to the macroscopic dimensions of the crystallites. The solid 'body' is mathematically described by a continuum of points and the force-over-area limit at each point yields the stress state locally. Subjecting a solid to a planar cut the magnitude and direction of the mechanical force required to restore the remaining material to the state before the cut may vary from point to point in the cut plane.

The theory of crystal shape change by self-diffusion in a polycrystalline material under applied stress was elaborated by Herring [67]. Resembling the macroscopic behaviour of a viscous fluid the grains are imagined to deform by diffusional flow of matter from grain boundary areas under compressive stress to those under tensile stress. Such diffusional flow is frequently found as the mechanism of creep at high-temperatures and low stresses [5]. The viscoelastic behaviour of solids is distinct from that of viscous fluids in that the solid can reach a mechanical equilibrium with an applied stress that includes a shear component. A discussion of the elasto-chemical equilibrium problem including precise definitions of the relevant phenomenological quantities has been given by Larché and Cahn [90].

As the crystal is strained due to the addition or removal of atoms internally work is performed. The chemical potential of a vacancy species at the grain boundary is modified with respect to the chemical potential in the unstrained solid, μ_s, by an additional term

$$\mu_s'(T, c_s, \sigma_{ij}) = \mu_s(T, c_s) + \sigma_{ij}\epsilon_{ij}V_0 \tag{3.70}$$

that takes into account the work required to deform the crystal with unstrained volume, V_0, if material is added or removed locally. The tensors σ_{ij} and ϵ_{ij} characterize the stress and strain state, respectively [5, 137]. Vacancy accumulation and void formation at

extended defects thus generates tensile stress making further accumulation energetically less favourable as is discussed for example in [78].

Comprehensive reviews of stress and related effects in high-temperature oxidation have been given by Stringer [169] and Evans [36, 38]. The Rhines-Wolf model [149] was developed to conceptualize compressive growth stress in NiO scales during high-temperature oxidation, and has been adopted for other materials since. The anion and cation transport in the nickel oxide layer of columnar grains is found to be confined to the grain boundaries [149]. In the Rhines-Wolf model the build-up of compressive stresses within growing scales is attributed to vacancy annihilation and oxide formation at grain boundaries traversing the scale normal to the substrate, see figure 3.16

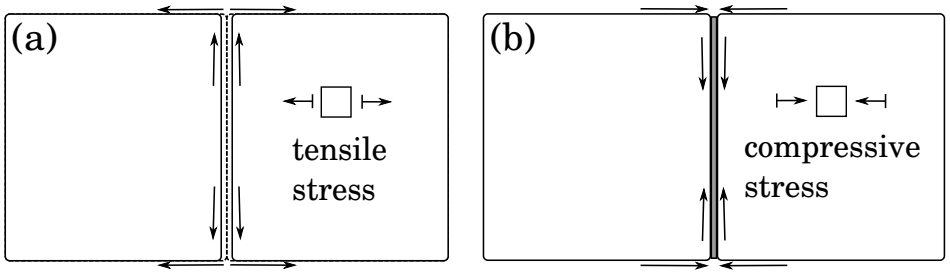

FIGURE 3.16: Compressive compared to tensile stress due to material being removed (a) or added (b) at the grain boundary separating two grains. Assuming the grains themselves are subject to an external force preventing stress relaxation by rigid displacement of the individual grains.

Atkinson developed an analytic model and argued that an anion and cation vacancy counter flux generally leads to tensile stresses within the growing scale [1]. Atkinson's treatment adopts a one-dimensional model derived from the Wagner theory of metal oxidation [189]. Grain boundaries and the interfaces are not treated explicitly and only steady-state concentration distributions are analyzed. The reaction equilibrium constants that are essential for the analysis therefore assume the meaning of effective parameters satisfying the one-dimensional equations; their value in the grains, at the grain boundary, the surface, and the alloy–oxide interface is not distinguished.
Veal *et al.* [183] follow Atkinson's [1] analysis and argue that vacancies and interstitials diffuse simultaneously through the alumina grain boundaries. The interstitials are thought to be 'blocked' by the reactive elements which segregate to the grain boundaries and thereby lead to predominant vacancy annihilation introducing tensile stress, in scales on reactive element containing alloys. In the absence of reactive elements it is argued that interstitial diffusion through the grain boundaries is predominant and their annihilation introduces compressive stress [183].

More complex ionic transport mechanisms than simple point defect hopping have been proposed in the literature on grain boundary diffusion in alumina, and the suggested mechanisms are often closely related to the stress state at the grain boundaries. Clarke has proposed that the cations and anions could be trapped at dislocation cores with subsequent climb of the dislocations through the thickness of the oxide [25]. As described in section 2.5, Heuer *et al.* have proposed a 'disconnection' mechanism for atomic transport through alumina grain boundaries [71, 72, 75].

3.5.4 Previous modelling approaches

Krishnamurthy and Srolovitz have developed a two-dimensional continuum model with a model structure of rectangular grains. Oxide creation and stress generation is considered at the grain boundaries separating the rectangular grains together with diffusive mass transfer [88, 89]. Fickian-diffusion and stress-driven transport are considered in time-dependent simulations [89]. However, electric field effects and electron-hole transport are not taken into account, only transport of neutral atomic species.

Limarga *et al.* [96] have presented an analytic steady-state model that only considers oxygen vacancy diffusion and does not consider the dynamical competition between stress generation and relaxation mechanisms. Electric field effects and electron-hole transport are also not taken into account.

A mathematically similar problem to the lateral growth stress evolution in oxides is found in the stress and electromigration analysis of failures in the Al-lines (interconnects) of integrated circuits [16]. Kirchheim has provided a detailed study including electric field effects, stress-driven and diffusive transport together with a vacancy annihilation mechanism at the model grain boundaries [82]. A two-dimensional square tiling is adopted as the model grain structure [82].

3.5.5 Modelling the effect of stress in the hexagonal cell model

The hexagonal cell model allows for three-dimensional simulations taking into account the defect transport through the grain boundaries self-consistently with the stress-evolution and distribution. The equations for the drift-diffusion transport have been described in sections 2.6 and 3.2.2. Stress effects due to creation and annihilation of vacancies at the rectangular grain boundaries within the idealized hexagonal grain structure, see figure 3.15, are examined in what follows.

The elastic properties of the hexagonal cell polycrystal depend on the single-crystal elastic constants of the prismatic crystallites. Figure 3.17 shows a terrace-kink

model schematic for the interface structure of the irreducible zone of an individual hexagonal grain. By joining two low index crystal surfaces a small-angle symmetrical tilt grain boundary between two adjacent cells is constructed, the surface steps become edge dislocations [172].

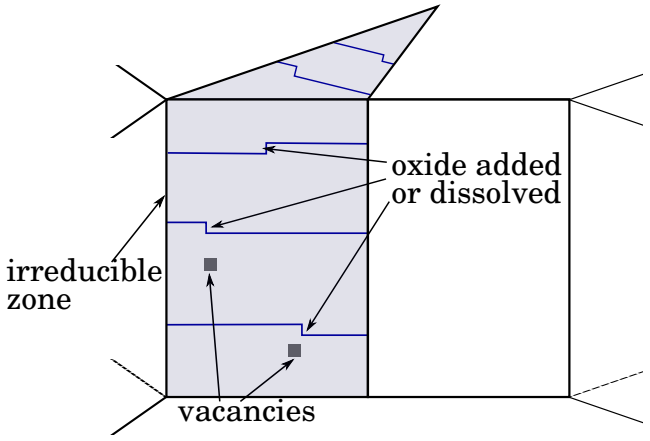

FIGURE 3.17: Terrace-kink schematic of the irreducible zone of a hexagonal cell. The rectangular grain interface plane is thought to be joined by an identical grain thereby constructing the grain boundary between two adjacent hexagonal grains.

Although the microscopic process of oxygen incorporation by the lattice, or the reverse process, has not yet been elucidated, I adopt a plausible description of the process, which leaves the boundary essentially unaltered in its structure. The oxide molecules are thought to be inserted at the grain boundaries creating a new layer of oxide in a self-similar manner, see figures 3.18 and 3.17, in the direction perpendicular to the alloy substrate and oxide surface. In other words crystal planes are added or removed by dislocation climb, the grains contract or expand and – due to the lateral dimensional restriction – in-plane compatibility stresses arise. No modification of the point defect diffusion coefficient due to stress is considered, the average properties of the grain boundary structure are thought to be preserved. The stress state is thought only to modify the Gibbs free energy of formation of the Schottky defect at the boundary. Furthermore, no spatial variation in the stress state is considered in the grain boundary plane and consequently no material transport due to a stress gradient.

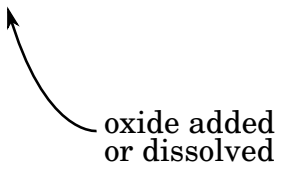

FIGURE 3.18: Schematic of a symmetrical low-angle tilt grain boundary. Oxide molecules are thought to be added at the grain boundary in such way as to preserve the grain boundary character, a self-similar process.

For the purpose of the simulation study to be discussed in section 3.5.6 the reaction rate constants, diffusion coefficients, and equilibrium constants enter as parameters. The microscopic details shown in the figures 3.18 and 3.17 do not enter explicitly in the continuum model. These details are discussed here for clarity of concept, and to establish a connection to related *ab initio* simulation work, such as the DFT calculations by Guhl *et al.* [56], and other related simulation methodologies.

Oxide is exchanged between the grain boundaries of the oxide polycrystal, the surface, and the alloy–oxide interface for the combined thermodynamic system alloy–oxide–atmosphere to attain a lower free energy state. The creation and annihilation process of lattice at the grain boundary is distinct from those at the surface and alloy–oxide interface since the later processes do not generate stress. The stress due to insertion of oxide molecules at the alloy–oxide interface is thought the be relaxed by rigid displacement of the oxide with respect to the substrate, the stress due to the lattice mismatch at the alloy–oxide interface is not considered here. Adding or removing oxide molecules at the rectangular interfaces of a hexagonal cell the relative change in cell volume is given by

$$\frac{\delta V}{V} = \frac{V' - V}{V} = \frac{2\Delta a_{\text{hex}}}{a_{\text{hex}}} + \frac{\Delta L}{L}. \tag{3.71}$$

However, the cross-section area of the hexagonal cells, see figure 3.19, in the material is constrained by the adjacent grains and the adhesion of the film to the alloy substrate, this means stress is induced.

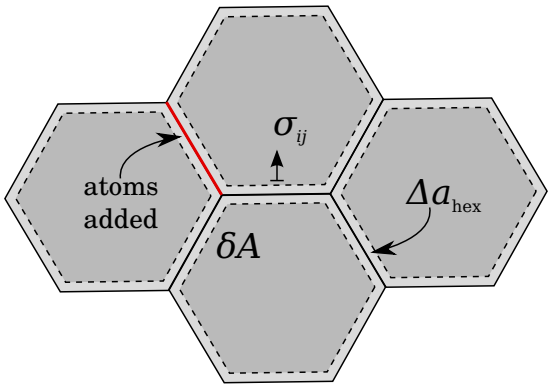

FIGURE 3.19: Top down view of the idealized hexagonal grain structure under in-plane compressive stress.

The relative change in volume is related to the normal strains by

$$\frac{\delta V}{V} = \text{Tr}\left(\epsilon_{ij}\right) = \epsilon_{11} + \epsilon_{22} + \epsilon_{33} \tag{3.72}$$

which is invariant under rotations of the coordinate system. In the absence of shear displacements, and in the coordinate system connecting the centers of the grains, see figure 3.20, the only non-vanishing stress components for in-plane strain with $\sigma_{33} = 0$, are the the normal stresses and due to the hexagonal symmetry $\sigma_{11} = \sigma_{22} = \boldsymbol{\sigma}$. Similarly, the in-plane normal strains are related $\epsilon_{11} = \epsilon_{22} = \boldsymbol{\epsilon}$

$$\frac{\delta V}{V} = 2\boldsymbol{\epsilon} + \epsilon_{33} \tag{3.73}$$

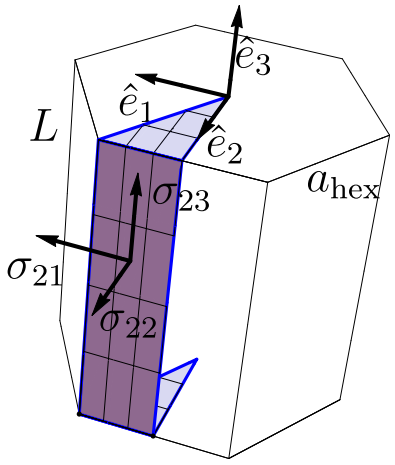

FIGURE 3.20: Irreducible zone of the hexagonal cell. The coordinate system is defined. The normal stress sign conventions is defined by tensile $\sigma_{22} > 0$, and compressive $\sigma_{22} < 0$ stress.

The stress and strain fields are connected by material laws also referred to as constitutive equations such as Hooke's law in linear elasticity theory which in generalized form is written in index notation as

$$\sigma_{ij} = C_{ijkl}\,\epsilon_{kl} \tag{3.74}$$

where C_{ijkl} is the fourth-order stiffness tensor, the components of which are related to the engineering elastic moduli [137]. In general anisotropic elasticity the stiffness tensor has 21 independent components which reduces to 5 for crystalline materials with hexagonal symmetry such as α-Al_2O_3. Imagining the individual alumina grain – for simplicity – to be constructed by repetition of a corundum conventional cell with the c-axis aligned to the $\hat{e}_3$ axis of the hexagonal cell structure, the calculation the elastic constant is readily performed. Due to the hexagonal symmetry Hooke's law reduces to two coupled scalar equations

$$\boldsymbol{\sigma} = (C_{11} + C_{12})\boldsymbol{\epsilon} + C_{13}\epsilon_{33} \tag{3.75}$$

$$0 = 2C_{13}\boldsymbol{\epsilon} + C_{33}\epsilon_{33} \tag{3.76}$$

and the stress-strain relation is written as

$$\boldsymbol{\sigma} = C\boldsymbol{\epsilon} \quad \text{with} \quad C = C_{11} + C_{12} - 2\frac{C_{13}^2}{C_{33}} \tag{3.77}$$

where the 2-indices Voigt notation [137] is used, and an effective elastic constant C is introduced.

Treating the crystal orientation of the individual grains as unknown the elastic properties of the hexagonal cell slab could be calculated from the effective elastic constants of an alumina polycrystal. This means Hooke's law for isotropic materials is applied with effective elastic constants of the polycrystal, hence

$$\epsilon_{ij} = \frac{1}{Y}\left(\sigma_{ij}\,(1+\nu) - \nu\delta_{ij}\sigma_{kk}\right) \tag{3.78}$$

where Y is the effective Young's modulus and ν is the effective Poisson ratio. The in-plane stress in the absence of shear, and for $\epsilon_{11} = \epsilon_{22} = \boldsymbol{\epsilon}$ is therefore given by

$$\boldsymbol{\sigma} = \sigma_{11} = \sigma_{22} = \frac{Y}{1-\nu}\boldsymbol{\epsilon} \tag{3.79}$$

while $\sigma_{33} = 0$. Compared to the anisotropic treatment under the simplifying assumption of the special alignment of the crystallite c-axis a different elastic constant in the

stress-strain relation is obtained. For the single crystal stiffness matrix elements at room temperature according to reference [187], the constants in GPa read as

$$C_{11} = 496.8, \quad C_{12} = 163.6, \quad C_{13} = 110.9, \quad \text{and} \quad C_{33} = 498.1, \tag{3.80}$$

$$C = C_{11} + C_{12} - 2\frac{C_{13}^2}{C_{33}} = 611\,\text{GPa}. \tag{3.81}$$

The polycrystal effective elastic (Young's) modulus and Poisson ratio determined from experiments on a dense α-Al_2O_3 polycrystals at room temperature [128] are given by

$$Y = 416\,\text{GPa}, \quad \text{and} \quad \nu = 0.231, \tag{3.82}$$

$$Y' = \frac{Y}{1-\nu} = 541\,\text{GPa}. \tag{3.83}$$

The different approaches, hence, yield elastic constants C and Y' that differ in magnitude by about 10%. The polycrystal elastic modulus, Y, is found to decrease by about 20% in the temperature range from 20 to 1500° C [128]. Both, the temperature dependence and crystallite orientation should be taken into account in principal, since the polycrystal elastic constants are available in the desired temperature range the experimental polycrystal data from reference [128] is used in the following discussion.

For inserting an extra plane of atoms between any two adjacent grains of the slab, Δa_{hex} is identified with $1/2$ times the modulus of the Burgers vector, b, of the dislocations that the grain boundary is composed of, hence

$$\boldsymbol{\epsilon} = \frac{b}{2a_{\text{hex}}}. \tag{3.84}$$

For ΔN oxide molecules added to the irreducible zone of the grain boundary rectangle the strain is written as

$$\boldsymbol{\epsilon}(\Delta N) = \frac{b}{2a_{\text{hex}}}\frac{\Delta N}{N} = 2\frac{\Omega_{\text{u}}\Delta N}{a_{\text{hex}}^2 L} \tag{3.85}$$

where $N = ba_{\text{hex}}L/4\Omega_{\text{u}}$ is the number of oxide molecules added for inserting a whole extra plane of material, and where $\Delta N > 0$ describes a net addition of material at the grain boundary. The expression is similar to the notion of $\delta V/V$ introduced above.

The Schottky reaction mechanism at the grain boundary is understood in such way that a Schottky vacancy complex annihilates as oxide is removed at the grain boundary. Denoting the net amount of oxide that has been added or removed at the

grain boundary plane up to time t by $\Delta N(t)$, the stress state is written as

$$\boldsymbol{\sigma}(t)\Omega_{\mathrm{u}} = -2\frac{Y}{1-\nu}\frac{\Omega_{\mathrm{u}}^2}{a_{\mathrm{hex}}^2 L}\Delta N(t) \tag{3.86}$$

where again $\Delta N > 0$ describes a net addition (compressive stress), and $\Delta N < 0$ a net removal of material (tensile stress).
The energy contribution to the Schottky defect formation energy, E_{S}^f, due to to the amount of oxide that has been added or removed up to time t is therefore written as

$$G_{\mathrm{S}}^f = E_{\mathrm{S}}^f + \boldsymbol{\sigma}(t)\Omega_{\mathrm{u}}. \tag{3.87}$$

The Schottky equilibrium constant taking into account the stress-strain state is written as

$$K_{\mathrm{S}}' = K_{\mathrm{S}} \exp\left(\frac{\boldsymbol{\sigma}\Omega_{\mathrm{u}}}{k_{\mathrm{B}}T}\right). \tag{3.88}$$

The change of the oxygen and aluminum vacancy concentrations due to the Schottky reaction are related by the stoichiometry

$$\frac{1}{3}\partial_t c_{\mathrm{V}_{\mathrm{O}}^{2+}} = \frac{1}{2}\partial_t c_{\mathrm{V}_{\mathrm{Al}}^{3-}} = \partial_t \xi_{\mathrm{S}} \tag{3.89}$$

where the reaction-coordinate ξ_{S} is introduced for notational convenience. The reaction free energy of the Schottky reaction is written as

$$g_{\mathrm{S}}(r,t) = -3\mu_{\mathrm{V}_{\mathrm{O}}^{2+}}(r,t) - 2\mu_{\mathrm{V}_{\mathrm{Al}}^{3-}}(r,t) - \boldsymbol{\sigma}(t)\Omega_{\mathrm{u}} \tag{3.90}$$

where the vacancy chemical potentials are equated to the negative of the respective ionic species chemical potential, $\mu_{\mathrm{V}_{\mathrm{O}}^{2+}} = -\mu_{\mathrm{O}}^z$ and $\mu_{\mathrm{V}_{\mathrm{Al}}^{3-}} = -\mu_{\mathrm{Al}}^z$. In this notation the variation in the Gibbs free energy density is given by

$$dg = \sum_i \left(\mu_i + z_i e_0 \phi\right) dc_i - \boldsymbol{\sigma}\Omega_{\mathrm{u}} = -g_{\mathrm{S}}\, d\xi_{\mathrm{S}} + \phi\, d\rho + \mu_{\mathrm{e}}\, dc_{\mathrm{e}} + \mu_{\mathrm{h}}\, dc_{\mathrm{h}} \tag{3.91}$$

where the free energy of reaction is defined in equation 3.90, ϕ is the electrostatic potential, and ρ is the local charge density. The free energy of reaction, g_{S}, introduced above is considered distinct from the chemical affinity

$$\mathcal{A}_{\mathrm{S}}(r,t) = 3\mu_{\mathrm{V}_{\mathrm{O}}^{2+}}(r,t) + 2\mu_{\mathrm{V}_{\mathrm{Al}}^{3-}}(r,t) \tag{3.92}$$

in that g_{S} includes the free energy contribution due to compositional changes as a function of position, r, and a mechanical work term that only depends on time in the present model

$$\Delta W = -\boldsymbol{\sigma}(t)\Omega_{\mathrm{u}}. \tag{3.93}$$

The deviation from chemical equilibrium locally can be due to kinetic limitations or caused by the stress induced, and $g_{\mathrm{S}}(r,t)$ is therefore the quantity of choice to describe the vacancy equilibration process locally.

Using simple mass-action kinetics a stress-dependent reaction rate within the grain boundary is readily obtained. The reaction rate for vacancy annihilation and creation at the grain boundary plane at position r and at time t written as

$$\partial_t \xi_{\mathrm{S}}(r,t) = k_{\mathrm{S}} \left(- \left(c_{\mathrm{V}_{\mathrm{O}}^{2+}} \right)^3 \left(c_{\mathrm{V}_{\mathrm{Al}}^{3-}} \right)^2 + K_{\mathrm{S}} \exp\left(\boldsymbol{\sigma}\Omega_{\mathrm{u}} \,/\, k_{\mathrm{B}}T \right) \right) \tag{3.94}$$

where k_{S} is the reaction rate constant. The net number of oxide molecules added, $\Delta N > 0$ or removed, $\Delta N < 0$, at the grain boundary over time is given by

$$\Delta N(t) = \int_0^t \int_{\text{GB rect.}} \xi_{\mathrm{S}}(r',t')\, d^3r' dt' \tag{3.95}$$

where the grain boundary rectangle integration zone is defined in figure 3.2 by $\overline{ABCD}$. For the numeric calculations the differential and integral equations are discretized which leads to

$$\xi_{\mathrm{S}}^{i,n} = \xi_{\mathrm{S}}^{i,n-1} - \Delta t_n k_{\mathrm{S}} \left(\left(c_{\mathrm{V}_{\mathrm{O}}^{2+}}^{i,n} \right)^3 \left(c_{\mathrm{V}_{\mathrm{Al}}^{3-}}^{i,n} \right)^2 - K_{\mathrm{S}} \exp\left(\boldsymbol{\sigma}^{i,n-1}\Omega_{\mathrm{u}} / k_{\mathrm{B}}T \right) \right) \tag{3.96}$$

$$\Delta N^{i,n} = \xi_{\mathrm{S}}^{i,n}\, v_i \tag{3.97}$$

$$\Delta N^{n} = \sum_i \Delta N^{i,n} \tag{3.98}$$

where the superscript 'i,n' is a shorthand for the dependence on the the position $r_i = (x_1^i, x_2^i, x_3^i)$ on the grid and the n-th point in time, t_n, and v_i is the i-th volume element.

The coefficient of ΔN in the simulations is modified to obtain faster convergence to the steady-state

$$R_{\mathrm{S}} = k_{\mathrm{S}} \left(- \left(c_{\mathrm{V}_{\mathrm{O}}^{2+}} \right)^3 \left(c_{\mathrm{V}_{\mathrm{Al}}^{3-}} \right)^2 + K_{\mathrm{S}} \exp\left(- \Delta N \cdot f \right) \right) \tag{3.99}$$

where the constant f is chosen much larger than calculated from the above consideration. The modification could be thought of artificially increasing the stiffness of the material, this means the amount of material added or removed overall is changed, but the value of the steady-state stress is not affected, only the time-dependence of the stress evolution.

The electron hole annihilation reaction is considered at the grain boundary, interface, and surface

$$R_{\text{eh}} = -k_{\text{eh}} \left(c_{\text{e}} c_{\text{h}} - K_{\text{eh}} \right). \tag{3.100}$$

The oxygen vacancy creation is considered at the alloy-scale interface expressed by

$$R_{\text{V}_{\text{O}}^{2+}} = -k_{\text{O}} \left(c_{\text{V}_{\text{O}}^{2+}} \left(c_{\text{e}} \right)^2 + K_{\text{V}_{\text{O}}^{2+}} \left(P^{I}_{\text{O}_2} / P^{\text{eq}}_{\text{O}_2} \right)^{-1/2} \right) \tag{3.101}$$

and the aluminum vacancy creation is taken into account at the oxide–gas surface as

$$R_{\text{V}_{\text{Al}}^{3-}} = -k_{\text{Al}} \left(c_{\text{V}_{\text{Al}}^{3-}} \left(c_{\text{h}} \right)^3 + K_{\text{V}_{\text{Al}}^{3-}} \left(P^{II}_{\text{O}_2} / P^{\text{eq}}_{\text{O}_2} \right)^{3/4} \right). \tag{3.102}$$

The constants K_i are chosen such that in equilibrium $R_i = 0$.

3.5.6 Simulation results

The simulations correspond to oxidation experiments in which $\sim 1\,\mu$m thick α-Al_2O_3 films are grown on aluminum containing alloy substrates. The cross-section of the hexagonal cells is considered fixed and the addition or removal of oxide at the rectangular grain boundary planes strains the polycrystalline film. The simulations discussed here are performed for a constant film thickness of $1\,\mu$m, the quantity of primary interest is the steady-state (stationary) stress, $\boldsymbol{\sigma}^{\text{st}}$. The stress feedback to the Schottky reaction is taken into account together with the defect concentrations and fluxes locally in a self-consistent manner.

3.5.6.1 The equilibrium constants

The electron-hole equilibrium constant, K_{eh}, the Schottky equilibrium constant, K_{S}, and the diffusion coefficients, D_s, are key parameters in this model. The values of the

equilibrium constants are expected to depend on the phase or interface of the alloy-scale-gas system considered. The dimensionless ratio, β,

$$\beta = \frac{K_{\mathrm{S}}^{1/5}}{K_{\mathrm{eh}}^{1/2}} \quad \text{where} \quad K_{\mathrm{eh}} = c_{\mathrm{e}} c_{\mathrm{h}} \quad \text{and} \quad K_{\mathrm{S}} = c_{\mathrm{V}_{\mathrm{O}}^{2+}}^{3} c_{\mathrm{V}_{\mathrm{Al}}^{3-}}^{2} \tag{3.103}$$

denotes the ratio of the geometric means of the vacancy concentration, $K_{\mathrm{S}}^{1/5}$, and the electron-hole concentrations, $K_{\mathrm{eh}}^{1/2}$. Small changes in the defect formation energies, e.g. G_{S}^{f}, or the band gap lead to large changes the equilibrium constants, the parameter β changes less rapidly and is more convenient for the discussion. Its value at the alloy-scale interface, β_I, at the grain boundary, β_{GB}, at the scale–gas interface, β_{II}, and in the bulk material, β_{bulk}, are distinguished. Values for β in bulk α-Al_2O_3 are given in the experimental study of reference [123] for temperatures between $1000 - 2000\,\mathrm{K}$ where approximately $10 > \beta_{\mathrm{bulk}} > 0.001$, see figure 2 in reference [123]. In the analytic investigation of Atkinson [1] it was assumed that the same equilibrium constants are applicable throughout, and the generation of tensile or compressive stress is predicted based on the point defect diffusion mechanism, see table 1 in reference [1]. Here, in addition to the special case

$$\beta_I = \beta_{\mathrm{GB}} = \beta_{II} \tag{3.104}$$

results for the case of

$$K_{\mathrm{S}}^{I} \ll K_{\mathrm{S}}^{\mathrm{GB}} = K_{\mathrm{S}}^{II} \quad \text{and hence} \quad \beta_I \ll \beta_{\mathrm{GB}} = \beta_{II} \tag{3.105}$$

are discussed, where the Schottky equilibrium constant at the alloy–scale interface is varied to study its effect on the steady-state stress, $\boldsymbol{\sigma}^{\mathrm{st}}$.

Lateral stress generation is of particular interest for scale growth on Al containing superalloys such as FeCrAl. The incipient melting temperature for superalloys is $\sim 1600\,\mathrm{K}$, which is significantly lower than the $1900\,\mathrm{K}$ at which most of the permeation experiments by Kitaoka *et al.* [83] have been performed. The equilibrium oxygen partial pressure at the alloy–oxide can be obtained from experiment and it is highly temperature dependent. For the FeCrAl(Zr) superalloy the oxygen partial pressure at the alloy–oxide interface is calculated from thermodynamic data[1] to be $P_{\mathrm{O}_2}^{\mathrm{int}} = 5.6 \times 10^{-18}\,\mathrm{Pa}$ at $1600\,\mathrm{K}$. The equilibrium constants are chosen in a similar way as in the calculations performed

[1] J. Smialek private communication.

for the study of the membrane experiments, see section 3.4.3.1. The equilibrium constants are defined with respect to an equilibrium oxygen partial pressure, $P^{\text{eq}}_{\text{O}_2}$, and considered to correspond to a temperature of $1600\,\text{K}$. The oxygen partial pressure at which the vacancy concentrations are stoichiometric is found at $P^{\text{eq}}_{\text{O}_2} \approx 10^{-3}\,\text{Pa}$ at $1900\,\text{K}$ in reference [138] based on DFT data for bulk α-Al_2O_3. From the experimental thermodynamic data and analysis of reference [123] on bulk alumina it is known that the ratio β_{bulk} decreases with decreasing temperature ([123] figure 2).

Here, the reference vacancy concentrations are chosen as $c^0_{V^{2+}_{O}} = 2/3 c^0_{V^{3-}_{Al}} = 5 \times 10^{14}\,\text{cm}^{-3}$, and the reference electron and hole concentrations are chosen as $c^0_{\text{e}} = c^0_{\text{h}} = 10^{15}\,\text{cm}^{-3}$, which corresponds to a reduction of $\beta/10$ compared to the membrane simulations 3.4.3. Implicitly defining an equilibrium oxygen partial pressure, $P^{\text{eq}}_{\text{O}_2}$, the reaction equilibrium constants are calculated as described in section 3.4.3.1. The reference oxygen partial pressure in the simulations, $P^{\text{eq}}_{\text{O}_2}$, is considered to correspond to $P^{\text{eq}}_{\text{O}_2} \sim 10^{-3}\,\text{Pa}$. The simulations described below are performed for an oxygen chemical potential difference across the film defined by $P^{I}_{\text{O}_2}/P^{\text{eq}}_{\text{O}_2} = 10^{-14}$ and $P^{II}_{\text{O}_2}/P^{\text{eq}}_{\text{O}_2} = 10^{8}$, unless indicated otherwise. The temperature is set to $1600\,\text{K}$, and the diffusion coefficients are defined with respect to a reference diffusion coefficient, D_{ref}, that together with the thickness $L = 1\,\mu\text{m}$ defines the time scale in the simulations, $t_{\text{ref}} = L^2 D^{-1}_{\text{ref}}$. The values D_s are indicated together with the simulation results. The hexagon side length is set to $a_{\text{hex}} = 0.8\,\mu\text{m}$. The reaction rate constants for the reactions defined in equations 3.99, 3.100, 3.101, and 3.102, are set to $k_{\text{S}} = k_{\text{eh}} = 10^4$, and $k_{\text{O}} = k_{\text{Al}} = 10^2$.

3.5.6.2 The steady-state stress

Figure 3.21 shows the temporal evolution of the stress state converging to a steady-state tensile stress of. Typically a constant steady-state stress value $\boldsymbol{\sigma}^{\text{st}} > 0$ is reached in the simulation method developed, and its value depends on the diffusion coefficients, equilibrium constants, and also the reaction rate constants. In the simulation result shown in figure 3.21. The diffusion coefficients of the vacancies are taken as equal $D_{V^{2+}_{O}} = D_{V^{3-}_{Al}} = D_{\text{vac}}$, as well as the electron and hole diffusion coefficients $D_{\text{e}} = D_{\text{h}} = D_{\text{eh}}$. Simulation results for different ratios of $D_{\text{vac}}/D_{\text{eh}}$ are shown in figure 3.21, and the magnitude of steady-state stress, $\boldsymbol{\sigma}^{\text{st}}$, increases with a decreasing ratio $D_{\text{vac}}/D_{\text{eh}}$.

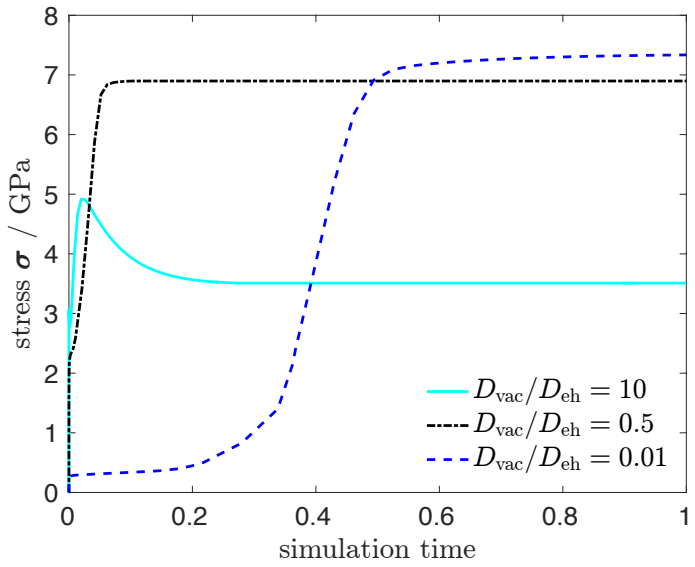

FIGURE 3.21: Evolution of the stress state at the grain boundary. The magnitude of stress converges to a steady-state value, constant as a function of time, and in this model also constant as the position in the grain boundary plane. The ratio of the oxygen partial pressures at the alloy–oxide interface, $P^{I}_{\mathrm{O}_2}$, and oxide–gas surface, $P^{II}_{\mathrm{O}_2}$, is given by $P^{II}_{\mathrm{O}_2}/P^{I}_{\mathrm{O}_2} = 10^{22}$ and corresponds to a oxygen chemical potential difference of $\Delta\mu_{\mathrm{O}_2} = N_{\mathrm{A}} k_{\mathrm{B}} T \log\left(P^{II}_{\mathrm{O}_2}/P^{I}_{\mathrm{O}_2}\right) = 674\,\mathrm{kJ\ mol^{-1}}$. The amount of steady-state stress increases with a decreasing value of the ratio $D_{\mathrm{vac}}/D_{\mathrm{eh}}$.

The possibility of faster vacancy diffusion than electron and hole diffusion is typically neglected in the literature on transport in alumina, except for Heuer [71]. But, there is experimental evidence suggesting that the electronic and vacancy (ionic) transport numbers are of similar magnitude [6, 7]. For $D_{\mathrm{vac}}/D_{\mathrm{eh}} > 1$ the self-consistent electric field slows down the vacancy diffusion.

Imagining a perturbation, ϵ, in the $\mathrm{V}^{2+}_{\mathrm{O}}$ defect formation energy at the alloy–oxide interface the reaction equilibrium constants at the interface are varied with respect to their value at the grain boundary, and oxide–gas surface. For a change of $\epsilon = 1\,\mathrm{eV}$ the Schottky equilibrium constant is modified by

$$\widetilde{G}^{f}_{\mathrm{V}^{2+}_{\mathrm{O}}} = G^{f}_{\mathrm{V}^{2+}_{\mathrm{O}}} + \epsilon \tag{3.106}$$

$$K^{I}_{\mathrm{S}} = \exp\left(-(3\widetilde{G}^{f}_{\mathrm{V}^{2+}_{\mathrm{O}}} + 2G^{f}_{\mathrm{V}^{3-}_{\mathrm{Al}}})/k_{\mathrm{B}}T\right) = K_{\mathrm{S}}\,\exp(-3\epsilon/k_{\mathrm{B}}T) \ll K_{\mathrm{S}} \tag{3.107}$$

and hence

$$\beta_I \approx 10^{-2}\beta_{\mathrm{GB}}. \tag{3.108}$$

Figure 3.22 shows the stresses for $D_{\mathrm{vac}}/D_{\mathrm{eh}} = 10$; in one simulation the equilibrium constant K_{S}^{I} is modified as described above, and in another simulation the electron-hole equilibrium constant throughout the interfaces and grain boundary is lowered, $K_{\mathrm{eh}} \times 10^{-2}$, with respect to the parameters described previously. The modified equilibrium constants lead to significantly lower stresses. Simulations for a modified Schottky equilibrium constant at all interfaces have also been carried out, the results indicate that the steady-state stress, $\boldsymbol{\sigma}^{\mathrm{st}}$, increases with a decreasing value of K_{S} for $K_{\mathrm{S}} = K_{\mathrm{S}}^{\mathrm{GB}} = K_{\mathrm{S}}^{I} = K_{\mathrm{S}}^{II}$.

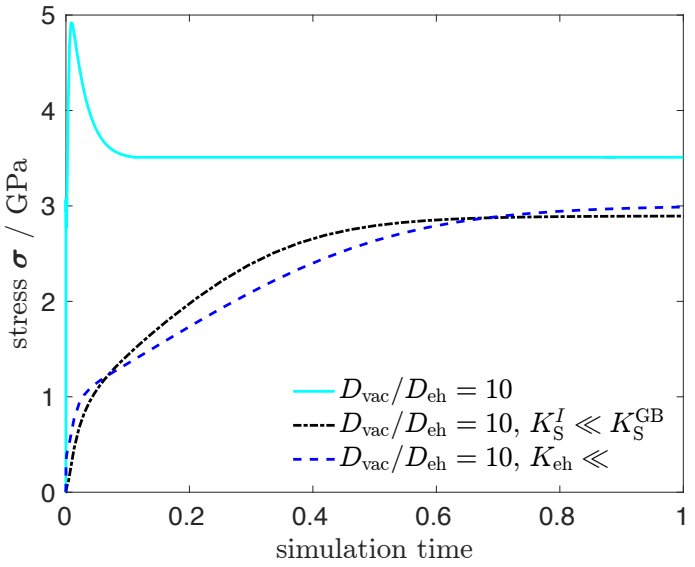

FIGURE 3.22: Evolution of the stress state at the grain boundary for modified equilibrium constants. The magnitude of stress converges to a steady-state value, constant as a function of time and position. The reduced electron-hole equilibrium constant $K_{\mathrm{eh}} \ll$ leads to a reduction in the amount of steady-state stress, similarly to the modified Schottky equilibrium constant, K_{S}^{I}, at the alloy–oxide interface.

Figure 3.23 shows the stresses for $D_{\mathrm{vac}}/D_{\mathrm{eh}} = 0.5$ under different scenarios. Again the lowered electron-hole equilibrium constant $K'_{\mathrm{eh}} = K_{\mathrm{eh}} \times 10^{-2}$ leads to a reduction in the amount of tensile stress. For a lower oxygen partial pressure applied at the surface (II) significantly less stress is induced, see figure 3.23.

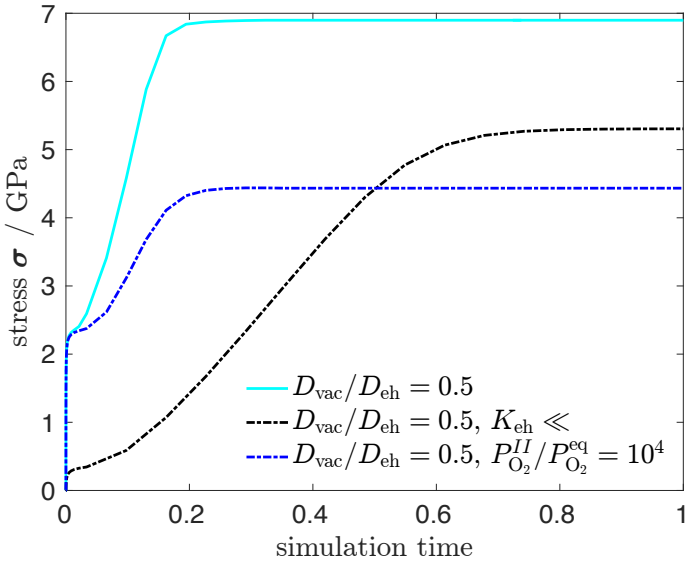

FIGURE 3.23: Evolution of the stress state at the grain boundary for a modified equilibrium constant, and a smaller oxygen partial pressure applied at the surface. The dashed blue line shows a simulation for $P^{II}_{O_2}/P^{eq}_{O_2} = 10^4$ while for the other two simulations plotted $P^{II}_{O_2}/P^{eq}_{O_2} = 10^8$. A smaller amount of partial pressure applied at the oxide–gas surface leads to significantly smaller tensile stresses. The reduced electron-hole equilibrium constant $K_{eh} \ll$ also leads to a reduction in the amount of steady-state stress.

3.5.6.3 The concentrations and chemical potential distributions

In the simulations the concentration distributions of the mobile species are obtained as a function of the position in the grain boundary and time, see figure 3.24 (a) for an example of a concentration distribution in stress-dependent calculations. Figure 3.24 shows the concentrations and dilute solution electrochemical potentials in the steady-state for a stress-dependent simulations. A significant deviation from local Schottky equilibrium is observed in figure 3.24 (b).

The dilute solution electrochemical potentials of the mobile species are defined by

$$\eta_s(r,t) = k_B T \ln\left(c_s(r,t)/c_s^0\right) + z_s e_0 \phi(r,t) \tag{3.109}$$

which was discussed in further detail in section 2.5. Schottky equilibrium is considered to hold locally if

$$\eta_{V_O^{2+}}(r)/2 = -\eta_{V_{Al}^{3-}}(r)/3 \tag{3.110}$$

and local electron-hole equilibrium holds if

$$-\eta_{\mathrm{e}}(r) = \eta_{\mathrm{h}}(r). \tag{3.111}$$

for all values of r within the grain boundary plane. For convenience the electrochemical potentials scaled by the charge of the particular species are shown in figure 3.24 (b). In this way the deviation from local ionic or electronic equilibrium becomes apparent readily, the quantities have the dimension of a voltage. The deviation from equilibrium is equivalent to plots of the scaled chemical potentials since the electrostatic potential, ϕ, difference cancels.

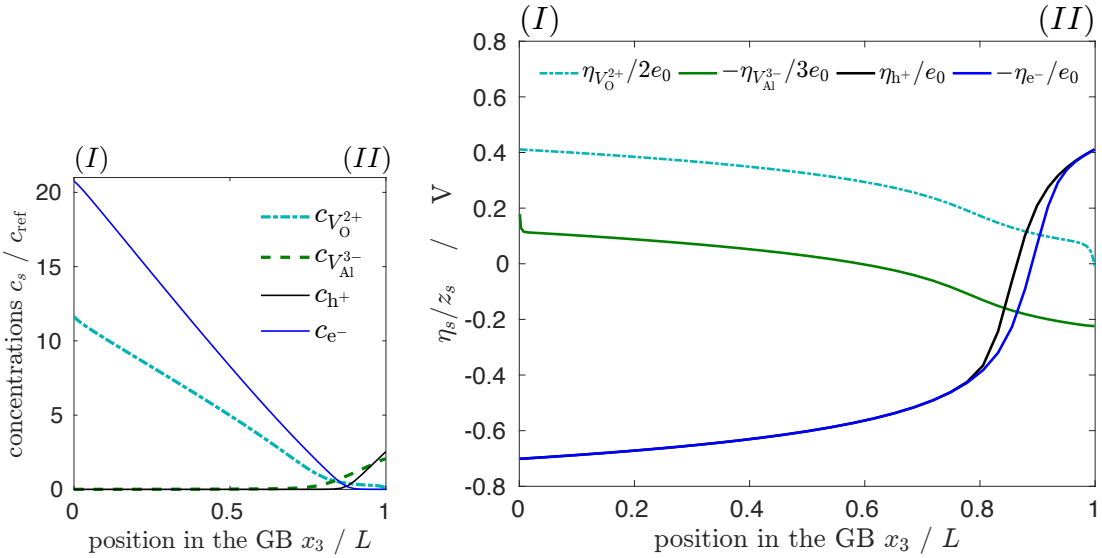

(a) (b)

FIGURE 3.24: (a) Steady-state concentrations of vacancies, electrons, and holes as a function of x_3 in the grain boundary plane, with fixed $x_1 = a_{\mathrm{hex}}/4$. Scaled units with $c_{\mathrm{ref}} = 10^{16}\,\mathrm{cm}^{-3}$ and $L = 1\,\mu$m. The diffusion coefficients are related by $D_{\mathrm{vac}}/D_{\mathrm{eh}} = 0.5$, and with $P^{II}_{\mathrm{O}_2}/P^{I}_{\mathrm{O}_2} = 10^{22}$. (b) The scaled electrochemical potentials, $\eta_s/z_s e_0$, calculated from the ideal solution chemical potentials, of the mobile species for fixed $x_1 = a_{\mathrm{hex}}/4$ in the grain boundary plane.

None of the electrochemical potential distributions is constant as a function of position in the steady-state. The magnitude of the deviation from Schottky equilibrium locally depends on the equilibrium constants, and the diffusion coefficients.

Figure 3.25 shows the distributions of the oxygen and aluminum chemical potentials calculated from the vacancy, electron, and hole concentrations. The internal oxygen chemical potential is calculated from the oxygen vacancy, $c_{\mathrm{V}_{\mathrm{O}}^{2+}}(r)$ and electron,

$c_e(r)$, concentrations by the dilute solution approximation

$$\mu_O(r) = -\left(\mu_{V_O^{2+}}(r) + 2\mu_e(r)\right) \quad \text{where} \quad \mu_s(r) = k_B T \ln\left(c_s(r)/c_s^0\right). \tag{3.112}$$

Analogously, the internal aluminum chemical potential is calculated from the aluminum vacancy and hole concentrations

$$\mu_{Al}(r) = -\left(\mu_{V_{Al}^{3-}}(r) + 3\mu_h(r)\right). \tag{3.113}$$

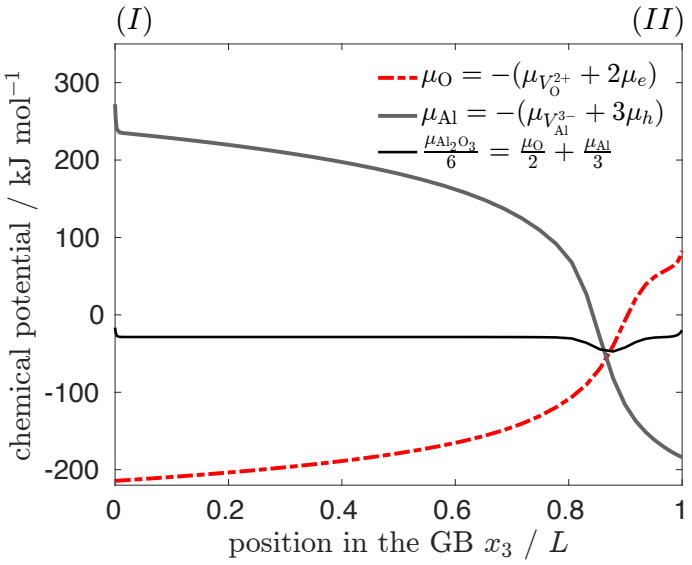

FIGURE 3.25: The internal aluminum and oxygen chemical potential, μ_{Al}, and μ_O, for fixed $x_1 = a_{hex}/4$ in the grain boundary plane.

3.5.6.4 The $p - n$ transition

The oxygen membrane permeation experiments by Kitaoka *et al.* [83] have shown the transition in the dominant ionic defect in the transport behaviour of α-Al_2O_3 as a function of the applied oxygen chemical potential difference, $\Delta\mu_{O_2}$. This has led to the hypothesis of a $p - n$ ionic transition within the alumina scale during high-temperature oxidation of aluminum containing alloys [70, 71].

In the developed model a transition between V_O^{2+} and V_{Al}^{3-} as the dominant defect in the defect fluxes in the grain boundary plane is observed. The character of the transition and its dependence on the reaction equilibrium constants and diffusion rates can be studied.

The essential variables for characterizing the $p-n$ transition are the species fluxes or current densities, and the transport numbers, the later are defined by

$$t_s = \frac{\sigma_s}{\sigma_{\mathrm{T}}}, \quad \text{and} \quad \sigma_s = \frac{D_s c_s z_s^2 e_0^2}{k_{\mathrm{B}} T} \tag{3.114}$$

where in the present simulations the total conductivity,

$$\sigma_{\mathrm{T}} = \sigma_{\mathrm{V}_{\mathrm{O}}^{2+}} + \sigma_{\mathrm{V}_{\mathrm{Al}}^{3-}} + \sigma_{\mathrm{h}} + \sigma_{\mathrm{e}}. \tag{3.115}$$

The transport numbers are dimensionless, adhere to $0 < t_s < 1$, and vary in the grain boundary plane since the mobile species concentrations change as a function of position, the diffusion coefficients are constants. Figure 3.26 shows the transport numbers in the steady-state as a function of the internal oxygen chemical potential; the vacancy diffusion coefficients, D_{vac}, are assumed to be larger than the electron-hole diffusion coefficient, D_{eh}. The parameters for the simulations shown in figures 3.26, 3.27, and 3.28 are those corresponding to the simulation with $\boldsymbol{\sigma}^{\mathrm{st}} = 5.3\,\mathrm{GPa}$, shown in figure 3.23 (black dashed line).

The vacancy transport number is defined by

$$t_{\mathrm{vac}} = t_{\mathrm{V}_{\mathrm{O}}^{2+}} + t_{\mathrm{V}_{\mathrm{Al}}^{3-}} \tag{3.116}$$

and the electron-hole transport number by

$$t_{\mathrm{eh}} = t_{\mathrm{e}} + t_{\mathrm{h}}. \tag{3.117}$$

The vacancy transport number is equal to the ionic transport number, $t_{\mathrm{vac}} = t_{\mathrm{ion}}$, since the vacancy and ionic conductivity are equal.

For any value of $t_s(r)$ as a function of position, r, can be assigned a value of $\mu_{\mathrm{O}}(r)$ determined from the concentrations, the resulting mapping is plotted in figure 3.26. A $p-n$ transition in the dominant vacancy species is predicted for the assumed parameters.

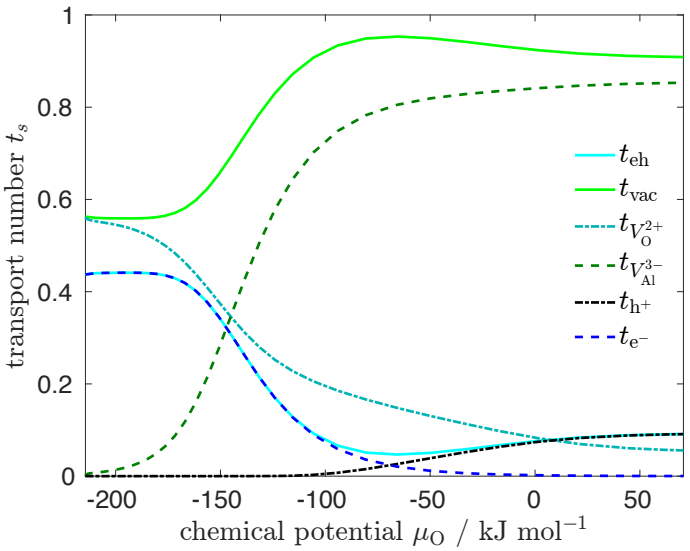

FIGURE 3.26: The steady-state (dimensionless and $0 < t_s < 1$) transport numbers as a function of the internal oxygen chemical potential μ_O. The diffusion coefficients in this simulation are related by $D_{vac}/D_{eh} = 0.5$. There is a $p - n$ transition in the dominant vacancy species in the vacancy transport number, t_{vac}, and a transition between electrons and holes as the dominant species in the electronic transport number, t_{eh}.

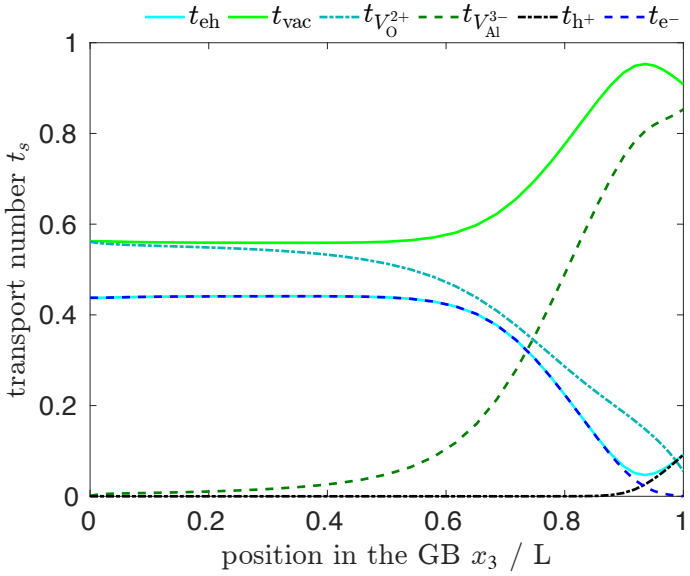

FIGURE 3.27: The steady-state (dimensionless and $0 < t_s < 1$) transport numbers as a function of the position in the grain boundary plane and averaged over the x_1 coordinate. The diffusion coefficients in this simulation are related by $D_{vac}/D_{eh} = 0.5$. There is a $p-n$ transition in the dominant vacancy species in the vacancy transport number, t_{vac}, and a transition between electrons and holes as the dominant species in the electronic transport number, t_{eh}.

Figure 3.28 shows a $p-n$ transition of the current densities in the grain boundary plane. In the steady-state the divergence of the vacancy current density which is given

by,

$$I_{\text{vac}} = 2e_0 J_{\text{V}_\text{O}^{2+}} - 3e_0 J_{\text{V}_\text{Al}^{3-}}, \tag{3.118}$$

vanishes $\nabla \cdot I_{\text{vac}} = 0$, and similarly the electron-hole current density,

$$I_{\text{eh}} = e_0 J_{\text{h}} - e_0 J_{\text{e}}, \tag{3.119}$$

adheres to $\nabla \cdot I_{\text{eh}} = 0$. The amount of charge transported by the vacancies is equal to the ionic current density, $I_{\text{vac}} = I_{\text{ion}}$.

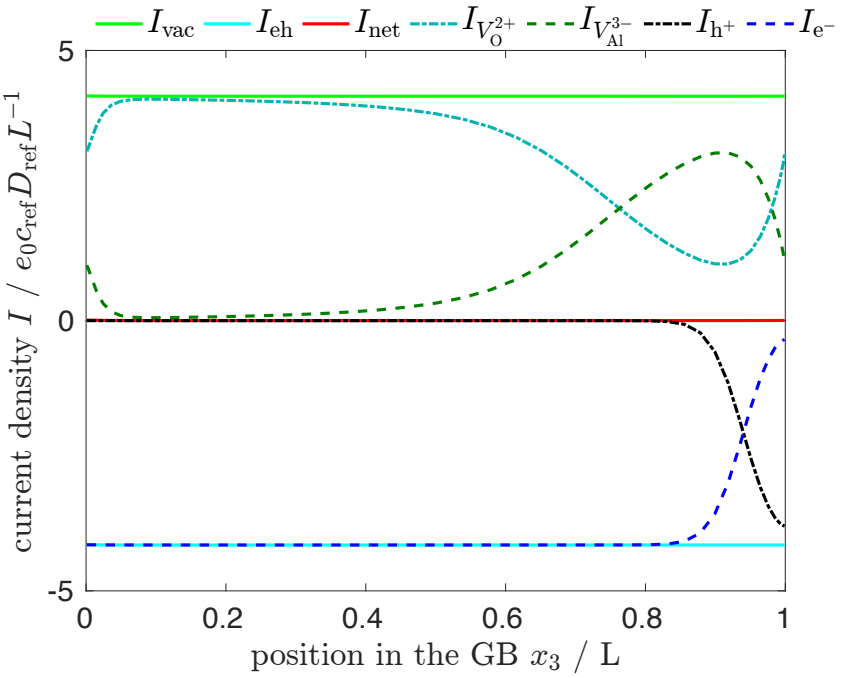

FIGURE 3.28: The steady-state current densities as a function of the position in the grain boundary plane and averaged over the x_1 coordinate. The diffusion coefficients in this simulation are related by $D_{\text{vac}}/D_{\text{eh}} = 0.5$. There is a $p-n$ transition in the dominant vacancy species in the vacancy current density, I_{vac}, and a transition between electrons and holes as the dominant species in the electronic current density, I_{eh}.

The transport numbers and hence the transition depends strongly on the values of the diffusion coefficients, and indeed for $D_{\text{vac}}/D_{\text{eh}} = 10$ no ionic $p-n$ transition is predicted, see figure 3.29. The vacancy diffusion coefficients are chosen larger than the electron and hole diffusion coefficients and for $D_{\text{V}_\text{O}^{2+}} = D_{\text{V}_\text{Al}^{3-}} = D_{\text{vac}}$ the oxygen vacancy dominates the transport regardless of the position in the grain boundary plane.

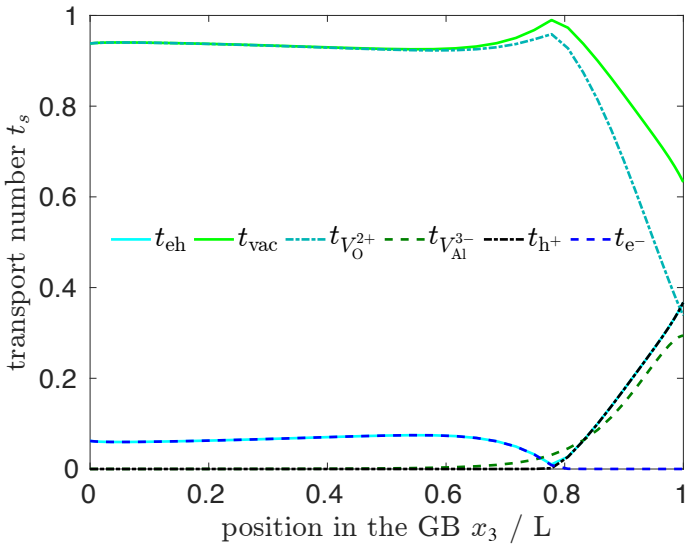

FIGURE 3.29: The steady-state (dimensionless and $0 < t_s < 1$) transport numbers as a function of the position in the grain boundary plane and averaged over the x_1 coordinate. The diffusion coefficients in this simulation are related by $D_{\mathrm{vac}}/D_{\mathrm{eh}} = 10$. There is no ionic $p - n$ transition.

3.5.7 Discussion

The experimental data of Balmain and Huntz [6, 7] regarding the electrical properties of polycrystalline α-Al_2O_3 scales has been described as the most reliable by Heuer [71]. For scales grown on β-NiAl at $T = 1100°\mathrm{C}$ with a thickness $\sim 2\,\mu$m the ionic transference number, $t_{\mathrm{ion}} = \sigma_{\mathrm{ion}}/(\sigma_{\mathrm{ion}} + \sigma_{\mathrm{e}})$, is analyzed and varies from about 0.6 at the alloy–oxide interface to about 0.1 at the oxide–gas interface, which is kept at an oxygen partial pressure of $P_{\mathrm{O}_2} = 10^5\,\mathrm{Pa}$ [6]. An intermediate minimum of t_{ion} occurs at about $P_{\mathrm{O}_2} = 10^{-5}\,\mathrm{Pa}$ which has been interpreted as evidence for a $p-n$ ionic transition by Heuer [71]. The addition of Yttrium to the alloy, NiAl(Y), is found to have little effect on the ionic transference number [6]. The analysis is based on the 'generalized Nernst-Einstein' relation that is closely related to the Wagner theory.

In order for the transport number $t_{\mathrm{vac}} \approx t_{\mathrm{eh}}$ the dominant vacancy and electronic species diffusion coefficients have to be of similar magnitude, $D_\nu \sim D_{\overline{\nu}}$, since the concentrations are related by approximate local charge neutrality. Therefore, in most simulations considered the chosen ratio $D_{\mathrm{vac}}/D_{\mathrm{eh}}$ does not depart significantly from 1. The electrons are found to be the dominant electronic species except near the oxide–gas surface. The $p - n$ transition is observed for e.g. $D_{\mathrm{vac}}/D_{\mathrm{eh}} = 0.5$, see figures 3.27 and 3.28, but not for e.g. $D_{\mathrm{vac}}/D_{\mathrm{eh}} = 10$, see figure 3.29. This is indicative of how sensitively the location of the $p - n$ transition depends on the diffusion coefficients, reaction rates, and oxygen partial pressure applied. However, it should be pointed out

that the stress generation does not require an internal $p-n$ ionic transition, simulations that do not show a pronounced transition do show steady-state stresses.

For the parameter configurations examined tensile stresses at the grain boundary are generated, confirming Atkinson's model and analytic considerations [2]. Also for varying the equilibrium constants at the alloy-oxide interface tensile stresses are observed. The stress state tends to a constant steady-state value in the model developed here, a spatial variation is not considered. The amount of stress in the steady-state is $\boldsymbol{\sigma}^{\mathrm{st}} \sim +5\,\mathrm{GPa}$ in most simulations considered. The stress $\boldsymbol{\sigma}^{\mathrm{st}}$ predicted is, thus, higher than the lateral growth stresses determined from most experiments. It depends strongly on the diffusion coefficients of the mobile species, the reaction rate constants, and on the oxygen partial pressure applied. The attainment of local Schottky equilibrium depends apart from the stress induced also on the relative rates of the reaction and the vacancy diffusion coefficients.

Apart from the sensitivity to the parameters used, another reason for stresses larger than in the experiments could be the neglect of a stress relaxation mechanism such as creep. Transport in a stress gradient, however, requires the relaxation of the assumption of a constant stress as a function of position.

A critical point in this model is the assumption that the Schottky reaction mechanism at the grain boundary proceeds in such way that as a Schottky vacancy complex annihilates oxide is removed at the grain boundary. This point is not entirely clear from the literature. While reference [183] assumes that oxide is removed as vacancies merge at the grain boundary, e.g. reference [70] seems to hold the opposite. If the later interpretation was right, the stresses predicted in this work would have the same magnitude, but their sign would be reversed. That is, a minus sign would appear in equation 3.95, and compressive stresses would be predicted.

Regarding the grain shape in the model, the amount of steady-state stress appears to be virtually independent of the aspect ratio a_{hex}/L.

Estimating the physical constants that enter into the stress expression derived previously

$$\boldsymbol{\sigma} = -2\frac{Y}{1-\nu}\frac{\Omega_{\mathrm{u}}}{a_{\mathrm{hex}}^2 L}\Delta N \tag{3.120}$$

the amount of oxide added or removed from the grain boundaries can estimated from the steady-state stress value determined in the simulations. The volume per formula unit of bulk oxide is given by $\Omega_{\mathrm{u}} = 4.128 \times 10^{-29}\,\mathrm{m}^{-3}$ at 1000° C, the hexagon side length $a_{\mathrm{hex}} = 1\,\mu\mathrm{m}$, $Y/(1-\nu) = 457\,\mathrm{GPa}$ (1400° C [128]), and the amount of oxide added or

removed is estimated from

$$\Delta N = \Delta N_{\text{sim}} f \left(2 \frac{Y}{1-\nu} \frac{\Omega_{\text{u}}^2}{a_{\text{hex}}^2 L} \right)^{-1} \tag{3.121}$$

where ΔN_{sim} is the amount of oxide added in the simulations, and f is a numeric constant in the simulations described in the previous section. The corresponding amount of oxide removed is about $\Delta N \approx -10^8$ oxide molecules per grain boundary plane for tensile stresses of about $5\,\text{GPa}$. This would mean on the order of $\sim 10^2$ layers of oxide are deleted at the grain boundaries until a steady-state is reached in which the creation and annihilation of vacancies at the grain boundary are balanced such that no further oxide is added or removed.

In conclusion, a model has been introduced capable of predicting the amount of stress induced in an idealized grain structure at conditions of high-temperature steady-state oxide scale growth. The model gives insight into the microscopic processes underpinning the transport during oxidation.

By comparison to experimental data it is reasoned that the diffusion coefficients of the dominant species could be of similar magnitude. The details of the defect transport mechanisms are still under debate [69, 71]. Thus, further work would be of value to determine the electron and ion transport mechanism in alumina grain boundaries, and particularly *ab initio* simulations along the lines of the work by Guhl *et al.* [56] are expected to benefit the understanding of the transport mechanism. That is, a detailed characterization of the localized and near band edge states at the grain boundary, as mentioned in chapter 2 section 2.5, and inclusion of their properties in a realistic model of the electron and ion grain boundary transport, see also the discussions by Heuer [69, 71].

The predicted amount of stress depends sensitively on a number of parameters and this might help to explain the discrepancies between the lateral growth stress values determined from the experimental measurements. Many experiments do indicate compressive lateral growth stresses, which could indicate the presence of an interstitial transport mechanism. Further work is required to determine if compressive stress does necessarily imply interstitial transport or if indeed vacancy diffusion can also lead to compressive stresses at the grain boundaries. Furthermore, a position dependence in the stress distribution within growing scales has been observed experimentally. The model could be extended by including a stress relaxation mechanism, such as transport in a stress gradient, and thereby take into account spatially varying stress distributions.

Chapter 4

Drift-diffusion limited scale growth or membrane permeation

4.1 Introduction

Metal oxidation and scale growth are complex phenomena and perhaps surprisingly, it is possible to explain the experimentally observed behaviour in many cases by simple analytical rate laws derived from elementary physical models. For micrometer thin scales growing at high-temperatures in a gaseous environment Wagner's theory [2, 189] is usually adopted to interpret experimental data. Due to its elegant thermodynamic formulation this theory is still influential today, and used in essentially unchanged form. Wagner [189] showed that the *drift-diffusion* transport of anions, cations, and electrons which limits the overall oxidation rate does yield a square root law time dependence for the film thickness

$$L \sim \sqrt{t}. \tag{4.1}$$

This is a remarkable result given that a square root time dependence is typically the hallmark of purely diffusive behaviour. This is reflected in the relation between the mean-square fluctuation in particle position as a function of time during Brownian motion

$$\langle (\Delta r)^2 \rangle \sim t \tag{4.2}$$

and the well known similarity solution of the Fickian diffusion equation by means of the auxiliary variable $\xi \sim x/\sqrt{t}$. It is shown here that Wagner's rate equation only yields a square root time dependence for the film thickness (parabolic law) in the limit of a

vanishing local charge density. In particular, for thin films and low defect concentrations the local charge neutrality approximation breaks down and a linear rate law, $L \sim t$, is predicted for these conditions.

Since it was originally derived for homogeneous scales, *i.e.* no grain boundaries or dislocations, the application of Wagner's theory to oxides such as alumina and chromia requires a modification. Grain boundary transport dominates in these oxides and the mobile species diffusion coefficients are replaced by Hart's expression for an effective diffusivity, see chapter 2 section 2.4. Grain boundaries in growing oxide films are known as sources and sinks of point defects, and the creation or annihilation of oxide within the film generates stress, as has been discussed in chapter 3 section 3.5. The induced stress causes a deviation from local ionic equilibrium and this deviation requires a further modification of Wagner's theory of metal oxidation which is discussed in this chapter.

The chapter is organized as follows. In section 4.2, the assumptions of local charge neutrality, and the application of the Gibbs-Duhem relation in the context of the Wagner theory are discussed. To obtain a closed form solution and growth rate formula Wagner's rate equation is typically solved by adopting the local charge neutrality assumption, which does limit the applicability of the theory significantly. It has been claimed in the literature on metal oxidation [47] that Wagner's theory is inconsistent with the non-equilibrium equivalent of the Gibbs-Duhem relation. It is argued here that the apparent contradiction is due to a misapplication of the Gibbs-Duhem relation.
In section 4.2.1, the oxidation rate formula is derived from an electric equivalence circuit model. It brings to light the essentials of the Wagner theory in a physically intuitive manner, and could serve as an educational device on this theory.
In section 4.3, the failure and consequences of the assumption of local ionic equilibrium are discussed. It is argued that the assumption of local ionic equilibrium is only justifiable in the presence of extended defects in the scale, and even if those are present the assumption is still prone to fail.

In section 4.3, an attempt is made for a systematic treatment of the charge neutrality approximation applied to Wagner's theory. Following the identification in sections 4.2.3 and 4.2.4 of the dimensionless ratio of the reference Debye length over the film thickness denoted by $\kappa = \ell_{\mathrm{D}}/L$ as the chief parameter governing the behaviour of the equations under consideration, a singular perturbation theory approach is adopted with perturbation parameter κ. Significantly, the novel treatment yields a prediction of a transition between a linear to square root time dependence of the scale growth rate for thin scales, see section 4.3.3. It is argued that a linear growth regime for thin films

precedes the square root (parabolic) law that is obtained from the Wagner theory by adopting the charge neutrality approximation.

4.2 A critical discussion of the Wagner theory

The scale growth rate of a $\mathrm{M}_{|z_\mathrm{X}|}\mathrm{X}_{|z_\mathrm{M}|}$ compound limited by the transport through the scale is proportional to the amount of oxidant reaching the metal–scale interface plus the amount of metal reaching the metal–oxidant interface per unit time. For constant fluxes a convenient formulation of the growth rate expression in the Wagner theory [2, 189] of metal oxidation is given by

$$\frac{dL}{dt} = \frac{\Omega_\mathrm{u}}{e_0|z_\mathrm{X} z_\mathrm{M}|} I_\mathrm{ion} \tag{4.3}$$

where L is the thickness of the scale, Ω_u is the volume per formula unit of scale; e_0 is the positive elementary charge; $I_\mathrm{ion} = e_0 z_\mathrm{X} J_\mathrm{X} + e_0 z_\mathrm{M} J_\mathrm{M}$ is the ionic flux with J_X and J_M the oxidant and metal fluxes, respectively; and with the convention of positive fluxes in the positive x_3 direction towards the scale–environment interface, and for $x_3 = 0$ at the metal–scale interface.

In this formulation it is immediately apparent that the growth rate vanishes unless the ionic current density is balanced by an electronic current density, since from $I_\mathrm{el} = 0$ would follow that $I_\mathrm{ion} = 0$ has to hold to satisfy the constraint of zero net current in the steady-state,

$$I_\mathrm{el} + I_\mathrm{ion} = 0. \tag{4.4}$$

The rate equation, generalized with respect to equation 2.10 introduced in chapter 2 to include hole transport, is written as

$$\frac{dL}{dt} = \frac{\Omega_\mathrm{u}}{e_0|z_\mathrm{X} z_\mathrm{M}|L} \int_I^{II} \frac{(\sigma_\mathrm{X} + \sigma_\mathrm{M})(\sigma_\mathrm{e} + \sigma_\mathrm{h})}{\sigma_\mathrm{X} + \sigma_\mathrm{M} + \sigma_\mathrm{e} + \sigma_\mathrm{h}} \, d\mu_\mathrm{X}. \tag{4.5}$$

A steady-state is assumed to be reached during growth described by Wagner's theory of metal oxidation requiring that the concentrations of the mobile species and fluxes throughout the scale reach a stationary value during growth. In this steady-state the current carried by ions and electrons is balanced such that there is no build-up or depletion of charge locally; a self-consistent electric field influences the species fluxes such that the net current vanishes at any point. It has been argued in the literature that the

self-consistent electric field in the Wagner theory is inconsistent with the Gibbs-Duhem equation [19, 20, 47], a problem which we address in section 4.2.2.

In the Wagner theory it is further assumed that the diffusing cations and anions are in equilibrium at the metal-oxide and oxide-gas interfaces, and indeed throughout the growing scale. In a vacancy mediated transport mechanism this assumption translates to Schottky equilibrium prevailing throughout the scale including its surface and interfaces. This ionic equilibrium requires the mobile ions to react internally and hence the formation and dissolution of oxide within the scale, which of course can only occur at dislocations and grain boundaries. The derivation of the Wagner theory, however, requires constant fluxes, $\nabla \cdot J_s = 0$, which cannot be satisfied if the ions are also reacting. The 'internal oxidation' would further induce stresses which would in turn modify the fluxes. In materials with cation and anion counter diffusion the assumption of internal ionic equilibrium therefore has to be examined, and it is discussed here in section 4.3.

4.2.1 An electric circuit equivalence system

The rate equation obtained by Wagner [189] can be derived in different ways. Here I propose a derivation by recourse to an electric circuit equivalence system. The reasons to promote this derivation are twofold: First, the simple circuit model provides a physically intuitive derivation. Second, the special combination of the transport coefficients in the integrand of the rate equation integral, see equation 4.5, is exposed as precisely the combination expected from the basic circuit rules of conductors (resistors) in series or parallel.

As a first step, the homogeneous film is mapped onto a conductor network, see figure 4.1, and the aim is to calculate the ionic currents through this partitioned film.

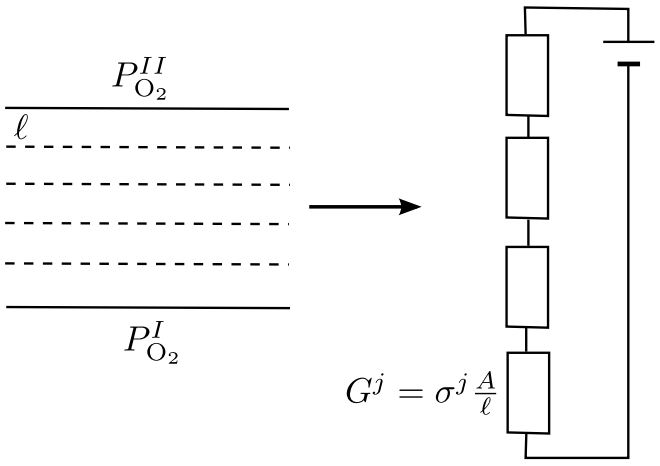

FIGURE 4.1: The film is imagined to be composed of layers with thickness ℓ. A conductance G^j is assigned to every layer and the film is mapped onto a conductor network (resistance and conductance are related by $G^j = 1/R^j$). The oxidant chemical potential difference between the surfaces induces a voltage in the conductor network.

4.2.1.1 An equivalence network of conductors

The equivalence network consists of conductors in parallel (resistors in series), the conductance of each element is due to the conductivity of the mobile species present and is a measure for how easily charge flows through each layer. The driving force is determined by the oxidant chemical potential difference between the interfaces (I) and (II),

$$\Delta\mu_{O_2} = \mu^{II}_{O_2} - \mu^{I}_{O_2}. \tag{4.6}$$

At the interfaces equilibrium between the oxidant ions and atoms, and the electrons is assumed to hold

$$\frac{1}{2}O_2 + 2e \rightleftharpoons O^{2-} \tag{4.7}$$

$$\frac{1}{2}\mu_{O_2} + 2\mu_e = \mu_{O^{2-}}. \tag{4.8}$$

In the steady-state the voltages across the conductances are distributed in such way as to minimize the energy dissipation. The Kirchhoff current law ascertains that the net current through the j-th equivalence conductor is zero for all j

$$A\sum_s I^j_s = \sum_s G^j_s V_{s,j} = 0, \tag{4.9}$$

where $V_{s,j}$ denotes the electrochemical potential difference of species s across the j-th conductor divided by the corresponding charge number, $\Delta\eta_s/z_s e_0$, it has the dimensions of a voltage; the current density I_s^j has the dimensions of unit charge per unit area, A, and time. There is no change in the local charge density in the steady-state, the currents of the different species s compensate each other. $V_{s,j}$ can also be written as

$$V_{s,j} = \frac{\Delta\eta_s^j}{z_s e_0} = \frac{\Delta\mu_s^j}{z_s e_0} + \Delta\phi^j. \tag{4.10}$$

If the oxidant ions and electrons are the mobile species, due to the Kirchhoff current law, the electrostatic potential difference across the j-th equivalence conductor is given by

$$\Delta\phi^j = -\frac{1}{G^j_{\mathrm{O}^{2-}} + G^j_{\mathrm{e}}} \left(G^j_{\mathrm{O}^{2-}} \frac{\Delta\mu^j_{\mathrm{O}^{2-}}}{z_{\mathrm{O}} e_0} + G^j_{\mathrm{e}} \frac{\Delta\mu_{\mathrm{e}}}{z_{\mathrm{e}} e_0} \right) \tag{4.11}$$

By using the above expression for $\Delta\phi^j$ the current of oxidant ions through the j-th equivalence conductor can be rewritten as

$$I^j_{\mathrm{O}^{2-}} = \frac{G^j_{\mathrm{O}^{2-}} G^j_{\mathrm{e}}}{G^j_{\mathrm{O}^{2-}} + G^j_{\mathrm{e}}} \left(\frac{\Delta\mu^j_{\mathrm{O}^{2-}}}{z_{\mathrm{O}} e_0} - \frac{\Delta\mu^j_{\mathrm{e}}}{z_{\mathrm{e}} e_0} \right) \frac{1}{A}. \tag{4.12}$$

The chemical or electrochemical potential difference divided by the charge,

$$\frac{\Delta\mu^j_{\mathrm{O}^{2-}}}{z_{\mathrm{O}} e_0} - \frac{\Delta\mu^j_{\mathrm{e}}}{z_{\mathrm{e}} e_0} = \frac{\Delta\eta^j_{\mathrm{O}^{2-}} - |z_{\mathrm{O}}|\Delta\eta^j_{\mathrm{e}}}{z_{\mathrm{O}} e_0} \equiv \Delta V_{\mathrm{O}}^{j,j-1} \tag{4.13}$$

is denoted here by, $\Delta V_{\mathrm{O}}^{j,j-1}$. It has the physical dimensions of a voltage and the meaning equivalent to a voltage across the j-th conductor, see figure 4.2. $\Delta V_{\mathrm{O}}^{j,j-1}$ is not due to an electrostatic potential difference or difference in the Fermi level, but is a thermodynamic driving force due to chemical potential gradients.

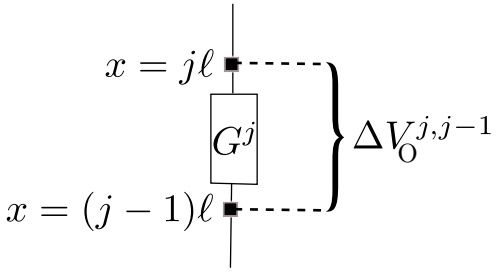

FIGURE 4.2: The equivalence voltage due to the chemical potential differences $\Delta V_{\mathrm{O}}^{j,j-1}$.

In the steady-state the current through all conductances is equal and the following identity holds

$$I_{\mathrm{O}^{2-}} = \frac{1}{L}\sum_{j=1}^{N}\frac{\ell}{A}\frac{G^j_{\mathrm{O}^{2-}}G^j_{\mathrm{e}}}{G^j_{\mathrm{O}^{2-}}+G^j_{\mathrm{e}}}\Delta V_{\mathrm{O}}^{j,j-1} \tag{4.14}$$

where $N\ell = L$, and ℓ is the length of the conductors. The conductance, G^j_s, and conductivity, σ_s, of species s in the j-th conductor is given by

$$G^j_s = \frac{A}{\ell}\,\sigma_s\Big|_{V_{\mathrm{O}}(x)\in[V_{\mathrm{O}}(j\ell),V_{\mathrm{O}}((j-1)\ell)]} \tag{4.15}$$

In the continuum limit, where $\ell \to 0$ while $N\ell = L$ is fixed, the oxidant ion current is given by

$$I_{\mathrm{O}^{2-}} = \frac{1}{L}\lim_{\ell\to 0}\sum_{j=1}^{N}\left(\frac{\sigma_{\mathrm{O}^{2-}}\sigma_{\mathrm{e}}}{\sigma_{\mathrm{O}^{2-}}+\sigma_{\mathrm{e}}}\right)_{V_{\mathrm{O}}(x)\in[V_{\mathrm{O}}(j\ell),V_{\mathrm{O}}((j-1)\ell)]}\Big(V_{\mathrm{O}}(j\,\ell)-V_{\mathrm{O}}((j-1)\ell)\Big) \tag{4.16}$$

which is a Riemann-Stieltjes integral,

$$I_{\mathrm{O}^{2-}} = \frac{1}{L}\int_0^L\left(\frac{\sigma_{\mathrm{O}^{2-}}\sigma_{\mathrm{e}}}{\sigma_{\mathrm{O}^{2-}}+\sigma_{\mathrm{e}}}\right)_x dV_{\mathrm{O}}(x). \tag{4.17}$$

Applying the above expression in the formulation of the growth rate given in equation 4.3, the growth rate as predicted by the Wagner theory in the case of two mobile species O^{2-} and e follows. For the general case of mobile cations, M^{2+}, and holes, h, in addition to anions and electrons the equivalence conductance is modified as shown in the next section.

4.2.1.2 The equivalence conductance

For anions, O^{2-}, and electrons, e, as the mobile species the equivalent conductance corresponds to two conductances in parallel (resistors in series)

$$G_{\text{equiv}} = \left(\frac{1}{G_{\mathrm{O}^{2-}}}+\frac{1}{G_{\mathrm{e}}}\right)^{-1} = \frac{G_{\mathrm{O}^{2-}}G_{\mathrm{e}}}{G_{\mathrm{O}^{2-}}+G_{\mathrm{e}}} \tag{4.18}$$

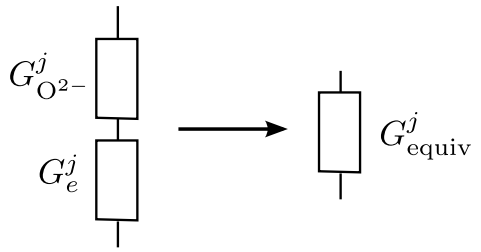

FIGURE 4.3: Effective conductance with two mobile species.

If the metal ion, M^{2+}, is mobile as well and if local ionic equilibrium holds, the two 'ionic conductances' are in series (resistors in parallel)

$$G_{\mathrm{ion}} = G_{\mathrm{O}^{2-}} + G_{\mathrm{M}^{2+}}, \tag{4.19}$$

and similarly for electron-hole equilibrium

$$G_{\mathrm{el}} = G_{\mathrm{e}} + G_{\mathrm{h}}. \tag{4.20}$$

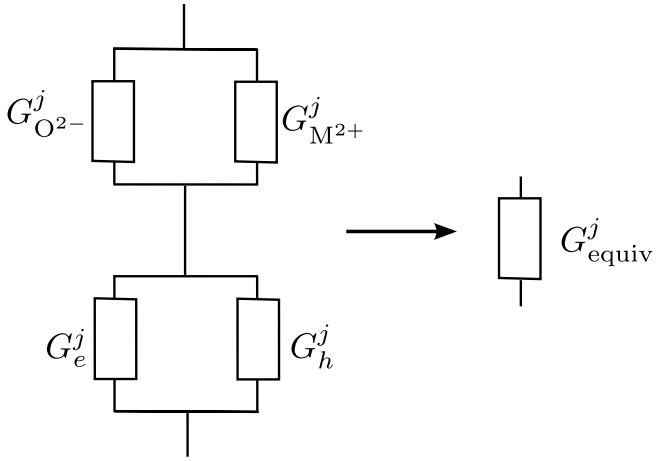

FIGURE 4.4: Effective conductance with four mobile species and ionic, and electron-hole equilibrium.

The corresponding equivalent conductance is given by the ionic and electronic conductance in parallel (resistance in series)

$$G_{\mathrm{equiv}} = \left(\frac{1}{G_{\mathrm{ion}}} + \frac{1}{G_{\mathrm{el}}}\right)^{-1} = \frac{(G_{\mathrm{O}^{2-}} + G_{\mathrm{M}^{2+}})(G_{\mathrm{e}} + G_{\mathrm{h}})}{G_{\mathrm{O}^{2-}} + G_{\mathrm{M}^{2+}} + G_{\mathrm{e}} + G_{\mathrm{h}}} \tag{4.21}$$

and the ionic current is given by

$$I_{\text{ion}} = \frac{1}{L}\int_0^L \left(\frac{(\sigma_{\text{O}^{2-}} + \sigma_{\text{M}^{2+}})\,(\sigma_{\text{e}} + \sigma_{\text{h}})}{\sigma_{\text{O}^{2-}} + \sigma_{\text{M}^{2+}} + \sigma_{\text{e}} + \sigma_{\text{h}}} \right)_x dV_{\text{O}}(x). \tag{4.22}$$

The ionic current determines the oxidation rate as expressed by equation 4.3. The circuit equivalence model, thus, yields the same ionic current and oxidation rate as the one derived within the Wagner theory of metal oxidation, see equation 4.5.

4.2.2 The application of the Gibbs-Duhem equation

A thermodynamic system describing a physical system under consideration is defined by a complete set of macroscopic variables, which are either extensive (scale with the system size) or intensive (independent of the system size) [55]. The fundamental thermodynamic relation in the energy representation [15] is given by

$$dU(X_i) = \sum_i \frac{\partial U}{\partial X_i} dX_i \tag{4.23}$$

where the X_i are extensive variables and the $Y_i = \partial U/\partial X_i$ are intensive. Adding identical small systems next to each other the extensive quantities scale with the total system size while the intensive quantities remain constant, thereby an integration of the fundamental relation is performed. Formally this is expressed by introducing the scaling parameter Λ. The energy is additive for combinations of two or more independent subsystems and, therefore, an extensive quantity, meaning it satisfies the scaling law

$$U(\Lambda X_i) = \Lambda\, U(X_i) \tag{4.24}$$

with the scaling parameter Λ. By a theorem of Euler for homogeneous functions of degree 1,

$$U(X_i) = \sum_i Y_i X_i \tag{4.25}$$

and by examining the total differential, dU, and comparing to relation 4.23 the Gibbs-Duhem relation follows

$$\sum_i X_i dY_i = 0. \tag{4.26}$$

This means the intensive variables are not all mutually independent.

In the local equilibrium hypothesis the thermodynamic state functions and their functional forms are assumed to hold for any 'local equilibrium cell' of the system, thereby extending the state functions to be continuous functions of space and time. It is common practice in the literature on irreversible thermodynamics to assume a pointwise form of the Gibbs-Duhem equation in space and thereby to relate the gradients of the chemical potentials [28, 92, 146]. Fromhold [47] applies a local form of the Gibbs-Duhem equation under isothermal conditions including the electric field, $-\nabla\phi$, for a 1D system

$$\sum_s c_s(x)\ \nabla\eta_s(x) = \sum_s c_s(x)\ \nabla\mu_s(x) + \rho(x)\ \nabla\phi(x) = 0, \tag{4.27}$$

and argues that the resulting constraint on the electric field is inconsistent with the Wagner theory of metal oxidation [47]. This claim has also been the subject of more recent publications [19, 20]. Fromhold argues that the field calculated from the zero net current assumption,

$$-\nabla\phi = \frac{k_{\mathrm{B}}T\sum_s D_s z_s \nabla c_s}{\sum_s D_s c_s z_s^2}, \tag{4.28}$$

and the electric field calculated from the Gibbs-Duhem equation,

$$-\nabla\phi = \frac{k_{\mathrm{B}}T\sum_s \nabla c_s}{\sum_s z_s c_s}, \tag{4.29}$$

are inconsistent [47]. However, the Gibbs-Duhem equation is a consequence of the extensivity of thermodynamic systems and for systems with non vanishing local charge density, $\rho(r)$, it is not applicable since such systems are not extensive. The electric field has to be calculated from the Maxwell equations. The only way for the electrostatic potential, to change is a variation in the local charge density and it can therefore not be varied independently without violating self-consistency. The electric field arises because the transport between the local equilibrium cells is not in stoichiometric proportions during a transient period that precedes the steady-state limit.

The Gibbs-Duhem relations holds if the Gibbs energy is a homogeneous function of first order in its extensive variables. In most physical systems additivity is a necessary condition for extensivity [179]. Within the local equilibrium hypothesis the non-equilibrium system is partitioned into local equilibrium cells. For such a thermodynamic system with non-vanishing local charge density and long-range Coulomb interactions it can be expected that neither additivity nor extensivity hold for the local Gibbs

energy. The local version of the Gibbs-Duhem equation is therefore not applicable.

Wagner applies the Gibbs-Duhem equation to relate the metal and oxidant ion chemical potentials in the limit of approximate local charge neutrality, *i.e.* without an electrostatic potential term; the treatment is further discussed in section 4.3.1.

4.2.3 The steady-state assumption

The steady-state assumption

$$\partial_t c_s = 0 \text{ and } \nabla \cdot J_s = 0 \tag{4.30}$$

ascertains that the concentrations do not change with time and that the fluxes are constant as a function of the position in the film. From this definition of the steady-state it is not immediately obvious why the assumptions of zero net current locally

$$\sum_s I_s = 0 \tag{4.31}$$

should only hold in the steady-state limit. However, the assumption of zero net current follows directly from the Maxwell-Ampere equation

$$\frac{1}{\mu_0}\nabla \times B = \sum_s I_s + \varepsilon_r \varepsilon_0 \partial_t E \tag{4.32}$$

which in the Coulomb gauge, $\nabla \cdot \mathscr{A} = 0$, and with the electric field,

$$E = -\nabla\phi + \partial_t \mathscr{A}, \tag{4.33}$$

is rewritten as

$$\Box\mathscr{A} = \sum_s I_s - \varepsilon_r \varepsilon_0 \partial_t \nabla\phi \tag{4.34}$$

where $\mathscr{A}$ is the magnetic vector potential, and $\Box$ is the d'Alembertian. $\Box\mathscr{A}$ corresponds to radiation effects and is not discussed here. For $\Box\mathscr{A} \equiv 0$ and with the Nernst-Planck flux the equation is rewritten as

$$\varepsilon_r \varepsilon_0 \partial_t \nabla\phi = \sum_s I_s \tag{4.35}$$

or

$$\frac{\varepsilon_r \varepsilon_0}{\sigma_{\mathrm{T}}} \partial_t \nabla\phi + \nabla\phi = -\sum_s t_s \frac{\nabla \mu_s}{z_s} \tag{4.36}$$

where σ_{T} is the total conductivity, and $\tau_{\mathrm{r}} = \varepsilon_r \varepsilon_0 / \sigma_{\mathrm{T}}$ is identified as the dielectric relaxation time, characterizing the time scale of changes in the local charge density.

The equation in dimensionless form reads as

$$\sum_s I_s - \kappa^2 \partial_t \nabla\phi = 0 \tag{4.37}$$

where

$$\kappa = \frac{\ell_{\mathrm{D}}}{L}. \tag{4.38}$$

For rapid changes in ϕ the term $\kappa^2 \partial_t \nabla\phi$, which is small since κ is typically small does not vanish; there is build-up and depletion of local charge density. The characteristic time scale for diffusion is given by

$$\tau_{\mathrm{d}} = L^2 / D_{\text{ref}} \tag{4.39}$$

and since

$$\frac{\tau_{\mathrm{r}}}{\tau_{\mathrm{d}}} \sim \left(\frac{\ell_{\mathrm{D}}}{L} \right)^2 \tag{4.40}$$

the time scale τ_{r} for variations in ϕ compared to to the time scale τ_{d} of attainment of the steady-state effectively varies as

$$\kappa^2 \sim \frac{1}{L^2 \sum_s z_s^2 c_s^{\text{surf}}} \tag{4.41}$$

where c_s^{surf} is the concentration of species s on the surface. For large thicknesses $L \gg \ell_{\mathrm{D}}$ and or large defect concentrations it can therefore be expected that in the steady-state the zero net current assumption applies at any position

$$\sum_s I_s = 0. \tag{4.42}$$

It is generally a very reliable assumption in the context of the Wagner theory.

Capturing the time dependent behaviour in this way is of course equivalent to

solving the Poisson equation self-consistently with the continuity equation, the divergence of the Maxwell-Ampere equation leads to the continuity equation under application of the Poisson equation. The coupled system of equations is a singular perturbation problem, with singular perturbation parameter κ^2, a perspective further discussed in section 4.3.2.

4.2.4 The local charge neutrality approximation

Overall charge neutrality of the system is maintained during the evolution of the concentrations. However, charge can be displaced within the system, allowing for the generation of a non vanishing local charge density, while adhering to the fundamental principle of charge conservation at any moment.

The local charge neutrality assumption

$$\rho(r) = 0 \tag{4.43}$$

is frequently applied in the Wagner theory to relate the mobile species concentrations and to derive closed form solutions for the fluxes and electric field. The validity of this assumption depends strongly on the screening parameter

$$\kappa = \lambda_{\mathrm{D}}/L, \tag{4.44}$$

the magnitude of the local charge density decreases as κ becomes smaller, which in particular varies as

$$\kappa \sim \frac{1}{\sqrt{\sum_s z_s^2 c_s^{\mathrm{surf}}}} \tag{4.45}$$

where c_s^{surf} is the concentration of species s on the surface.

There seems to be a paradox contained in the analytical closed form equations frequently derived from the Wagner theory or similar approaches: The equations for the fluxes, permeation rate, electrostatic potential difference across the film etc. are derived by applying the zero local charge density approximation, $\rho(r) = 0$. While these solutions seem consistent with the more general simulation results, it seems paradoxical to derive equations containing electric field effects while assuming $\rho = 0$ throughout the domain.

An immediate remedy might be to consider the charge to be confined to the surface or

interface with equal and opposite surface charges similarly to a parallel plate capacitor. However, this hypothesis immediately leads to difficulties since the electrostatic potential difference is generally expected to converge to a constant in the limit of large thicknesses $L(t)$ and the capacitor potential difference,

$$\Delta\phi = \frac{\gamma}{\varepsilon_r \varepsilon_0} L(t) \rightarrow \text{const.} \tag{4.46}$$

then seems to indicate that the surface charge, γ, varies as $\gamma \sim L(t)^{-1}$. This means that the surface concentrations cannot be stationary during growth, seemingly contradicting the steady-state and the zero net current assumptions.

The approach described in section 4.3.2 is an attempt to resolve this apparent paradox in the derivations.

4.3 Beyond the Wagner theory

It has been argued and shown in chapter 3 section 3.5 that the assumption of internal ionic equilibrium within a growing scale does not hold in general. Here I propose a simple modification to the rate equation for monocrystalline scales or membranes. For the general case of transport through scales or membranes with extended defects, and internal oxidation inducing stress generation no analytic model is available at present. Section 4.3.1 gives a discussion of the Wagner theory taking into account the findings from the simulations with the hexagonal cell model in chapter 3 section 3.5.6.

Typically the local charge neutrality approximation is adopted to derive a closed form solution from the oxidation rate equation 4.5. The departure from local charge neutrality or 'Debye-Hückel disorder' has been identified as early as 1946 by Bardeen [8] as an aspect of the theory that could require modifications of the rate equations. The local charge neutrality approximation and the related 'space charge' phenomenon have been investigated extensively by Fromhold [49] in the context of scale growth. In section 4.3.2 I propose a method of systematic improvement upon the local charge neutrality approximation. The treatment was developed independently from Fromhold's derivations, by adapting a technique from the mathematical literature on semiconductors [112]. It has been noted in the literature, e.g. [47], that Wagner's rate formula does not necessarily yield a square root (parabolic) growth rate, the latter only follows if the integral in equation 4.5 is constant. In section 4.3.3 a linear regime, preceding the square root law regime, is predicted within the framework of Wagner's oxidation rate theory. The linear regime is derived by relaxing the local charge neutrality approximation.

4.3.1 Internal ionic equilibrium

Wagner [189] assumed the chemical potentials of the ions and atoms are in equilibrium at any point in the scale

$$\mu_{\mathrm{X}}^{z} = \mu_{\mathrm{X}} + |z_{\mathrm{X}}|\mu_{\mathrm{e}} \tag{4.47}$$

$$\mu_{\mathrm{M}}^{z} + |z_{\mathrm{M}}|\mu_{\mathrm{e}} = \mu_{\mathrm{M}}, \tag{4.48}$$

and that the chemical potentials of the neutral atoms are related by[1]

$$N_{\mathrm{X}} d\mu_{\mathrm{X}} + N_{\mathrm{M}} d\mu_{\mathrm{M}} = 0. \tag{4.49}$$

Further, for small deviations from stoichiometry, $N_{\mathrm{X}}/N_{\mathrm{M}} \simeq |z_{\mathrm{M}}/z_{\mathrm{X}}|$,

$$\nabla\mu_{\mathrm{X}} \simeq -\left|\frac{z_{\mathrm{X}}}{z_{\mathrm{M}}}\right| \nabla\mu_{\mathrm{M}}. \tag{4.50}$$

The immediate consequence of this relation is the characteristic form of the transport coefficient in Wagner's oxidation rate formula

$$\sigma_{\mathrm{X}} t_{\mathrm{el}} \frac{\nabla\mu_{\mathrm{X}}}{z_{\mathrm{X}}} + \sigma_{\mathrm{M}} t_{\mathrm{el}} \frac{\nabla\mu_{\mathrm{M}}}{z_{\mathrm{M}}} \simeq (\sigma_{\mathrm{X}} + \sigma_{\mathrm{M}}) t_{\mathrm{el}} \frac{\nabla\mu_{\mathrm{X}}}{z_{\mathrm{X}}} \tag{4.51}$$

containing the sum of the ionic conductivities. The normalized deviation from stoichiometry in a local equilibrium cell can be written as

$$N_{\mathrm{X}}/N_{\mathrm{M}} - |z_{\mathrm{M}}/z_{\mathrm{X}}| = \Gamma_{\mathrm{X}}/N_{\mathrm{M}} \tag{4.52}$$

where Γ_{X} is the excess of component X. For a system with ~ 1 point defects per $\sim 10^4$ atoms the deviation from stoichiometry seems indeed negligible.

But, the analysis neglects the effect of a non-vanishing local charge density on the variation of the chemical potentials. Furthermore, in polycrystalline materials the possibility of internal oxidation at extended defects adds a further complication. The internal creation or dissolution of material at grain boundaries for example would induce stress and the free energy of the oxide creation reaction, g_{X}, must vanish for local ionic equilibrium equilibrium to hold

$$g_{\mathrm{X}}(r) = |z_{\mathrm{X}}|\mu_{\mathrm{M}}^{z}(r) + |z_{\mathrm{M}}|\mu_{\mathrm{X}}^{z}(r) - \boldsymbol{\sigma}(r)\Omega_{\mathrm{u}} = 0 \tag{4.53}$$

[1] Referred to as the Duhem-Margules equation by Wagner [189].

where $\boldsymbol{\sigma}$ is the stress and Ω_{u} is the volume per formula unit of material. If this equilibrium holds the gradient of the free energy of reaction vanishes

$$\nabla g_{\mathrm{X}} = 0. \tag{4.54}$$

This problem is further discussed in section 4.3.1.2. Deviations from ionic equilibrium locally have been first discussed by Wagner [194] and Fromhold [47, 48], but their treatment does not involve the stress state. A discussion involving stress generation was given for example by Atkinson [1], whose treatment has been discussed already in chapter 3 section 3.5.

4.3.1.1 Monocrystalline scales

In monocrystalline scales topology forbids the internal creation of vacancies, the lattice inside monocrystals has to be preserved. This is why internal Schottky equilibrium is not satisfied in general within a monocrystal, the deviation from equilibrium depends on the chemical potential gradients imposed upon the crystal and the mobile species transport rates. Frenkel defect pairs of vacancies and interstitials can of course occur in monocrystals but are not the main concern of this work. Given internal ionic equilibrium does not hold

$$|z_{\mathrm{X}}|\mu^z_{\mathrm{M}}(r) + |z_{\mathrm{M}}|\mu^z_{\mathrm{X}}(r) \neq 0 \tag{4.55}$$

the ionic current density is written as

$$I_{\text{ion}} = -\sigma_{\mathrm{X}}\left(\frac{\nabla\mu^z_{\mathrm{X}}}{z_{\mathrm{X}}} + \nabla\phi\right) - \sigma_{\mathrm{M}}\left(\frac{\nabla\mu^z_{\mathrm{M}}}{z_{\mathrm{M}}} + \nabla\phi\right) \tag{4.56}$$

$$= -\sigma_{\mathrm{X}}t_{\text{el}}\frac{\nabla\mu_{\mathrm{X}}}{z_{\mathrm{X}}} - \sigma_{\mathrm{M}}t_{\text{el}}\frac{\nabla\mu_{\mathrm{M}}}{z_{\mathrm{M}}} - \underbrace{(\sigma_{\mathrm{X}}t_{\mathrm{M}} - \sigma_{\mathrm{M}}t_{\mathrm{X}})}_{=0}\left(\frac{\nabla\mu^z_{\mathrm{X}}}{z_{\mathrm{X}}} - \frac{\nabla\mu^z_{\mathrm{M}}}{z_{\mathrm{M}}}\right) \tag{4.57}$$

$$= \sigma_{\mathrm{X}}t_{\text{el}}\frac{\nabla\mu_{\mathrm{X}}}{|z_{\mathrm{X}}|} - \sigma_{\mathrm{M}}t_{\text{el}}\frac{\nabla\mu_{\mathrm{M}}}{|z_{\mathrm{M}}|} \tag{4.58}$$

which is split into contributions of the anions and cations. By using the fact that the individual currents are constant as a function of position in the scale the ionic current density is further written as

$$I_{\text{ion}} = \frac{1}{L}\int_I^{II}\sigma_{\mathrm{X}}t_{\text{el}}\frac{d\mu_{\mathrm{X}}}{|z_{\mathrm{X}}|} - \frac{1}{L}\int_I^{II}\sigma_{\mathrm{M}}t_{\text{el}}\frac{d\mu_{\mathrm{M}}}{|z_{\mathrm{M}}|}. \tag{4.59}$$

In Wagner's theory on the other hand it would now be further assumed that internal ionic equilibrium holds requiring

$$\frac{d\mu_{\mathrm{X}}}{|z_{\mathrm{X}}|} = \frac{d\mu_{\mathrm{M}}}{|z_{\mathrm{M}}|}, \tag{4.60}$$

and only by this assumption the two integrals in equation 4.59 could be formulated as one with the characteristic form of the integrand, $(\sigma_{\mathrm{X}} + \sigma_{\mathrm{M}})t_{\mathrm{el}}$. The form of the integrand was discussed further in section 4.2.1.

Equation 4.59 is therefore the straightforward generalization upon the Wagner rate formula, see equation 4.5, in the absence of internal ionic (Schottky) equilibrium. The oxidation rate follows by applying the ionic current defined in equation 4.59 in the rate equation 4.3 given at the beginning of section 4.2.

4.3.1.2 Polycrystalline scales

The spatial variation of the species concentrations and chemical potentials in a polycrystalline scale is determined by the distribution of the fluxes, J_s, and reactions, R_s, within the grains, and on its surface and interfaces. The evolution of the concentrations, the fluxes, and the reactions are connected by the continuity equation

$$\partial_t c_s = -\nabla \cdot J_s + R_s. \tag{4.61}$$

In the steady-state the concentrations are stationary and hence

$$\nabla \cdot J_s = R_s \tag{4.62}$$

holds at any point within the material, see figure 4.5 for a pictorial interpretation.

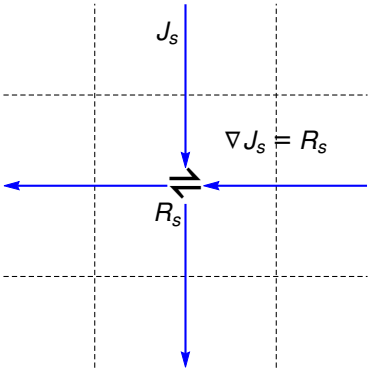

FIGURE 4.5: The fluxes between the volume elements of the material are related to the chemical reactions within the volume elements.

If oxide is formed or dissolved internally at extended defects, such as dislocations or grain boundaries, the chemical potentials of the cations and anions are related through the internal oxidation reaction; the free energy of reaction, as defined in section 4.3.1,

$$g_{\mathrm{X}}(r) = |z_{\mathrm{X}}|\mu^{z}_{\mathrm{M}}(r) + |z_{\mathrm{M}}|\mu^{z}_{\mathrm{X}}(r) - \boldsymbol{\sigma}(r)\Omega_{\mathrm{u}} \tag{4.63}$$

quantifies the deviation from internal equilibrium for which $g_{\mathrm{X}} = 0$. As mentioned in chapter 3 section 3.5.5, the free energy of reaction is distinguished from the chemical affinity

$$\mathcal{A}(r) = |z_{\mathrm{M}}|\mu^{z}_{\mathrm{X}}(r) + |z_{\mathrm{X}}|\mu^{z}_{\mathrm{M}}(r). \tag{4.64}$$

that quantifies the deviation from local ionic equilibrium. The notion is also distinguished from the 'local equilibrium' hypothesis in irreversible thermodynamics. In the theory of irreversible thermodynamics the material is imagined to be partitioned into 'local equilibrium cells' of such size that changes due to the thermodynamic fluctuations exceed the thermodynamic driving forces across any particular cell, thereby establishing 'local equilibrium' [87, 146].

The reactions between oxidant and metal are related by stoichiometry

$$\frac{1}{|z_{\mathrm{M}}|}R_{\mathrm{X}} = \frac{1}{|z_{\mathrm{X}}|}R_{\mathrm{M}} \tag{4.65}$$

and in the steady-state the divergences of the fluxes are therefore related by

$$\frac{1}{|z_{\mathrm{M}}|}\nabla \cdot J_{\mathrm{X}} = \frac{1}{|z_{\mathrm{X}}|}\nabla \cdot J_{\mathrm{M}}. \tag{4.66}$$

This means the divergence of the ionic current density,

$$I_{\text{ion}} = z_{\mathrm{X}}e_0 J_{\mathrm{X}} + z_{\mathrm{M}}e_0 J_{\mathrm{M}}, \tag{4.67}$$

vanishes at any point in the material

$$\nabla \cdot I_{\text{ion}} = 0 \tag{4.68}$$

independent of the attainment of ionic equilibrium between cations and anions within the scale.

However, despite a constant ionic current density, the growth rate cannot be formulated in a simple manner as in the integral equation 4.5. The individual fluxes are not

constant and the growth rate depends on the respective species fluxes at the metal–scale, $x = 0$, and scale–environment interface, $x = L$,

$$\frac{dL}{dt} \sim z_{\mathrm{X}} J_{\mathrm{X}}(0) + z_{\mathrm{M}} J_{\mathrm{M}}(L). \tag{4.69}$$

The fluxes are connected to the reactions and even by neglecting the effect of stress and in the limit of internal ionic equilibrium, $\mathcal{A} = 0$, the fluxes cannot in general be expected to be constant,

$$\nabla \cdot J_s(r) \neq 0. \tag{4.70}$$

The attainment of local ionic equilibrium depends on the relative magnitudes of the reaction and diffusion rates.

This casts doubt on the application of the Wagner theory to grain boundary transport dominated scales such as alumina in which internal oxidation and lateral growth stresses are observed, see chapter 3 section 3.5.2. Assuming the grain boundaries act as sources and sinks of defects, Schottky equilibrium is typically assumed to hold locally. But, the necessary condition of constant fluxes for Wagner's rate formula 4.5 cannot be strictly true if there is formation or dissolution of oxide at the grain boundaries during growth. This is because the induced stresses, which are observed experimentally, cause a modification in the fluxes as a function of the position in the grain boundary. The later effect has been demonstrated in the simulations with the hexagonal cell model detailed in chapter 3 section 3.5.

At this point no analytic alternative to Wagner's rate equation 4.5 is available, that takes into account the effect of stress and the deviation from internal ionic equilibrium. The computational model presented in chapter 3 section 3.5 does, however, allow for numeric calculations taking into account these effects.

4.3.2 Limiting solutions – singular perturbation approach

The Poisson-Nernst-Planck (PNP) system of equations cannot be solved analytically in general, a numerical solution method has been developed and is described in chapter 3 of this work. Analytical closed form solutions are useful for gauging the numerical solution method and for making the essential features of the PNP system readily apparent.

The calculations described here make evident the connection between 'diffusion-reaction' and the electric field dependent 'drift-diffusion-reaction' equations. The derivations show that the solution of 'drift-diffusion-reaction' equations is closely related

to 'diffusion-reaction' solutions in, perhaps surprisingly, the limit of a strong self-consistent electric field in the 'drift-diffusion-reaction' model. It is argued that in the limit of a strong self-consistent electric field the transport maps onto a model of diffusion-reaction only, but with an effective diffusion coefficient. Furthermore, the method makes apparent how the local charge neutrality approximation becomes an increasingly more accurate approximation in the limit of a small screening parameter, $\kappa = \ell_{\mathrm{D}}/L$, and how the self-consistent electric field increases in magnitude as κ gets smaller.

Solutions for the simplified special case of two mobile species are obtained here. The two species could be thought of as the dominant vacancy and charge compensating electronic species as in the alumina membrane permeation simulations presented in chapter 3, but the developed formulae are more generally applicable.

I have argued in sections 4.2.4 and 4.2.3 that the dimensionless ratio of the reference Debye length over the film thickness denoted by $\kappa = \ell_{\mathrm{D}}/L$ is the chief parameter governing the behaviour of the PNP system of equations, with regards to the assumptions of local charge neutrality and the steady-state. In what follows, I use κ as a perturbation parameter, and due to the special nature of the PNP equations pertaining to the fulfillment of the boundary conditions, it is an application of what is known as 'singular perturbation theory' in the literature, e.g. [97]. Singular perturbation theory and a length-scale separation ansatz have been applied in mathematical investigations in the semiconductor and device literature [113, 150, 158], and in ion channel transport [161].

For approximations it is convenient to rescale the equations to estimate relative magnitudes of terms, the scaling is discussed in more detail in chapter 2 section 2.6.1. The film thickness, L, denotes the reference length for the problem and the scaled PNP system of equations reads as

$$\partial_t c_s = -\nabla \cdot J_s \tag{4.71}$$

$$\kappa^2 \nabla^2 \phi = -\rho. \tag{4.72}$$

The parameter κ also appears in the Maxwell-Ampere law

$$\kappa^2 \partial_t \nabla \phi - \sum_s z_s J_s = 0 \tag{4.73}$$

which is related to the Poisson equation through the continuity equation. The Debye-Hückel screening parameter, λ_{D}, is defined by

$$\lambda_{\mathrm{D}}(c_s, T, \varepsilon_r, z_s) = \left(\frac{\varepsilon_r \varepsilon_0 k_{\mathrm{B}} T}{e_0^2 \sum_s z_s^2 c_s} \right)^{1/2} \tag{4.74}$$

and for the film growth or membrane permeation problem its value varies with position since the concentrations, $c_s(r)$, depend on the position. The reference screening length, ℓ_{D}, is introduced as a parameter representative of the true screening length λ_{D}.

The position dependent concentrations are replaced by the constant c_0 which is chosen as the maximum of the concentrations in the domain

$$c_0 = \max_{s,r}\{c_s(r)\} \quad \text{and} \quad \ell_{\mathrm{D}} = \left(\frac{\varepsilon_r \varepsilon_0 k_{\mathrm{B}} T}{e_0^2 c_0} \right)^{1/2}. \tag{4.75}$$

The concentration c_0 is expected to be the surface concentration of the dominant species and therefore depends on the boundary conditions through e.g. the oxygen partial pressure and the equilibrium constants, $c_{\overline{\nu}}(P_{\mathrm{O}_2}, K_i)$.
The derivations are given for two mobile species which are denoted by ν and $\overline{\nu}$, where it is assumed that

$$(\nu, \overline{\nu})\text{-notation}: \quad |z_{\overline{\nu}}| = 1 \quad \text{and} \quad \mathrm{sgn}\{z_\nu\} = -\mathrm{sgn}\{z_{\overline{\nu}}\}. \tag{4.76}$$

In what follows it is shown that while the steady-state concentrations $c_s(x;\kappa)$ converge uniformly to $c_s(x;0)$ in the limit of $\kappa \to 0$, the electric field $-\nabla\phi(r;\kappa)$ does not converge uniformly to $-\nabla\phi(r;0)$. The singular perturbation parameter κ denotes the ratio of the range of charge screening effects characterized by the reference Debye screening length ℓ_{D}, to the range of the macroscopic electrostatic field characterized by the film thickness L.

4.3.2.1 The non-interacting system

Here, the PNP system is investigated by considering a special case in the parameters to obtain an analytically soluble 'non-interacting' problem. Then the screening parameter κ is used in a perturbation approach beyond the non-interacting special case.

The analytically soluble special case consists of two mobile species $(\nu, \overline{\nu})$ with equal diffusion coefficients $D_\nu = D_{\overline{\nu}} = D$. The value of D does not affect the steady-state solutions of the concentration profiles. Since the species diffuse at the same rate and are created or annihilated by law of mass action type reactions in stoichiometric

proportions the system is locally charge neutral at any position and time $\rho(x,t) = 0$; the species do not interact the electric field vanishes $-\nabla\phi(x,t) = 0$. The solution of the non-interacting system is considered identical to the $\kappa = 0$ solution in the perturbation treatment. The fluxes are in stoichiometric proportions,

$$|z_\nu| J_\nu = J_{\overline{\nu}} \tag{4.77}$$

$$|z_\nu| \left(c_\nu^{II} - c_\nu^{I}\right) = \left(c_{\overline{\nu}}^{II} - c_{\overline{\nu}}^{I}\right) \tag{4.78}$$

where $|z_{\overline{\nu}}| = 1$ has been used, and since $\rho = 0$ the concentrations on the surface or interface can be calculated from the law of mass action

$$|z_\nu| c_\nu^j = c_{\overline{\nu}}^j \tag{4.79}$$

$$c_\nu^j = f_\nu P_{\mathrm{O}_2}^{n_\nu}(j) \tag{4.80}$$

where $j \in \{I, II\}$, and the c_ν^j are determined from the boundary conditions and the equilibrium constants, $c_\nu^j(P_{\mathrm{O}_2}^j, K_i)$. The concentrations vary linearly

$$c_s^{(0)}(x) = k_s x + c_s^I \tag{4.81}$$

where in particular $k_s = c_s^{II} - c_s^I$, the superscript (0) denotes the non-interacting solution, and $s \in \{\nu, \overline{\nu}\}$.

4.3.2.2 The length-scale separation ansatz

The concentration profiles are approximated uniformly up to order κ by smooth, slowly varying functions which are independent of κ and derived from the non-interacting system obtained by setting $D_s = D$ and considered equivalent to a $\kappa = 0$ solution. The solution in the limit

$$\kappa \to 0 \tag{4.82}$$

is investigated with an ansatz that contains the x/L varying reduced solution, $c_\nu^{(0)}$, and a x/ℓ_{D} varying screening term which is expected to describe $\sim \exp(\pm x/\ell_{\mathrm{D}})$ varying boundary layers.

The 'scale separation' ansatz to take into account the boundary layers is written as

$$c_\nu(x;\kappa) = c_\nu^{(0)}(x) + \kappa\, c_\nu^{(1)}(x/\kappa) \tag{4.83}$$

where again

$$|z_\nu| c_\nu^{(0)}(x) + c_{\overline{\nu}}^{(0)}(x) = 0 \;\; \forall x \tag{4.84}$$

and $c_\nu^{(1)}$ contains the screening effects and vanishes for $x \in [0,1]$ in the limit $\kappa \to 0$

$$\lim_{\kappa \to 0} c_\nu(x;\kappa) \to c_\nu^{(0)}(x) \;\; \forall x \tag{4.85}$$

In the limit the gradient of the concentration is given by

$$\nabla c_\nu = k_\nu + c_\nu^{(1)\prime} \tag{4.86}$$

$$\lim_{\kappa \to 0} \nabla c_\nu(x;\kappa) = \begin{cases} 0, & \text{if } \; x \in \{0,1\} \\ k_\nu, & \text{otherwise} \end{cases} \tag{4.87}$$

The electric field $E = -\nabla\phi$, flux and charge density in the limit and $x \in (0,1)$ are given by,

$$\lim_{\kappa \to 0} J_\nu(x;\kappa) = J_\nu^{(0)}(x) = -D^{\text{eff}} k_\nu \tag{4.88}$$

$$\lim_{\kappa \to 0} E(x;\kappa) = E^{(0)}(x) = D' \frac{k_\nu}{c_\nu^{(0)}(x)} \tag{4.89}$$

where with $|z_{\overline{\nu}}| = 1$,

$$D^{\text{eff}} = \frac{D_\nu D_{\overline{\nu}}}{D_\nu |z_\nu| + D_{\overline{\nu}}} (|z_\nu| + 1) \tag{4.90}$$

$$D' = z_{\overline{\nu}} \frac{D_{\overline{\nu}} - D_\nu}{D_\nu |z_\nu| + D_{\overline{\nu}}} \tag{4.91}$$

and where equations 4.73 and 4.84, relation 4.87, and the sum and product rules of limits have been used.

From equation 4.89 the electrostatic potential in the limit is given by

$$\lim_{\kappa \to 0} \phi(x) = -D' \, \ln\left(\frac{k_\nu x + c_\nu^I}{c_\nu^I}\right) \tag{4.92}$$

and the electrostatic potential difference during growth tends to a constant

$$\lim_{\kappa \to 0} \Delta\phi = -D' \ln\left(\frac{c_\nu^{II}}{c_\nu^I}\right) = -D' \Delta\mu_\nu = \text{const.} \tag{4.93}$$

which by using $\Delta\mu_\nu = n_\nu \Delta\mu_{O_2}$ can also be written as

$$\lim_{\kappa\to 0} \Delta\phi = -D' n_\nu \Delta\mu_{O_2}. \tag{4.94}$$

Since $D' < 1$ an upper bound for the electrostatic potential difference reads as

$$|\Delta\phi| < |n_\nu \Delta\mu_{O_2}|. \tag{4.95}$$

4.3.2.3 The local charge density and screening

The local charge density vanishes in the limit of $\kappa \to 0$,

$$\lim_{\kappa\to 0} \rho(x) = \lim_{\kappa\to 0} \kappa^2 \nabla \cdot E \to 0, \tag{4.96}$$

and approaches the $\kappa = 0$ solution; however, the electric field differs from the $\kappa = 0$ solution in the limit. The solution $E^{(0)}$, see equation 4.89, is consistent with the surface charges, γ_j,

$$\gamma_j = \kappa^2 D' \frac{k_\nu}{c_\nu^j}, \tag{4.97}$$

$$\gamma_I + \gamma_{II} + \int_0^1 \kappa^2 \nabla \cdot E^{(0)} dx = 0. \tag{4.98}$$

The screening behaviour is lost in the limiting solutions. Screening effects can be recovered if the first order terms are considered in the concentrations, which leads to the electric field expression,

$$E \approx D' \frac{k_\nu}{c_\nu^{(0)}(x)} + \frac{z_{\overline{\nu}}}{D_\nu |z_\nu| + D_{\overline{\nu}}} \frac{D_{\overline{\nu}} c_{\overline{\nu}}^{(1)\prime}/|z_\nu| - D_\nu c_\nu^{(1)\prime}}{c_\nu^{(0)}(x)}, \tag{4.99}$$

where first order terms, $\kappa c_s^{(1)}$, in the denominator have been neglected. Assuming that $E(0) = E(1) = 0$, and that the $E^{(0)}$ solution should be approached away from the surfaces suggests the approximation,

$$D_{\overline{\nu}} c_{\overline{\nu}}^{(1)\prime}/|z_\nu| - D_\nu c_\nu^{(1)\prime} \approx -(D_{\overline{\nu}} - D_\nu) k_\nu \left(\exp(-x/\kappa) + \exp(-(1-x)/\kappa)\right). \tag{4.100}$$

To capture screening effects for small κ, the electric field therefore takes the form

$$\begin{aligned} E(x) &= E^{(0)}(x) + E^{(1)}(x/\kappa) \\ &= D' \frac{k_\nu}{c_\nu^{(0)}(x)} \Big(1 - \exp(-x/\kappa) - \exp(-(1-x)/\kappa) \Big) \end{aligned} \tag{4.101}$$

where the exponential terms, $\exp(\cdot) \in (0, 1]$, and $E(0) = E(1) = 0$. The zeroth order solution $E^{(0)}(x)$ for the electric field is not approached uniformly in the $\kappa \to 0$ limit by the κ dependent solution, $E(x; \kappa)$, due to the different behaviour near the surfaces, see figure 4.6. Hence, the problem is identified as a singular perturbation problem.

The charge density takes the form

$$\begin{aligned} \rho = \kappa^2 \nabla \cdot E = -D' \left(\frac{k_\nu}{c_\nu^{(0)}(x)} \right)^2 \Big(1 - \exp(-x/\kappa) - \exp(-(1-x)/\kappa) \Big) \kappa^2 + \\ D' \frac{k_\nu}{c_\nu^{(0)}(x)} \Big(\exp(-x/\kappa) - \exp(-(1-x)/\kappa) \Big) \kappa \end{aligned} \tag{4.102}$$

where the charge density in the interior vanishes $\mathcal{O}(\kappa^2)$ more rapidly than near the surfaces $\mathcal{O}(\kappa)$. The electric field and the charge density are shown in figure 4.6.

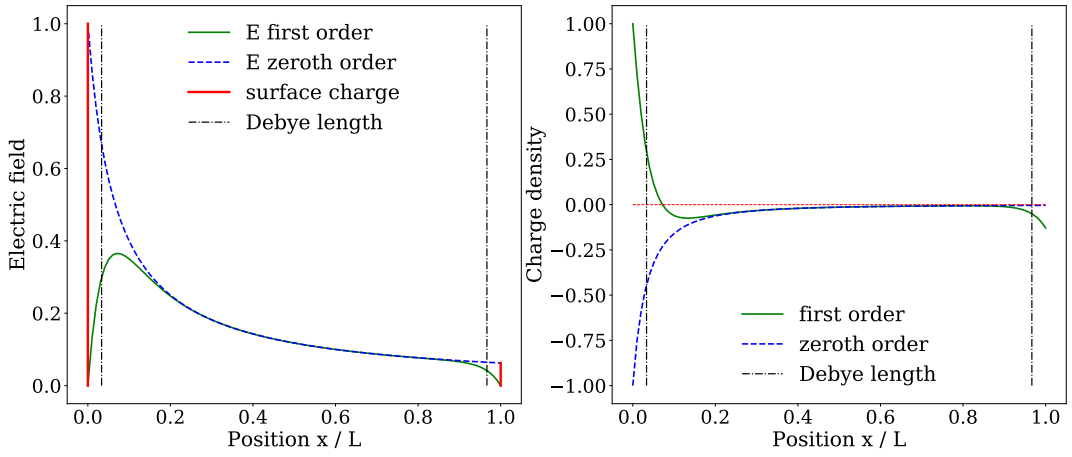

FIGURE 4.6: Analytical investigation of the electric field and space charge that would correspond to a oxygen membrane permeation scenario of $P_{O_2}^{II} = P_{O_2}^{hi}$ at $x = 1$ and $P_{O_2}^{I} = P_{O_2}^{eq}$ at $x = 0$, see chapter 3. Scaled units are used. The screening behaviour is captured by the first order approximation with characteristic length scale κ. The first order approximation of the local charge density departs significantly from the zeroth order counterpart in the vicinity of the surfaces. The first order approximations converge to the zeroth order approximations in the bulk zone a few Debye lengths away from the surfaces.

4.3.2.4 The electric field effect: Retardation *vs.* enhancement

In the limit of local charge neutrality, the surface concentrations of the dominant vacancy species 'ν' and electronic species '$\overline{\nu}$' are given by

$$c_\nu = c_{\overline{\nu}}/|z_\nu| = f_\nu \; P_{\mathrm{O}_2}^{n_\nu} \tag{4.103}$$

where the prefactor, f_ν, depends on the equilibrium constants, and the power law exponent, n_ν, depends on the species charge state.

A purely diffusive flux in steady-state of species 's' with boundary conditions of c_s^{II} and c_s^I would read as

$$J_s = -D_s \frac{c_s^{II} - c_s^I}{L}. \tag{4.104}$$

In the presence of the self-consistent electric field the flux of the dominant vacancy species 'ν' reads as

$$J_\nu = -D^{\text{eff}} \frac{c_\nu^{II} - c_\nu^I}{L} \tag{4.105}$$

$$D^{\text{eff}} = \frac{D_\nu D_{\overline{\nu}}}{D_\nu |z_\nu| + D_{\overline{\nu}}} (|z_\nu| + 1) \tag{4.106}$$

where $\overline{\nu}$ again denotes the charge compensating species with $|z_\nu| = 1$, the derivation is discussed in section 4.3.2.2. If $D_\nu \gg D_{\overline{\nu}}$ the vacancy flux could be thought of as being retarded with respect to pure diffusion since

$$D^{\text{eff}} \simeq (|z_\nu| + 1) D_{\overline{\nu}} < D_\nu \tag{4.107}$$

and for $D_\nu \ll D_{\overline{\nu}}$ the electric field effect could be thought of as enhancing the vacancy diffusion since in this case

$$D^{\text{eff}} \simeq (|z_\nu| + 1) D_\nu > D_\nu. \tag{4.108}$$

However, the comparison to pure diffusion is misleading since the surface concentrations would change if they were not restricted by the electric field.

4.3.3 Linear to square root law transition in the growth rate

In section 4.3.2.3 a κ-dependent expression for the electric field beyond the local charge neutrality approximation has been given in equation 4.101. A κ-dependent flux is calculated by averaging over the film thickness while using the κ-dependent electric field of equation 4.101,

$$J_\nu = \int_0^1 -D_\nu(\nabla c_\nu + z_\nu c_\nu \nabla\phi)\, dx \tag{4.109}$$

and the flux containing a screening correction term is evaluated as

$$J_\nu = -D^{\text{eff}} k_\nu + \kappa\, k^{(1)}. \tag{4.110}$$

In what follows it is shown that this κ-dependent correction term in the flux, J_ν, leads to a modification in the growth rate behaviour. For $D_{\overline{\nu}} \gg D_\nu$ where the constant $k^{(1)} = -2|z_\nu| D_\nu k_\nu$, the flux reads as,

$$J_\nu \simeq -D_\nu k_\nu \Big(1 + |z_\nu|\,(1 - 2\kappa) \Big) \tag{4.111}$$

which applies for $2\kappa < 1$. The growth rate is calculated from the defect flux,

$$\frac{dL}{dt} = \Omega_\nu |J_\nu| \tag{4.112}$$

where Ω_ν is the volume added per particle of species ν reaching the surface. The growth rate law including the first order correction term can hence be written as,

$$\frac{dL}{dt} = \frac{k_{\text{p}}}{L} \left(1 - k_C \frac{\ell_{\text{D}}}{L} \right) \tag{4.113}$$

where k_C is a constant on the order of magnitude one, k_{p} is a constant with the dimensions of the diffusion coefficient, D_ν, and where the definition $\kappa = \ell_{\text{D}}/L$ has been used. The differential equation can be solved readily, and by neglecting the second order term $\mathcal{O}(\ell_{\text{D}}^2)$ as well as demanding $L(0) = 0$, the thickness as a function of time is given by

$$L(t) = k_C \ell_{\text{D}} \left(\sqrt{1 + \frac{2k_p}{(k_C \ell_{\text{D}})^2} t} - 1 \right). \tag{4.114}$$

There are two growth regimes contained in equation 4.114, a transition from a linear to square root (parabolic law) time dependence is predicted for the film thickness,

$L(t)$. First, for time t adhering to

$$\frac{2k_p}{(k_C\ell_{\mathrm{D}})^2}t \ll 1 \tag{4.115}$$

a linear regime is obtained from equation 4.114, by a first order series expansion of the square root expression, which yields

$$L(t) \simeq \frac{k_{\mathrm{p}}}{k_C\ell_{\mathrm{D}}}t. \tag{4.116}$$

Second, for time t adhering to

$$\frac{2k_p}{(k_C\ell_{\mathrm{D}})^2}t \gg 1 \tag{4.117}$$

the thickness as a function of time asymptotically approaches the square root time dependence,

$$L(t) \simeq \sqrt{2k_{\mathrm{p}}t} \tag{4.118}$$

where k_{p} appears as the 'parabolic' rate constant.

Taking into account a simple screening model near the interfaces, therefore, leads to the prediction of a linear regime preceding the square root time dependence that is characteristic of diffusive behaviour.

The constant k_{p} has the dimensions of a diffusion coefficient and the time scale associated with the linear regime could be related to the 'charging time' constant $\tau_{\mathrm{c}} = \lambda_{\mathrm{D}}L/D$ discussed in reference [12], which depends on the Debye length, λ_{D}, and the diffusion coefficient, D. The time scale τ_{c} is thought of as a capacitor charging time, characteristic of the build-up or depletion of a screening layer near a charged surface [12].

4.4 Summary

A formulation of the Wagner theory of metal oxidation in terms of the ionic current density has been described, and an intuitive circuit equivalence model for Wagner's rate equation has been introduced.

The internal ionic equilibrium is typically discussed by recourse to the Gibbs-Duhem equation and local charge neutrality assumption as outlined section 4.3.1. In contrast, it has been argued here that the attainment of internal ionic equilibrium – an

essential assumption of the Wagner theory – has to be discussed in terms of the defect transport and reaction rates which requires a computational simulation model as presented in chapter 3. In polycrystalline scales the attainment of local ionic equilibrium at the grain boundaries or dislocations of the scales is complicated by the generation of tensile or compressive stresses and the assumptions necessary for the validity of the Wagner theory are not fulfilled. An analytic model extending the Wagner theory to account for growth stresses is not available at present. Thus, further work is required to achieve a consistent analytic model that can be used to interpret scale growth experiments.

The theory of singular perturbations has been applied here to the problem of drift-diffusion limited growth to obtain analytical closed expressions for the key quantities involved. The potential of this approach is demonstrated by the prediction of a linear to square root (parabolic) law in the film growth rate in section 4.3.3.

Linear growth regimes have been observed in oxidation experiments but are typically attributed to reactions as the rate limiting step instead of the ionic or electronic transport. Further work is required to determine by computer simulation or experiment, if the linear growth law described here is indeed observable during metal oxidation.

Chapter 5

Conclusions

This thesis presents a model for time-dependent grain boundary diffusion of ions and electrons through a film of polycrystalline oxide. The granular structure of the film is idealized as a slab comprised of hexagonal columnar grains.

The model has been applied to the archetypical oxide 'alumina' in two different scenarios, membrane oxygen permeation, and steady-state alumina film growth on an alloy surface. In alumina the ionic transport is dominated by grain boundaries, which act as preferential pathways for the ion transfer through the film. Despite decades of intense study on polycrystalline alumina the grain boundary transport mechanisms are still elusive, unintentional doping effects and the occurrence of electric fields and stresses during oxidation complicate the analysis of the experimental data. The hexagonal cell model developed in this work takes into account the internal electric field, and a simple model for stress generation within thin films self-consistently with a generic description of the transport processes during oxidation or membrane permeation. The model is therefore well suited to complement experimental studies and to analyze the validity of simplified analytic models, such as the Wagner theory of metal oxidation.

In the first application of the model, described in chapter 3 of this work, alumina membrane oxygen permeation has been simulated. Four mobile defects, charged aluminum and oxygen vacancies, electrons and holes, have been considered, and the simulation results are compatible with the experimental results of Kitaoka *et al.* [83]. These membrane permeation experiments on high purity alumina enable to elucidate the ionic transport through alumina films; the experimental methodology has been reproduced in the computer simulations for a comparative analysis.

In the limits of high and low oxygen partial pressure applied on the membrane surfaces distinct power laws describe the oxygen permeation rate, this experimental

finding has been reproduced in the simulations and is evidence for the notion of vacancies carrying nominal ionic charges. The calculated power laws for the permeation rate depend on the stoichiometry of the quasi-chemical reactions at the membrane surfaces, and on the efficacy of local charge neutrality. That is, in the limit of a small Debye screening length compared to the grain size the magnitude of the local charge density is small and the fractional power law exponents emerge in the simulations. The simulation method takes into account the long-range Coulomb interactions between the grain boundary planes and the membrane surfaces. The Coulomb interactions between the grain boundary planes affects the mass transfer dynamics through the slab significantly only during the initial transient. The electric field generated by the evolution of the charge density influences the transport significantly; in the long time limit it is dominated by the surface charges.

A simplified, one-dimensional analytic model has been introduced that employs the approximation of a single dominant defect, which appears from the 3D calculation to be justified. The analytic model has been shown to agree well with the simulation results under certain limiting conditions, but fails in the intermediate oxygen partial pressure regime.

Experimental data on alumina indicates that the ionic and electronic transport numbers are of similar magnitude, therefore, the possibility of vacancies diffusing faster than the electronic species cannot be excluded. The open circuit voltage has been examined in the membrane permeation simulations and it is suggested that the experimental measurement of the voltage compared to the simulation results could clarify the relative magnitudes of the dominant vacancy and electronic species diffusion coefficients.

In the second application, the hexagonal cell model has been extended to include a Schottky reaction at the grain boundaries coupled to a simple model for the resulting generation of internal stresses. Lateral growth stresses are predicted in the simulations for conditions that are considered close to steady-state alumina scale growth on an alloy surface at high temperatures. The calculated stresses have similar magnitude as those measured experimentally in high-temperature oxidation experiments. The simulations enable a detailed understanding of the stress generation and evolution, which is essential for predicting the stability of alumina scales as high-temperature oxidation barriers in thermal barrier coatings.

For simulations with coupled internal reactions, stresses, and fluxes a deviation from local Schottky equilibrium at the grain boundary has been observed. Consequently, it has been argued that the assumptions for an application of the Wagner theory are not satisfied for the physical conditions investigated.

The simulations demonstrate a $p - n$ ionic transition within an alumina film, that depends sensitively on the diffusion rates. This partially confirms the hypothesis by Heuer *et al.* [70], and makes the properties of the transition accessible for further study. The location of the $p - n$ transition can be predicted from the simulations, and depends strongly on the diffusion coefficients of the mobile species. Comparison of the simulation results to experimental data seems to show that the diffusion coefficients of vacancies, electrons, and holes could be of surprisingly similar magnitude. If true, this could indicate the presence of a cooperative transport mechanism. However, some experiments seem to indicate that interstitial diffusion through the grain boundaries cannot be neglected, as has been done in this work. Furthermore, the transport mechanisms of the vacancies in alumina grain boundaries are not agreed upon in the literature, and the microscopic electron and hole transport mechanisms are unknown. The focus in the literature has been mostly on vacancy grain boundary diffusion, therefore, further work would be of value to illuminate the electron and hole transport mechanism and recombination, which could be achieved by *ab initio* simulations.

The numerical solution method for the time-dependent Poisson-Nernst-Planck system of equations with reaction boundary conditions has been implemented in an object oriented C++ code, and has been used throughout to generate the simulation results. The simulation methodology is similar to semiconductor device simulations and the wealth of literature on this subject was drawn upon in the numerical formulation and computational implementation. The implementation has been successfully benchmarked against one-dimensional analytical models applicable in limiting cases.

The question of validity of mapping the transport through grain boundaries and grains of a polycrystalline film onto a one-dimensional model remains largely open. In this work only the transport through the grain boundaries of an idealized film has been investigated. Further work would be of value to extend the model by including transport in the grains, which is required for capturing the effect of space charge layers ranging from the interfaces into the grains. It is expected that inclusion of these space charge layers would lead to a more pronounced dependence of the simulation results on the grain shape than has been observed in the simulations described in this work. Such further development would be significant for more advanced oxidation rate models of polycrystalline films, and for assessing the applicability of established one-dimensional models.

Bibliography

[1] A. Atkinson. Conditions for the formation of new oxide within oxide films growing on metals. *Corros. Sci.*, 22:347–357, 1982.

[2] A. Atkinson. Transport processes during the growth of oxide films at elevated temperature. *Rev. Mod. Phys.*, 57:437–470, 1985.

[3] A. Atkinson, R. I. Taylor, and A. E. Hughes. A quantitative demonstration of the grain boundary diffusion mechanism for the oxidation of metals. *Philos. Mag. A*, 45:823–833, 1982.

[4] H. V. Atkinson. A review of the role of short-circuit diffusion in the oxidation of nickel, chromium, and nickel-chromium alloys. *Oxid. Met.*, 24:177–197, 1985.

[5] R. W. Balluffi, S. Allen, and W. C. Carter. *Kinetics of Materials*. John Wiley & Sons, Inc., 2005.

[6] J. Balmain and A. M. Huntz. Improvement of the application of an electrochemical method for the determination of transport properties of an α-alumina scale. Part II: Influence of yttrium and palladium on alumina scales developed on β-NiAl alloy. *Oxid. Met.*, 46:213–234, 1996.

[7] J. Balmain and A. M. Huntz. Improvement of the Application of an Electrochemical Method for the Determination of Transport Properties of an Alumina Scale. Part I : Alumina Scale on a β-NiAl Alloy. *Oxid. Met.*, 45:183–196, 1996.

[8] J. Bardeen, W. H. Brattain, and W. Shockley. Investigation of Oxidation of Copper by Use of Radioactive Cu Tracer. *J. Chem. Phys.*, 14:714–721, 1946.

[9] G. I. Barenblatt. *Scaling*. Cambridge University Press, Cambridge, 2003.

[10] V. Battaglia and J. Newman. Modeling of a Growing Oxide Film: The Iron/Iron Oxide System. *J. Electrochem. Soc.*, 142:1423–1430, 1995.

[11] I. Batyrev, A. Alavi, and M. W. Finnis. Ab initio calculations on the Al_2O_3(0001) surface. *Faraday Discuss.*, 114:33–43, 1999.

[12] M. Z. Bazant, K. Thornton, and A. Ajdari. Diffuse-charge dynamics in electrochemical systems. *Phys. Rev. E*, 70:021506, 2004.

[13] T. R. Brumleve and R. P. Buck. Numerical solution of the Nernst-Planck and Poisson equation system with applications to membrane electrochemistry and solid state physics. *J. Electroanal. Chem.*, 90:1–31, 1978.

[14] N. Cabrera and N. F. Mott. Theory of the oxidation of metals. *Rep. Prog. Phys.*, 12:163–184, 1949.

[15] H. B. Callen. *Thermodynamics and an Introduction to Thermostatistics*. Wiley, New York, 1985.

[16] H. Ceric, R. Heinzl, C. Hollauer, T. Grasser, and S. Selberherr. Microstructure and stress aspects of electromigration modeling. *AIP Conf. Proc.*, 817:262–268, 2006.

[17] C. Y. Chao, L. F. Lin, and D. D. Macdonald. A Point Defect Model for Anodic Passive Films. *J. Electrochem. Soc.*, 128:1187–1194, 1981.

[18] J.-N. Chazalviel. *Coulomb Screening by Mobile Charges*. Birkhäuser, Boston, 1999.

[19] T.-L. Cheng and Y.-H. Wen. Toward a quantitative understanding of the electric field in thermal metal oxidation and a self-consistent Wagner theory. *J. Phys. Chem. Lett.*, 5:2289–2294, 2014.

[20] T.-L. Cheng, Y.-H. Wen, and A. Hawk. Diffuse-Interface Modeling and Multiscale-Relay Simulation of Metal Oxidation Kinetics-With Revisit on Wagner's Theory. *J. Phys. Chem. C*, 118:1269–1284, 2014.

[21] S. Chevalier. Mechanisms and Kinetics of Oxidation. In *Shreir's Corrosion*, pages 132–152. Elsevier, 2010.

[22] M. Choi, A. Janotti, and C. G. Van de Walle. Native point defects and dangling bonds in α-Al_2O_3. *J. Appl. Phys.*, 1131:044501, 2013.

[23] R. J. Christensen, D. M. Lipkin, D. R. Clarke, and K. Murphy. Nondestructive evaluation of the oxidation stresses through thermal barrier coatings using Cr^{3+} piezospectroscopy. *Appl. Phys. Lett.*, 69:3754–3756, 1996.

[24] D. R. Clarke. Stress generation during high-temperature oxidation of metallic alloys. *Curr. Opin. Solid State Mater. Sci.*, 6:237–244, 2002.

[25] D. R. Clarke. The lateral growth strain accompanying the formation of a thermally grown oxide. *Acta Mater.*, 51:1393–1407, 2003.

[26] D. R. Clarke, M. Oechsner, and N. P. Padture. Thermal-barrier coatings for more efficient gas-turbine engines. *MRS Bull.*, 37:891–898, 2012.

[27] R. Darolia. Thermal barrier coatings technology: critical review, progress update, remaining challenges and prospects. *Int. Mater. Rev.*, 58:315–348, 2013.

[28] S. R. de Groot and P. Mazur. *Non-equilibrium thermodynamics*. North-Holland, Amsterdam, 1962.

[29] B. E. Deal and A. S. Grove. General relationship for the thermal oxidation of silicon. *J. Appl. Phys.*, 36:3770–3778, 1965.

[30] P. Debye and E. Hückel. The theory of electrolytes I. The lowering of the freezing point and related occurrences. *Phys. Z.*, 24:185–206, 1923.

[31] E. Dörre and H. Hübner. *Alumina: Processing, Properties, and Applications*. Springer, Berlin, 1984.

[32] R. Dovesi, C. Roetti, C. Freyria-Fava, E. Apra, V. R. Saunders, and N. M. Harrison. Ab initio Hartree-Fock treatment of ionic and semi-ionic compounds: state of the art. *Phil. Trans. R. Soc. Lond. A*, 342:203–210, 1992.

[33] R. S. Eisenberg. Computing the field in proteins and channels. *J. Membr. Biol.*, 150:1–25, 1996.

[34] R. S. Eisenberg. From structure to function in open ionic channels. *J. Membr. Biol.*, 171:1–24, 1999.

[35] A. G. Evans, D. R. Clarke, and C. G. Levi. The influence of oxides on the performance of advanced gas turbines. *J. Eur. Ceram. Soc.*, 28:1405–1419, 2008.

[36] A. G. Evans, M. Y. He, and J. W. Hutchinson. Mechanics-based scaling laws for the durability of thermal barrier coatings. *Prog. Mater. Sci.*, 46:249–271, 2001.

[37] A. G. Evans, D. R. Mumm, J. W. Hutchinson, G. H. Meier, and F. S. Pettit. Mechanisms controlling the durability of thermal barrier coatings. *Prog. Mater. Sci.*, 46:505–553, 2001.

[38] H. E. Evans. Stress effects in high temperature oxidation of metals. *Int. Mater. Rev.*, 40:1–40, 1995.

[39] F. P. Fehlner and N. F. Mott. Low-temperature oxidation. *Oxid. Met.*, 2:59–99, 1970.

[40] P. Fielitz, G. Borchardt, M. Schmücker, and H. Schneider. How to measure volume diffusivities and grain boundary diffusivities of oxygen in polycrystalline oxides. *Solid State Ionics*, 160:75–83, 2003.

[41] M. W. Finnis. Metal-ceramic cohesion and the image interaction. *Acta Metall. Mater.*, 40:25–37, 1992.

[42] M. W. Finnis. The theory of metal – ceramic interfaces. *J. Phys. Condens. Matter*, 8:5811–5836, 1996.

[43] J. C. Fisher. Calculation of diffusion penetration curves for surface and grain boundary diffusion. *J. Appl. Phys.*, 22:74–77, 1951.

[44] J. Fleig. Inhomogeneous current distributions at grain boundaries and electrodes and their impact on the impedance. *Solid State Ionics*, 113:739–747, 1998.

[45] J. Fleig. The grain boundary impedance of random microstructures: numerical simulations and implications for the analysis of experimental data. *Solid State Ionics*, 150:181–193, 2002.

[46] C. Freysoldt, B. Grabowski, T. Hickel, J. Neugebauer, G. Kresse, A. Janotti, and C. G. Van de Walle. First-principles calculations for point defects in solids. *Rev. Mod. Phys.*, 86:253–305, 2014.

[47] A. T. Fromhold. *Theory of Metal Oxidation, Vol. I.* North-Holland, Amsterdam, 1976.

[48] A. T. Fromhold. Recombination And Local Equilibrium In Growing Oxide-Films. *J. Chem. Phys.*, 69:5192–5194, 1978.

[49] A. T. Fromhold. *Theory of Metal Oxidation, Vol. II.* North-Holland, Amsterdam, 1980.

[50] A. T. Fromhold. Metal oxidation kinetics from the viewpoint of a physicist: the microscopic motion of charged defects through oxides. *Langmuir*, 5:886–896, 1987.

[51] A. T. Fromhold. Space-charge modification of the ionic currents for oxide growth. *Solid State Ionics*, 75:229–239, 1995.

[52] A. T. Fromhold and E. L. Cook. Kinetics of oxide film growth on metal crystals: electron tunneling and ionic diffusion. *Phys. Rev.*, 158:600–612, 1967.

[53] A. T. Fromhold and E. L. Cook. Kinetics of oxide film growth on metal crystals: Thermal electron emission and ionic diffusion. *Phys. Rev.*, 163:650–664, 1967.

[54] D. Gillespie, W. Nonner, and R. Eisenberg. Coupling Poisson–Nernst–Planck and density functional theory to calculate ion flux. *J. Phys. Condens. Matter*, 14:12129–12145, 2002.

[55] W. T. Grandy. *Entropy and the Time Evolution of Macroscopic Systems*. Oxford University Press, Oxford, 2008.

[56] H. Guhl, H.-S. Lee, P. Tangney, W. M. C. Foulkes, A. H. Heuer, T. Nakagawa, Y. Ikuhara, and M. W. Finnis. Structural and electronic properties of $\Sigma 7$ grain boundaries in α-Al_2O_3. *Acta Mater.*, 99:16–28, 2015.

[57] X. Guo, J. Fleig, and J. Maier. Separation of Electronic and Ionic Contributions to the Grain Boundary Conductivity in Acceptor-Doped SrTiO3. *J. Electrochem. Soc.*, 148:J50–J53, 2001.

[58] X. Guo and R. Waser. Electrical properties of the grain boundaries of oxygen ion conductors : Acceptor-doped zirconia and ceria. 51:151–210, 2006.

[59] J. H. Harding, K. J. W. Atkinson, and R. W. Grimes. Experiment and Theory of Diffusion in Alumina. *J. Am. Ceram. Soc.*, 86:554–559, 2003.

[60] L. G. Harrison. Influence of dislocations on diffusion kinetics in solids with particular reference to the alkali halides. *Trans. Faraday Soc.*, 57:1191–1199, 1961.

[61] E. W. Hart. On the role of dislocations in bulk diffusion. *Acta Metall.*, 5:597, 1957.

[62] K. Hauffe. *Oxidation of Metals*. Plenum Press, New York, 1965.

[63] V. Heine. Theory of surface states. *Phys. Rev.*, 138:A1689–A1696, 1965.

[64] P. Heitjans and J. Kärger, editors. *Diffusion in Condensed Matter: Methods, Materials, Models*. Springer, Berlin, 2005.

[65] S. C. Hendy, N. J. Laycock, and M. P. Ryan. Atomistic Modeling of Cation Transport in the Passive Film on Iron and Implications for Models of Growth Kinetics. *J. Electrochem. Soc.*, 152:B271–B276, 2005.

[66] M. A. Heroux, E. T. Phipps, A. G. Salinger, H. K. Thornquist, R. S. Tuminaro, J. M. Willenbring, A. Williams, K. S. Stanley, R. A. Bartlett, V. E. Howle, R. J. Hoekstra, J. J. Hu, T. G. Kolda, R. B. Lehoucq, K. R. Long, and R. P. Pawlowski. An overview of the Trilinos project. *ACM Trans. Math. Softw.*, 31:397–423, 2005.

[67] C. Herring. Diffusional viscosity of a polycrystalline solid. *J. Appl. Phys.*, 21:437–445, 1950.

[68] A. H. Heuer. Oxygen and aluminum diffusion in α-Al_2O_3: How much do we really understand? *J. Eur. Ceram. Soc.*, 28:1495–1507, 2008.

[69] A. H. Heuer, M. Z. Azar, H. Guhl, W. M. C. Foulkes, B. Gleeson, T. Nakagawa, Y. Ikuhara, and M. W. Finnis. The Band Structure of Polycrystalline Al_2O_3 and its Influence on Transport Phenomena. *J. Am. Ceram. Soc.*, 99:733–747, 2016.

[70] A. H. Heuer, D. B. Hovis, J. L. Smialek, and B. Gleeson. Alumina Scale Formation: A New Perspective. *J. Am. Ceram. Soc.*, 94:146–153, 2011.

[71] A. H. Heuer, T. Nakagawa, M. Z. Azar, D. B. Hovis, J. L. Smialek, B. Gleeson, N. D. M. Hine, H. Guhl, H. S. Lee, P. Tangney, W. M. C. Foulkes, and M. W. Finnis. On the growth of Al_2O_3 scales. *Acta Mater.*, 61:6670–6683, 2013.

[72] A. H. Heuer and M. Zahiri Azar. A disconnection mechanism of enhanced grain boundary diffusion in Al_2O_3. *Scr. Mater.*, 102:15–18, 2015.

[73] H. M. Hindam and W. W. Smeltzer. Growth and microstructure of α-Al_2O_3 on β-NiAl. *J. Electrochem. Soc.*, 127:1630–1635, 1980.

[74] N. D. M. Hine, K. Frensch, W. M. C. Foulkes, and M. W. Finnis. Supercell size scaling of density functional theory formation energies of charged defects. *Phys. Rev. B*, 79:024112, 2009.

[75] J. P. Hirth, B. Pieraggi, and R. A. Rapp. The role of interface dislocations and ledges as sources/sinks for point defects in scaling reactions. *Acta Met. mater.*, 43:1065–1073, 1995.

[76] J. M. Howe. Bonding, structure, and properties of metal/ceramic interfaces: Part 1 Chemical bonding, chemical reaction, and interfacial structure. *Int. Mater. Rev.*, 38:233–256, 1993.

[77] J. M. Howe, R. C. Pond, and J. P. Hirth. The role of disconnections in phase transformations. *Prog. Mater. Sci.*, 54:792–838, 2009.

[78] D. Hull and D. E. Rimmer. The growth of grain-boundary voids under stress. *Philos. Mag.*, 4:673–687, 1959.

[79] A. Jüngel. *Transport Equations for Semiconductors*. Springer, Berlin, 2009.

[80] S. Kim, J. Fleig, and J. Maier. Space charge conduction: Simple analytical solutions for ionic and mixed conductors and application to nanocrystalline ceria. *Phys. Chem. Chem. Phys.*, 5:2268–2273, 2003.

[81] R. Kirchheim. Growth kinetics of passive films. *Electrochim. Acta*, 32:1619–1629, 1987.

[82] R. Kirchheim. Stress and electromigration in Al-lines of integrated circuits. *Acta Metall. Mater.*, 40:309–323, 1992.

[83] S. Kitaoka. Mass transfer in polycrystalline alumina under oxygen potential gradients at high temperatures. *J. Ceram. Soc. Japan*, 124:1100–1109, 2016.

[84] S. Kitaoka, T. Matsudaira, and M. Wada. Mass-Transfer Mechanism of Alumina Ceramics under Oxygen Potential Gradients at High Temperatures. *Mater. Trans.*, 50:1023–1031, 2009.

[85] S. Kitaoka, T. Matsudaira, M. Wada, T. Saito, M. Tanaka, and Y. Kagawa. Control of oxygen permeability in alumina under oxygen potential gradients at high temperature by dopant configurations. *J. Am. Ceram. Soc.*, 97:2314–2322, 2014.

[86] D. A. Knoll and D. E. Keyes. Jacobian-free Newton-Krylov methods: a survey of approaches and applications. *J. Comput. Phys.*, 193:357–397, 2004.

[87] H. J. Kreuzer. *Nonequilibrium thermodynamics and its statistical foundations*. Clarendon Press, Oxford, 1981.

[88] R. Krishnamurthy and D. J. Srolovitz. Stress distributions in growing oxide films. *Acta Mater.*, 51:2171–2190, 2003.

[89] R. Krishnamurthy and D. J. Srolovitz. Stress distributions in growing polycrystalline oxide films. *Acta Mater.*, 52:3761–3780, 2004.

[90] F. C. Larché and J. W. Cahn. The interaction of composition and stress in crystalline solids. *J. Res. Natl. Bur. Stand.*, 89:467–500, 1984.

[91] A. D. Le Claire. The analysis of grain boundary diffusion measurements. *Br. J. Appl. Phys.*, 14:351–356, 1963.

[92] G. Lebon and D. Jou. *Understanding non-equilibrium thermodynamics*. Springer, Berlin, 2008.

[93] Y. Lei, Y. Gong, Z. Duan, and G. Wang. Density functional calculation of activation energies for lattice and grain boundary diffusion in alumina. *Phys. Rev. B*, 87:214105, 2013.

[94] R. J. LeVeque. *Finite Difference Methods for Ordinary and Partial Differential Equations*. SIAM, Philadelphia, 2007.

[95] Y. Levin. Electrostatic correlations. *Reports Prog. Phys.*, 65:1577–1632, 2002.

[96] A. M. Limarga, D. S. Wilkinson, and G. C. Weatherly. Modeling of oxidation-induced growth stresses. *Scr. Mater.*, 50:1475–1479, 2004.

[97] C. C. Lin and L. A. Segel. *Mathematics Applied to Deterministic Problems in the Natural Sciences*. SIAM, Philadelphia, 1988.

[98] D. M. Lipkin and D. R. Clarke. Measurement of the stress in oxide scales formed by oxidation of alumina-forming alloys. *Oxid. Met.*, 45:267–280, 1996.

[99] D. Liu, S. J. Clark, and J. Robertson. Oxygen vacancy levels and electron transport in Al_2O_3. *Appl. Phys. Lett.*, 96:32903–32905, 2010.

[100] Q. Ma and D. R. Clarke. Stress Measurement in Single-Crystal and Polycrystalline Ceramics Using Their Optical Fluorescence. *J. Am. Ceram. Soc.*, 76:1433–40, 1993.

[101] Q. Ma and D. R. Clarke. Piezospectroscopic Determination of Residual Stresses in Polycrystahe Alumina. *J. Am. Ceram. Soc.*, 77:298–302, 1994.

[102] D. D. Macdonald. The Point Defect Model for the Passive State. *J. Electrochem. Soc.*, 139:3434–3449, 1992.

[103] D. D. Macdonald. The history of the Point Defect Model for the passive state: A brief review of film growth aspects. *Electrochim. Acta*, 56:1761–1772, 2011.

[104] D. D. Macdonald and G. R. Engelhardt. The Point Defect Model for Bi-Layer Passive Films. *ECS Trans.*, 28:123–144, 2010.

[105] J. Maier. Defect chemistry and ionic conductivity in thin films. *Solid State Ionics*, 23:59–67, 1987.

[106] J. Maier. Ionic conduction in space charge regions. *Prog. Solid State Chem.*, 23:171–263, 1995.

[107] J. Maier. Ionic transport in nano-sized systems. *Solid State Ionics*, 175:7–12, 2004.

[108] J. Maier. Nanoionics: ion transport and electrochemical storage in confined systems. *Nat. Mater.*, 4:805–815, 2005.

[109] J. Maier. Space charge effects in confined ceramic systems. *Int. J. Mater. Res.*, 99:24–25, 2008.

[110] P. Marcus and V. Maurice. Atomic level characterization in corrosion studies. *Philos. Trans. R. Soc. A*, 375:20160414, 2017.

[111] P. Marcus, V. Maurice, and H.-H. Strehblow. Localized corrosion (pitting): A model of passivity breakdown including the role of the oxide layer nanostructure. *Corros. Sci.*, 50:2698–2704, 2008.

[112] P. A. Markowich, C. A. Ringhofer, and C. Schmeiser. *Semiconductor Equations*. Springer, Vienna, 1990.

[113] P. A. Markowich, C. A. Ringhofer, S. Selberherr, and M. Lentini. A singular perturbation approach for the analysis of the fundamental semiconductor equations. *IEEE Trans. Electron Devices*, 30:1165–1180, 1983.

[114] T. Matsudaira, S. Kitaoka, N. Shibata, T. Nakagawa, and Y. Ikuhara. Mass transfer through a single grain boundary in alumina bicrystals under oxygen potential gradients. *J. Mater. Sci.*, 46:4407–4412, 2011.

[115] T. Matsudaira, M. Wada, and S. Kitaoka. Effect of Dopants on the Distribution of Aluminum and Oxygen Fluxes in Polycrystalline Alumina Under Oxygen Potential Gradients at High Temperatures. *J. Am. Ceram. Soc.*, 96:3243–3251, 2013.

[116] T. Matsudaira, M. Wada, T. Saitoh, and S. Kitaoka. The effect of lutetium dopant on oxygen permeability of alumina polycrystals under oxygen potential gradients at ultra-high temperatures. *Acta Mater.*, 58:1544–1553, 2010.

[117] T. Matsudaira, M. Wada, T. Saitoh, and S. Kitaoka. Oxygen permeability in cation-doped polycrystalline alumina under oxygen potential gradients at high temperatures. *Acta Mater.*, 59:5440–5450, 2011.

[118] K. Matsunaga, A. Nakamura, T. Yamamoto, and Y. Ikuhara. Theoretical study of defect structures in pure and titanium-doped alumina. 172:155–158, 2004.

[119] V. Maurice and P. Marcus. Passive films at the nanoscale. *Electrochim. Acta*, 84:129–138, 2012.

[120] R. A. McKee and R. E. Druschel. The Microstructures and Growth Rates of FeS on Pure and Not-So-Pure Iron. *J. Electrochem. Soc.*, 131:853–857, 1984.

[121] H. Mehrer. *Diffusion in Solids: Fundamentals Methods, Materials, Diffusion-Controlled Processes*. Springer, Berlin, 2007.

[122] R. Memming. *Semiconductor electrochemistry*. Wiley-VCH, Weinheim, 2015.

[123] S. K. Mohapatra and F. A. Kröger. The Dominant Type of Atomic Disorder in α-Al_2O_3. *J. Am. Ceram. Soc.*, 61:106–109, 1978.

[124] W. Mönch. *Semiconductor surfaces and interfaces*. Springer, Berlin, 2001.

[125] N. F. Mott. A theory of the formation of protective oxide films on metals. *Trans. Faraday Soc.*, 35:1175–1177, 1939.

[126] N. F. Mott. The theory of the formation of protective oxide films on metals, II. *Trans. Faraday Soc.*, 35:472–483, 1940.

[127] N. F. Mott. A theory of the formation of protective oxide films on metals, III. *Trans. Faraday Soc.*, 43:429–434, 1947.

[128] R. G. Munro. Evaluated Material Properties for a Sintered α-Alumina. *J. Am. Ceram. Soc.*, 80:1919–1928, 2005.

[129] D. Naumenko, B. Gleeson, E. Wessel, L. Singheiser, and W. J. Quadakkers. Correlation between the Microstructure, Growth Mechanism, and Growth Kinetics of Alumina Scales on a FeCrAlY Alloy. *Metall. Mater. Trans. A*, 38:2974–2983, 2007.

[130] D. Naumenko, B. A. Pint, and W. J. Quadakkers. Current Thoughts on Reactive Element Effects in Alumina-Forming Systems: In Memory of John Stringer. *Oxid. Met.*, 86:1–43, 2016.

[131] W. H. Nernst. Zur Kinetik der in Lösung befindlichen Körper. *Z. Phys. Chem.*, 2:613–637, 1888.

[132] W. H. Nernst. Die elektromotorische Wirksamkeit der Jonen. *Z. Phys. Chem.*, 4:129, 1889.

[133] S. Nesic. Key issues related to modelling of internal corrosion of oil and gas pipelines – A review. *Corros. Sci.*, 49:4308–4338, 2007.

[134] S. Nesic and K. L. J. Lee. A Mechanistic Model for Carbon Dioxide Corrosion of Mild Steel in the Presence of Protective Iron Carbonate Films—Part 1: Theory and Verification. *Corrosion*, 59:616–628, 2003.

[135] J. A. Nychka and D. R. Clarke. Quantification of aluminum outward diffusion during oxidation of FeCrAl alloys. *Oxid. Met.*, 63:325–352, 2005.

[136] J. A. Nychka, D. R. Clarke, and J. R. Dryden. Quantifying cation grain boundary diffusion. *J. Appl. Phys.*, 102:034907, 2007.

[137] J. F. Nye. *Physical properties of crystals: Their representation by tensors and matrices*. Clarendon Press, Oxford, 1985.

[138] T. Ogawa, A. Kuwabara, C. A. J. Fisher, H. Moriwake, K. Matsunaga, K. Tsuruta, and S. Kitaoka. A density functional study of vacancy formation in grain boundaries of undoped α-alumina. *Acta Mater.*, 69:365–371, 2014.

[139] L. Onsager. Reciprocal relations in irreversible processes. I. *Phys. Rev.*, 37:405–426, 1931.

[140] L. Onsager. Reciprocal relations in irreversible processes. II. *Phys. Rev.*, 38:2265–2279, 1931.

[141] L. Onsager. Theories of Concentrated Electrolytes. *Chem. Rev.*, 13:73–89, 1933.

[142] N. P. Padture, M. Gell, and E. H. Jordan. Thermal Barrier Coatings for Gas-Turbine Engine Applications. *Science*, 296:280–284, 2002.

[143] D. E. Parry. The electrostatic potential in the surface region of an ionic crystal. *Surf. Sci.*, 49:433–440, 1975.

[144] D. E. Parry. Errata: The electrostatic potential in the surface region of an ionic crystal. *Surf. Sci.*, 54:195, 1976.

[145] M. Planck. Ueber die Erregung von Electricität und Wärme in Electrolyten. *Ann. Phys. Chem.*, 39:161–186, 1890.

[146] N. Pottier. *Nonequilibrium Statistical Physics: Linear Irreversible Processes*. Oxford University Press, Oxford, 2009.

[147] W. J. Quadakkers, A. Elschner, W. Speier, and H. Nickel. Composition and growth mechanisms of alumina scales on FeCrAl-based alloys determined by SNMS. *Appl. Surf. Sci.*, 52:271–287, 1991.

[148] A. Reddy, D. B. Hovis, A. H. Heuer, A. P. Paulikas, and B. W. Veal. In Situ Study of Oxidation-Induced Growth Strains In a Model NiCrAlY Bond-Coat Alloy. *Oxid. Met.*, 67:153–177, 2007.

[149] F. N. Rhines and J. S. Wolf. The role of oxide microstructure and growth stresses in the high-temperature scaling of nickel. *Metall. Trans.*, 1:1701–1710, 1970.

[150] C. A. Ringhofer. A Singular Perturbation Analysis for the Transient Semiconductor Device Equations in One Space Dimension. *IMA J. Appl. Math.*, 39:17–32, 1987.

[151] J. Rogal, S. V. Divinski, M. W. Finnis, A. Glensk, J. Neugebauer, J. H. Perepezko, S. Schuwalow, M. H. F. Sluiter, and B. Sundman. Perspectives on point defect thermodynamics. *Phys. Status Solidi B*, 251:97–129, 2014.

[152] C. Sarioglu, E. Schumann, J. R. Blachere, F. S. Pettit, and G. H. Meier. X-ray determination of stresses in alumina scales on high temperature alloys. *Mater. High Temp.*, 17:109–115, 2000.

[153] N. Sato and M. Cohen. The Kinetics of Anodic Oxidation of Iron in Neutral Solution. *J. Electrochem. Soc.*, 111:519–522, 1964.

[154] D. L. Scharfetter and H. K. Gummel. Large-signal analysis of a silicon read diode oscillator. *IEEE Trans. Electron Devices*, 16:64–77, 1969.

[155] E. Schöll, editor. *Theory of Transport Properties of Semiconductor Nanostructures*. Springer, 1998.

[156] W. Schottky and C. Wagner. Theorie der geordneten Mischphasen. *Z. Phys. Chem.*, B11:163–210, 1930.

[157] E. Schumann, C. Sarioglu, J. R. Blachere, F. S. Pettit, and G. H. Meier. High-Temperature Stress Measurements During the Oxidation of NiAl. *Oxid. Met.*, 53:259–272, 2000.

[158] S. Selberherr. *Analysis and simulation of semiconductor devices*. Springer, Vienna, 1984.

[159] A. Seyeux, V. Maurice, and P. Marcus. Oxide Film Growth Kinetics on Metals and Alloys: I. Physical Model. *J. Electrochem. Soc.*, 160:C189–C196, 2013.

[160] J. S. Sheasby and D. B. Jory. Electrical properties of growing alumina scales. *Oxid. Met.*, 12:527–539, 1978.

[161] A. Singer, D. Gillespie, J. Norbury, and R. S. Eisenberg. Singular perturbation analysis of the steady-state Poisson-Nernst-Planck system: Applications to ion channels. *Eur. J. Appl. Math.*, 19:541–560, 2008.

[162] W. W. Smeltzer, R. R. Haering, and J. S. Kirkaldy. Oxidation of metals by short circuit and lattice diffusion of oxygen. *Acta Metall.*, 9:880–885, 1961.

[163] W. W. Smeltzer and D. J. Young. Oxidation properties of transition metals. *Prog. Solid State Chem.*, 10:17–54, 1975.

[164] J. L. Smialek, N. S. Jacobson, B. Gleeson, D. B. Hovis, and A. H. Heuer. Oxygen Permeability and Grain-Boundary Diffusion Applied to Alumina Scales. *NASA/TM*, 217855, 2013.

[165] D. M. Smyth. *The Defect Chemistry of Metal Oxides*. Oxford University Press, Oxford, 2000.

[166] M. V. Speight and J. E. Harris. The generation of stresses in oxide films growing by cation diffusion. *Acta Metall.*, 26:1043–1045, 1978.

[167] F. H. Stott. The protective action of oxide scales in gaseous environments at high temperature. *Reports Prog. Phys.*, 50:861–913, 1987.

[168] F. H. Stott, G. C. Wood, and J. Stringer. The influence of alloying elements on the development and maintenance of protective scales. *Oxid. Met.*, 44:113–145, 1995.

[169] J. Stringer. Stress generation and relief in growing oxide films. *Corros. Sci.*, 10:513–543, 1970.

[170] J. Stringer. The Importance of Short-Circuit and Related Transport Processes in High-Temperature Oxidation. In *Defects and Transport in Oxides*, pages 495–517. Springer, Boston, 1974.

[171] M. L. Sushko, V. Alexandrov, D. K. Schreiber, K. M. Rosso, and S. M. Bruemmer. Multiscale model of metal alloy oxidation at grain boundaries. *J. Chem. Phys.*, 142:214114, 2015.

[172] A. P. Sutton and R. W. Balluffi. *Interfaces in crystalline materials*. Clarendon Press, Oxford, 1995.

[173] S. M. Sze and K. N. Kwok. *Physics of Semiconductor Devices*. John Wiley & Sons, Inc., 2006.

[174] N. Takahashi, T. Mizoguchi, T. Tohei, K. Nakamura, T. Nakagawa, N. Shibata, T. Yamamoto, and Y. Ikuhara. First Principles Calculations of Vacancy Formation Energies in Σ13 Pyramidal Twin Grain Boundary of α-Al_2O_3. *Mater. Trans.*, 50:1019–1022, 2009.

[175] M. P. Tautschnig, N. M. Harrison, and M. W. Finnis. A model for time-dependent grain boundary diffusion of ions and electrons through a film or scale, with an application to alumina. *Acta Mater.*, 132:503–516, 2017.

[176] T. Tohei, Y. Watanabe, N. Takahashi, T. Nakagawa, N. Shibata, and Y. Ikuhara. First principles study of oxygen diffusion in a α -alumina twin grain boundary. *Philos. Mag.*, 95:3985–3999, 2015.

[177] V. K. Tolpygo and D. R. Clarke. Competition Between Stress Generation and Relaxation During Oxidation of an Fe-Cr-Al-Y Alloy. *Oxid. Met.*, 49:187–212, 1998.

[178] V. K. Tolpygo and D. R. Clarke. Microstructural evidence for counter-diffusion of aluminum and oxygen during the growth of alumina scales. *Mater. High Temp.*, 20:261–271, 2003.

[179] H. Touchette. When is a quantity additive, and when is it extensive? *Phys. A Stat. Mech. its Appl.*, 305:84–88, 2002.

[180] A. Tschöpe. Grain size-dependent electrical conductivity of polycrystalline cerium oxide. II: Space charge model. *Solid State Ionics*, 139:267–280, 2001.

[181] H. L. Tuller. Ionic conduction in nanocrystalline materials. *Solid State Ionics*, 131:143–157, 2000.

[182] W. Van Roosbroeck. Theory of the Flow of Electrons and Holes in Germanium and Other Semiconductors. *Bell Syst. Tech. J.*, 29:560–607, 1950.

[183] B. W. Veal and A. P. Paulikas. Growth strains and creep in thermally grown alumina: Oxide growth mechanisms. *J. Appl. Phys.*, 104:093525, 2008.

[184] B. W. Veal, A. P. Paulikas, and P. Y. Hou. Tensile stress and creep in thermally grown oxide. *Nat. Mater.*, 5:349–351, 2006.

[185] K. J. Vetter. General kinetics of passive layers on metals. *Electrochim. Acta*, 16:1923–1937, 1971.

[186] K. J. Vetter and F. Gorn. Kinetics of layer formation and corrosion processes of passive iron in acid solutions. *Electrochim. Acta*, 18:321–326, 1973.

[187] J. B. Wachtmann, W. E. Tefft, D. G. Lam, and R. P. Stinchfield. Elastic Constants of Synthetic Single-Crystal Corundum at Room Temperature. *J. Am. Ceram. Soc.*, 43:334–334, 1960.

[188] M. Wada, T. Matsudaira, and H. Kitaoka. Mutual grain-boundary transport of aluminum and oxygen in polycrystalline Al_2O_3 under oxygen potential gradients at high temperatures. *J. Ceram. Soc. Japan*, 119:832–839, 2011.

[189] C. Wagner. Beitrag zur Theorie des Anlaufvorgangs. *Z. Phys. Chem.*, B21:25–41, 1933.

[190] C. Wagner. Beitrag zur Theorie des Anlaufvorganges II. *Z. Phys. Chem.*, B32:447–462, 1936.

[191] C. Wagner. Diffusion and High Temperature Oxidation of Metals. In *Atom Movements*, pages 152–173. 1951.

[192] C. Wagner. Überlegungen zum Übergang vom linearen zum parabolischen Zeitgesetz der Oxydation eines Metalls zu einem Oxid mit Metalldefizit. *Ber. Bunsenges. Phys. Chem.*, 70:775–780, 1966.

[193] C. Wagner. The formation of thin oxide films on metals. *Corros. Sci.*, 13:23–52, 1973.

[194] C. Wagner. Deviations from Internal Equilibrium in Scales Growing on Metals in Corroding Gases. *Ber. Bunsenges. Phys. Chem.*, 78:611–614, 1974.

[195] C. Wagner. Equations for transport in solid oxides and sulfides of transition metals. *Prog. Solid State Chem.*, 10:3–16, 1975.

[196] C. Wagner and K. Grünewald. Beitrag zur Theorie des Anlaufvorganges III. *Z. Phys. Chem.*, B40:455–475, 1938.

[197] G. D. Watkins. Intrinsic defects in II–VI semiconductors. *J. Cryst. Growth*, 159:338–344, 1996.

[198] G. D. Watkins. Intrinsic defects in silicon. *Mater. Sci. Semicond. Process.*, 3:227–235, 2000.

[199] R. T. P. Whipple. Concentration contours in grain boundary diffusion. *Philos. Mag. Ser. 7*, 45:1225–1236, 1954.

[200] S. B. Zhang and J. E. Northrup. Chemical potential dependence of defect formation energies in GaAs: Application to Ga self-diffusion. *Phys. Rev. Lett.*, 67:2339–2342, 1991.

[201] Z. Zhang and J. T. Yates. Band Bending in Semiconductors: Chemical and Physical Consequences at Surfaces and Interfaces. *Chem. Rev.*, 112:5520–5551, 2012.